# SEMICONDUCTOR METALLIZATION BY ION BEAMS

*HIROSHI INOKAWA*

MARCH 1985

*DEPARTMENT OF ELECTRONICS*

*KYOTO UNIVERSITY*

KYOTO, JAPAN

# SEMICONDUCTOR METALLIZATION BY ION BEAMS

*HIROSHI INOKAWA*

MARCH 1985

*DEPARTMENT OF ELECTRONICS*

*KYOTO UNIVERSITY*

KYOTO, JAPAN

ACKNOWLEDGEMENTS

The author wishes to express sincere gratitude to Professor Toshinori Takagi for his constant and generous guidance and encouragement throughout this work. He is also grateful to Professor Isao Yamada for his advice and stimulating discussion in accomplishing this work. Thanks are also due to Professor K. Matsubara (Department of Electronics, Yamaguchi University), Dr. J. Ishikawa, Dr. H. Takaoka, and Mr. H. Tsuji for their helpful discussions.

The author is very much indebted to Professor M. Sakisaka (Department of Nuclear Engineering), Professor T. Mannami (Department of Engineering Science), and the members of their research groups for their genial guidance and support in ion backscattering / channeling measurements. He wishes to express appreciation to Professor J.W. Mayer (Cornell University, U.S.A.) and his colleagues for precise evaluation of some of his samples by ion channeling. He also owes much to the scientists in LSI R & D Laboratory of Mitsubishi Corporation and in Eaton Corporation in testing some of his samples.

The author would like to thank Mr. K. Fukushima (Department of Electrical Engineering, Setsunan University), Mr. Shi Chang Cheng (University of Wuhang, China), Mr. H. Usui, Mr. M. Itoh, Mr. J. Matsuo, Mr. T. Fujino, Mr. M. Shibutani, and other members of Professor Takagi's research group for their intimate cooperation.

LIST OF FIGURES

Chapter 1

1.1 Number of publications related to the metallization of silicon devices.[1)]

Chapter 2

2.1 Energy regions corresponding to various engineering applications of ions and the fundamental physical and chemical phenomena underlying in them.
2.2 Self-sputtering yield of various elemental targets as a function of ion energy.
2.3 The threshold energy $E_s$ where self-sputtering yield of elemental target becomes unity.
2.4 Electronic and nuclear stopping cross-sections as a function of energy in reduced units.[10)]
2.5 Displacement cross sections in a low-energy region for various ion-target combinations.

Chapter 3

3.1 Langmuir's space-charge-limited current between plane parallel electrodes.
3.2 Beam divergence during transport in an equipotential space.
3.3 Ion current and gas pressure equivalent to a given deposition rate in terms of impinging particle flux.
3.4 Schematic diagrams of deceleration conditions. (a) Deceleration of uniform current between infinite-size parallel plates, (b) deceleration of a beam in a given deceleration field, and (c) deceleration of a beam in a practical deceleration lens system.
3.5 Relation between space charge effect parameter kd and integration constant $C_1$.
3.6 Characteristic (kd)s as a function of $u_1$, ratio of initial and final velocities.
3.7 An example of potential distribution induced by space charge effect, corresponding to several values of current density for $u_1 = (0.1)^{1/2}$.
3.8 Increase of beam radius under a linearly gradient potential distribution.
3.9 Increase of beam radius under a potential distribution proportional to the 4/3 power of the distance from the end side.

List of Figures (Continued)


3.10 Calculated ion trajectories and equipotential lines under the condition that a $^{108}Ag^+$ beam of 20 μA is decelerated from 30 keV to 20 eV. Aspect ratios δ/D are 0 (a), 0.15 (b), 0.35 (c), 0.65 (d), 0.95 (e) and 0.95 (f), respectively. (e) and (f) are in the same condition except that in (f) space charge effect is not corrected.

3.11 Set-up of experimental ion beam equipment used to evaluate the deceleration behavior of the beam.

3.12 Current-energy characteristics of the experimental ion beam equipment shown in Fig. 3.11.

3.13 1.5-MeV $He^+$ channeling spectra of Si(111) wafers bombarded by 50-eV, 300-eV and 1-keV $Ar^+$ ions using apparatus shown in Fig. 3.11.

3.14 Schematic diagram of the deceleration electrode system for ion beam deposition.

3.15 Effect of secondary electron elimination on the current-energy characteristics of the ion beam deceleration system.

3.16 Schematic diagram of the Ion Beam Engineering Experimental System installed in Kyoto University

3.17 Energy dependence of the collection efficiency of Pd ions on Si(111) surface.

3.18 RED patterns from Pd films on Si(111), formed by mass-analyzed ion beam deposition and conventional vacuum deposition, postannealed at 400°C for 30min.

3.19 Examination of the pattern in Fig. 3.18 (c). (b) is obtained by a azimuthal rotation of about 11° from the condition (a). Patterns are indexed as hexagonal $Pd_2Si$ with a = 6.49 Å and c = 3.43 Å.

3.20 Relation between resistivity and thickness of Pd films formed by mass-analyzed ion beam deposition on Si(111).

3.21 Electron micrographs of Pd films on Si(111), formed by mass-analyzed ion beam deposition and conventional vacuum deposition.

3.22 Auger spectra of Pd films deposited on Si(111) by mass-analyzed ion beams at various energies and those of pure Si, Pd, and $Pd_2Si$.

3.23 AES line analysis of ion beam deposited Pd on a Si-$SiO_2$ line-and-space pattern.

3.24 Selectivity of ion beam deposition on conductor as a function of ion energy.

3.25 RBS spectra of Pd-implanted (320 keV, 2.0 X $10^{17}$ $cm^{-2}$) Si(100), postannealed at various temperatures.

3.26 RBS spectra of Ag-implanted (320 keV, 4.0 X $10^{17}$ $cm^{-2}$) Si(100), postannealed at various temperatures.

3.27 Al concentration profiles of Al-implanted (73 keV, 4.0 X $10^{17}$ $cm^{-2}$) Si(100), postannealed at various temperatures, measured by AES with sputter etching.

List of Figures (Continued)

3.28 Collection efficiency and collected amount of Pd implanted into Si at 320 keV, as a function of dose.
3.29 Flow chart of the computer simulation of high-dose implantation and the assumptions made in it.
3.30 Calculated Pd depth distribution for various ion doses at energy level of 320 keV. Sputtering yields of Si and Pd by Pd ion are assumed to be 2.7 and 20, respectively.
3.31 Calculated collection efficiency and collected amount.
3.32 X-ray diffractometer traces of Pd-implanted (320 keV, 2.0 X $10^{17}$ $cm^{-2}$) Si(100), postannealed at various temperatures.
3.33 Sheet resistance of 320-keV Pd-implanted Si(100), postannealed at 300°C for 30 min, as a function of dose.
3.34 Sheet resistance of 73-keV Al-implanted Si(100), postannealed at 300°C for 30 min, as a function of dose.
3.35 The sheet resistance after annealing at 800°C for different doses of 40-keV Al, B and P ions implanted at room temperature in bulk silicon and silicon on sapphire.[47)]
3.36 Sheet resistance of 320-keV Pd-implanted Si(100), postannealed at 300°C for 30 min, as a function of peak Pd concentration.
3.37 Sheet resistance of Pd implanted Si(100) to a dose level of 2 X $10^{17}$ $cm^{-2}$ at various energies.
3.38 Depth profiles of Pd implanted in Si(100) to a dose level of 2 X $10^{17}$ $cm^{-2}$ at various energies.
3.39 RED patterns from Pd-implanted (320 keV, 4.0 X $10^{17}$ $cm^{-2}$) single-crystal Si, postannealed at 600°C for 30 min.

**Chapter 4**

4.1 Al-Si phase diagram.[9)]
4.2 Diffusion coefficients for Si in Al for bulk Al sample and thin film samples.[11)]
4.3 Formation of alloy penetration pits.[7)]
4.4 Correlation of electromigation lifetime for Al films with the median grain size (Δ) and with the microstructural parameter (o).[8)]
4.5 Schematic diagram of a typical ICB source.
4.6 Velocity distributions at the collimator for the nozzle source and the effusive source.
4.7 Relation between $T_1$ and $M_1$ and that between U and $M_1$.
4.8 Translational velocity for Ag cluster beam as a function of crucible temperature.[31)]
4.9 Translational Temperature for Ag cluster beam as a function of crucible temperature.[31)]
4.10 Nucleation rate J of Al (a) and Ar (b) clusters in P-T diagrams. The dotted lines in the figures show the transition of vapor state along isentropic expansion starting

from the saturated vapor in the crucible of 1 and 5 Torr. Mach number M is also shown on the lines.
4.11 Dimensions and parameters for the design of the cluster source.
4.12 Ionization potential (I.P.) of $Fe_x$ clusters are plotted as a function of cluster size. The solid circle is the I.P. for the iron atom. The work function of iron is 4.8 eV.[66]
4.13 Ratio of ionized clusters in the beam as a function of ionization electron current. Ionization voltage, 500 V; acceleration voltage, 0 kV; vapor pressure in crucible, 4 Torr.[68]
4.14 Schematic diagram of the ICB source used to deposit Al films in a normal high vacuum.
4.15 Contact resistivity of ICB Al films to p-type 10-Ωcm Si(100) substrate, as a function of annealing temperature. The data by conventional vacuum deposition (denoted as V.D.) are compared.
4.16 Ratio of X-ray {111} diffraction intensity $I_{111}$ and {200} diffraction intensity $I_{200}$ as a function of acceleration voltage ($V_a$).
4.17 Transmission electron micrographs of ICB Al films deposited at various acceleration voltages ($V_a$). (a) 1 kV, (b) 3 kV, and (c) 5 kV.
4.18 Depth profiles of oxygen in ICB Al films measured by Auger electron spectroscopy combined with sputter etching.
4.19 Cross-sectional views of ICB Al films on beveled steps. (a) $V_a$ = 1 kV, (b) $V_a$ = 5 kV.
4.20 Schematic dagram of the ICB source used to deposit Al films in an ultra-high vacuum.
4.21 Schematic diagram of the deposition apparatus.
4.22 Auger spectra of Si(111) surface before (a) and after (b) the heat treatment at 1000°C for 5 min.
4.23 5-keV RED patterns of Si(111) surface before (a) and after (b) the heat treatment at 1000°C for 5 min.
4.24 75-keV RED patterns from an Al film on Si(111), deposited by ICB ($V_a$ = 5.0 kV, $I_e$ = 100 mA, and $T_s$ = room temperature). Incident electron beam is parallel to Si[$\bar{1}$10] (a), and Si[$\bar{2}$11] (b).
4.25 Indices of the RED patterns in Fig. 4.24. The patterns correspond to Al($\bar{1}$10) reciprocal lattice (a), and Al($\bar{2}$11) reciprocal lattice (b).
4.26 Schematic illustrations of relative orientation of an Al film on Si(111) substrate.
4.27 75-keV RED patterns from an Al film on Si(100), deposited by ICB ($V_a$ = 0.2 kV, $I_e$ = 100 mA, and $T_s$ = room temperature). (a) incident electron beam is parallel to Si[011], (b) the

sample is rotated azimuthally by 35° from the condition of (a).
4.28 Indices of the RED patterns in Fig. 4.27. Diffraction from Al(110) crystal corresponds to Al(001) reciprocal lattice (a), and Al(1$\bar{1}$2) reciprocal lattice (b). Diffraction from Al(110)R crystal corresponds to Al($\bar{1}$10) reciprocal lattice (a), and Al($\bar{1}$11) reciprocal lattice (b).
4.29 Scehmatic illustrations of relative orientation of an Al film on Si(100) substrate.
4.30 Stereographic projection of the crystal planes around the normal axis of an Al film on Si(100), deposited by ICB ($V_a$ = 0.2 kV, $I_e$ = 100 mA, and $T_s$ = room temperature). 160-keV $H^+$ backscattering and channeling technique was used to determine this projection.
4.31 Dependence of backscattering yield on the azimuthal rotation angle of Al film on Si(100), deposited by ICB ($V_a$ = 0.2 kV, $I_e$ = 100 mA, and $T_s$ = room temperature). Tilt angle was fixed at 5°.
4.32 5-keV RED patterns during Al deposition by ICB ($V_a$ = 5 kV, $I_e$ = 100 mA, and $T_s$ = room temperature). Incident electron beam was parallel to Si[$\bar{2}$11] (a) clean Si(111) surface before deposition, (b) 1.5-nm thick Al film, (c) 6.0-nm thick Al film, and (d) 360-nm thick Al film.
4.33 75-keV RED pattern corresponding to Fig. 4.32 (b).
4.34 Indices of the RED pattern in Fig. 4.33. Spots of Al(100) crystal correspond to Al(011) reciprocal plane, Al(100)' to Al(013), and Al(100)'' to Al(0$\bar{1}$5).
4.35 Schematic illustrations of relative orientation of the Al crystals on Si(111) substrate at the initial stage of deposition.
4.36 Ratios of differentiated Auger peaks of $Al_{KLL}$ and $Al_{LVV}$ transitions as function of deposition time.
4.37 Scanning ion micrographs (100 keV, $Ga^+$) of Al films on Si substrate, deposited by ICB ($V_a$ = 0.2 kV, $I_e$ = 100 mA, $T_s$ = room temperature) and conventional sputter deposition ($T_s$ = room temperature). By ICB deposition, Al(111) grows epitaxially on Si(111) substrate.
4.38 Scanning electron micrographs (SEM) and scanning ion micrographs (SIM) of an ICB Al films ($V_a$ = 5 kV, $I_e$ = 100 mA, $T_s$ = room temperature) on a Si(111) substrate with lines of 100-nm thick oxide. Narrower lines on the substrate are the oxide.
4.39 Channeled backscattering spectra obtained from Al films on Si(111) and Si(100), deposited by ICB ($I_e$ = 100 mA, and $T_s$ = room temperature) at various acceleration voltages ($V_a$). Spectrum from a bare Si(111) wafer is also shown as the reference.

List of Figures (Continued)


4.40 Reflectance of the ICB deposited ($I_e$ = 100 mA, and $T_s$ = room temperature) Al films on Si(111) as a function of wavelength. Films were deposited at $V_a$ = 0.2, 3.0 and 5.0 kV, and without ionization of clusters (denoted as neutral).

4.41 SEM images of the surface and the interface of Al films on Si(111), post-annealed at 450 °C for 30 minutes in vacuum. (a) surface of an Al film deposited by ICB ($V_a$ = 5.0 kV, $I_e$ = 100 mA, and $T_s$ = room temperature), (b) interface of (a), (c) surface of an Al film deposited by conventional vacuum deposition, and (d) interface of (c).

4.42 SEM images of the surface and the interface of Al films on Si(111), post-annealed at 550 °C for 30 minutes in vacuum. (a) surface of an Al film deposited by ICB ($V_a$ = 5.0 kV, $I_e$ = 100 mA, and $T_s$ = room temperature), (b) interface of (a), (c) surface of an Al film deposited by conventional vacuum deposition, and (d) interface of (c).

4.43 AES depth profiles of Al-Si interfaces after annealing at 550°C for 30 min. (a) a sample deposited by ICB ($V_a$ = 5 kV, $I_e$ = 100 mA, $T_s$ = room temperature), and (b) a sample by conventional vacuum deposition.

4.44 1.5-MeV $He^+$ backscattering / channeling spectra of the ICB Al film on Si(111) before (a) and after (b) annealing at 500°C for 30 min. Incident ion beam is aligned to Al<111>.

4.45 1.5-MeV $He^+$ backscattering / channeling spectra of the ICB Al film on Si(111) before (a) and after (b) annealing at 500°C for 30 min. Incident ion beam is aligned to Al<100>.

4.46 Dependence of the minimum yield $\chi_{min}$ on annealing temperature, measured by 165-keV $H^+$ beam of Al<111> incidence. The ICB Al films were deposited under $V_a$ = 5 kV, $I_e$ = 100 mA, and $T_s$ = room temperature and postannealed at various temperatures for 30 min.

4.47 Current density-voltage (J-V) characteristics of ICB Al-Si junctions after annealing at various temperatures for 30 min. Zero voltage of each curve is shifted by 50 mV.

4.48 Dependence of the forward n value and the J-V barrier height of the Al-Si junctions on annealing temperature. The ICB Al films were deposited with $V_a$ = 0.2 kV, $I_e$ = 100 mA, and $T_s$ = room temperature.

4.49 1-MHz capacitance-voltage (C-V) characteristics of ICB Al-Si junctions after annealing at various temperatures for 30 min.

4.50 0.9-MeV $He^+$ aligned backscattering spectra of an epitaxial Al film before and after the treatment by steam at 550°C for 2 hours.

4.51 75-keV RED patterns of an Al film deposited on GaAs(100) by ICB ($V_a$ = 0.2 keV, $I_e$ = 100 mA, $T_s$ = room temperature). Incident elctron beam is parallel to GaAs[011] (a), and GaAs[010] (b).

List of Figures (Concluded)

4.52 Indices of the RED patterns in Fig. 4.51.
4.53 Schematic illustration of the relative orientation of the Al film on GaAs(100) substrate.
4.54 160-keV $H^+$ backscattering spectra of an epitaxial Al film deposited on GaAs(100) substrate by ICB ($V_a$ = 0.2 keV, $I_e$ = 100 mA, $T_s$ = room temperature).
4.55 1.5-MeV $He^+$ backscattering spectra of an epitaxial Al film deposited on sapphire (0001) substrate by ICB ($V_a$ = 5 kV, $I_e$ = 100 mA, $T_s$ = room temperature).
4.56 75-keV RED patterns of an epitaxial Al film deposited on sapphire substrate by ICB ($V_a$ = 5 kV, $I_e$ = 100 mA, $T_s$ = room temperature). (b) is obtained by rotating the sample azimuthally by 30° from the condition of (a).
4.57 2.0-MeV $He^+$ backscattering spectra of an epitaxial $CaF_2$ film deposited on Si(111) substrate by ICB ($V_a$ = 1 kV, $T_s$ = 700 °C). The $He^+$ beam enters the $CaF_2$<110> direction.
4.58 75-keV RED patterns of an epitaxial Al film deposited on the epitaxial $CaF_2$ film on Si(111) shown in Fig. 4.57. Incident electron beam is parallel to Si[$\bar{1}$10] (a), and Si[$\bar{2}$11] (b).

## LIST OF TABLES


**Chapter 1**

1.1 Scaling results for some device parameters.

**Chapter 2**

2.1 $E_1$ (eV) where nuclear stopping cross section $S_n(E)$ is maximum.
2.2 $E_2$ (eV) where nuclear stopping cross section $S_n(E)$ is equal to electronic stopping cross section $S_e(E)$.
2.3 Projected range $R_p$ (microns) of various ions.
2.4 Experimental threshold energy $E_d$ for atomic displacement.
2.5 Upper energy limit $E_A$ (eV) for the existence of the effect of the screening electrons.
2.6 Upper energy limit $E^*$ (eV) which causes no radiation damage.
2.7 Rate constants of various ion-molecule reactions compared with neutral atomic or molecular reactions.
2.8 Comparison of deposition temperature between CVD (atmospheric pressure) and plasma CVD.

**Chapter 3**

3.1 Experimental conditions of metallization by low-energy ion beam deposition.
3.2 Experimental conditions of metallization by high-dose ion implantation.

**Chapter 4**

4.1 Characteristics of ICB technique.
4.2 Dimensions and parameters for the design of the cluster source compared with those for a molecular beam source.
4.3 Deposition conditions of Al films by ICB in a moderately high vacuum.
4.4 Deposition conditions of Al films by ICB in an ultra-high vacuum.

CONTENTS

Chapter 1 INTRODUCTION . . . . . . . . . . . . . . . . . . . . . . . 1

References

Chapter 2 ION-SURFACE INTERACTIONS . . . . . . . . . . . . . . . . 8

2.1 Introduction . . . . . . . . . . . . . . . . . . . . . . . . 8
2.2 Fundamental Physical and Chemical Phenomena . . . . . . . . . 9
2.2.1 Sputtering . . . . . . . . . . . . . . . . . . . . . . . 9
2.2.2 Sticking . . . . . . . . . . . . . . . . . . . . . . . 17
2.2.3 Inelastic Effects . . . . . . . . . . . . . . . . . . . 17
2.2.4 Implantation . . . . . . . . . . . . . . . . . . . . . 18
2.2.5 Radiation Damage . . . . . . . . . . . . . . . . . . . 20
2.2.6 Activation of Chemical Reactions by Ionization . . . 24
2.3 Fundamental Characteristics of Ion-Based Techniques . . . 27
2.3.1 Lowering of Processing Temperature . . . . . . . . . . 27
2.3.2 Formation of Metastable Materials . . . . . . . . . . 29
2.3.3 Reduction of Film Stress . . . . . . . . . . . . . . . 29
2.3.4 Increase of Adhesion Strength of Depositied Film . . 30
2.3.5 Change in Morphology . . . . . . . . . . . . . . . . . 30
2.3.6 Densification of Deposited Film . . . . . . . . . . . 31
2.3.7 Improvement of Crystallinity, Purity, Oxidation Resistance of Film, etc. . . . . . . . . . . . . . . . 31
2.4 Conclusions . . . . . . . . . . . . . . . . . . . . . . . . 32
References

Chapter 3 METALLIZATION BY MASS-ANALYZED ION BEAMS . . . . . . 41

3.1 Introduction . . . . . . . . . . . . . . . . . . . . . . . . 41
3.2 Low-Energy Ion Beam Transport and Related Problems . . . . 44
3.2.1 Beam Divergence in an Equipotential Space . . . . . 44
3.2.2 Deceleration of Ion Beams and Related Problems . . . 45
3.2.3 Other Problems Related to Ion Beam Deceleration . . 58
3.2.4 Ion Beam Engineering Experimental System . . . . . . 62
3.3 Formation of Very Thin Films by Low-Energy Ion Beam Deposition . . . . . . . . . . . . . . . . . . . . . . . . 64
3.3.1 Experiment . . . . . . . . . . . . . . . . . . . . . . 64
3.3.2 Collection Efficiency of Pd on Si . . . . . . . . . . 64
3.3.3 Energy Dependence of Film-Substrate Reaction . . . . 67
3.3.4 Resistivity of Ultrathin Films . . . . . . . . . . . 67
3.3.5 Observation by Auger Electron Spectroscopy . . . . . 70
3.3.6 Selective Deposition on Conductor . . . . . . . . . . 72

3.4 Formation of Buried Conductive Layers by High-Dose Ion Implantation . . . . . . . . . . . . . . . . . . . . . . . 72
3.4.1 Experiment . . . . . . . . . . . . . . . . . . . . . 72
3.4.2 Depth Profile of the Implanted Metal . . . . . . . . 75
3.4.3 Collection Efficiency and Collected Amount of Implanted Pd . . . . . . . . . . . . . . . . . . . 78
3.4.4 Phase Identification . . . . . . . . . . . . . . . . 80
3.4.5 Sheet Resistance of Metal-Implanted Si . . . . . . . 83
3.4.6 Energy Dependence of Sheet Resistance of the Pd Implanted Si . . . . . . . . . . . . . . . . . 86
3.4.7 Recovery of the Crystallinity of Surface Si . . . . 89
3.5 Conclusions . . . . . . . . . . . . . . . . . . . . . . 89
References

Chapter 4 **Al METALLIZATION BY IONIZED CLUSTER BEAM** . . . . . 96

4.1 Introduction . . . . . . . . . . . . . . . . . . . . . . 96
4.2 Fundamentals of the ICB Technique . . . . . . . . . . . . 103
4.2.1 Characteristics of the ICB Technique . . . . . . . . . 103
4.2.2 Operating Conditions of the ICB Source . . . . . . . . 110
4.3 Al Deposition in a High Vacuum . . . . . . . . . . . . . 120
4.3.1 Experimental Conditions . . . . . . . . . . . . . . . 120
4.3.2 The Al-Si Contact Characteristics . . . . . . . . . . 120
4.3.3 Crystallographical Structure and Electromigration Resistance . . . . . . . . . . . . . . . . . . . . . 124
4.3.4 Oxidation Resistance . . . . . . . . . . . . . . . . . 127
4.3.5 Step Coverage . . . . . . . . . . . . . . . . . . . . 127
4.4 Al Epitaxy in an Ultra-High Vacuum . . . . . . . . . . . 129
4.4.1 Experimental Conditions . . . . . . . . . . . . . . . 129
4.4.2 Crystalline Orientation . . . . . . . . . . . . . . . 134
4.4.3 Observation of the Initial Stage of the Deposition . 137
4.4.4 SIM Observations . . . . . . . . . . . . . . . . . . . 147
4.4.5 Crystalline Quality . . . . . . . . . . . . . . . . . 149
4.4.6 Optical Reflectance . . . . . . . . . . . . . . . . . 151
4.4.7 Morphological Stability . . . . . . . . . . . . . . . 151
4.4.8 Crystallographical Stability . . . . . . . . . . . . . 154
4.4.9 Electrical Stability . . . . . . . . . . . . . . . . . 156
4.4.10 Electromigration Resistance . . . . . . . . . . . . . 163
4.4.11 Oxidation Resistance . . . . . . . . . . . . . . . . 163
4.4.12 Epitaxy on GaAs(100) . . . . . . . . . . . . . . . . 165
4.4.13 Epitaxy on Insulator Substrates . . . . . . . . . . . 168
4.5 Conclusions . . . . . . . . . . . . . . . . . . . . . . 171
References

Chapter 5 **CONCLUSIONS** . . . . . . . . . . . . . . . . . . . . 178

**APPENDIX** . . . . . . . . . . . . . . . . . . . . . . . . . . 180

**LIST OF PAPERS** . . . . . . . . . . . . . . . . . . . . . . . 188

## Chapter 1

# INTRODUCTION

Recent evolution of semiconductor metallization (making interconnections and contacts) has two aspects. The first involves meeting requirements for the reduction in the size of semiconductor devices. As summarized in Table 1.1, by scaling the dimensions of devices by a factor k, delay time of the each device (ie. FET or bipolar transistor) is reduced by a factor k while line response time is not changed, resulting in the stringent demand for the control over the resistance and/or capacitance in metallization. Another result of the device reduction is the increase of current density in metallization by a factor k and $k^2$ respectively for FET and bipolar transistors, which causes the problems of electromigration and high contact resistanse. In addition, reduction in the size of device features also brings about troubles such as spiking shorts in shallow junctions due to intrusion of metal into the semiconductor region and interlayer shorts in multilevel metallization due to hillock formation.

The other aspect of the evolution of semiconductor metallization involves realization of new device structures which include conductive layers sandwiched between semiconductor and/or insulator layers as appear in the buried gate static induction transistor,[17,18] the permeable base transistor[19] and in tree-dimensional devices in general.

Figure 1.1 shows the number of publications dealing with metallization of semiconductor devices after the bibliography by Vossen.[1] More than 3000 papers have been published since the mid-1960's and the number is increasing at an increased rate,

Table 1.1 Scaling results for some device parameters.

| Device parameter | Scaling factor | |
|---|---|---|
| | FET | Bipolar |
| Device dimensions $t_{ox}$, L, W | 1/k | 1/k |
| Doping concentration | k | k |
| Voltage | 1/k | $\sim 1$ |
| Current | 1/k | $\sim 1$ |
| Delay time in transistor | 1/k | 1/k |
| Power density | 1 | $\sim k$ |
| Capacitance | 1/k | 1/k |
| Line resistance | k | k |
| Line response time | 1 | $\sim 1$ |
| Line current density | k | $k^2$ |

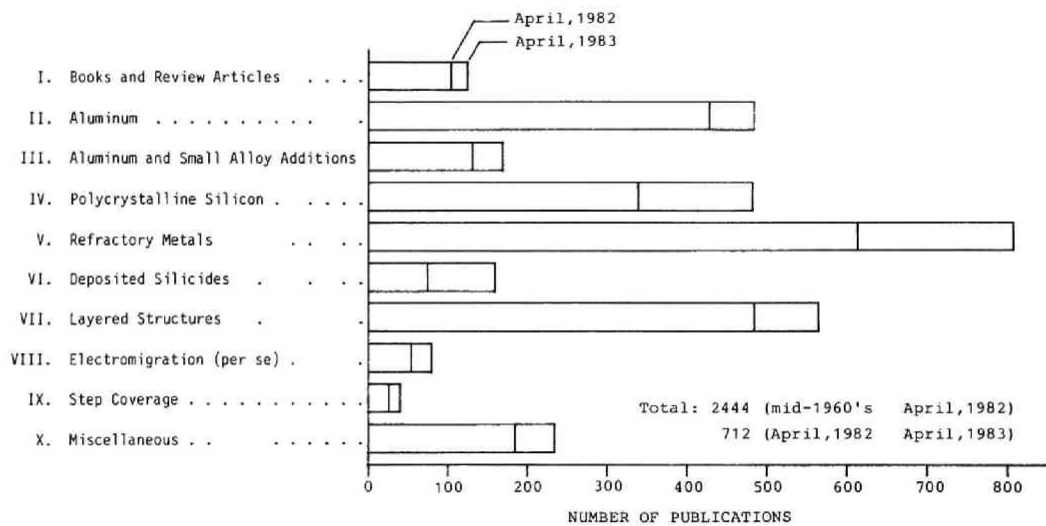


Fig. 1.1
Number of publications related to the metallization of silicon devices.[1]

showing the importance of the metallization step in device processing. Aluminum (II) and its alloys (III) are the basic materials in semiconductor metallization and their properties have been investigated considerably. Electromigration (VIII) and step coverage (IX) are old problems in metallization which have not been completely solved. Refractory metals and deposited silicides (V,VI), including epitaxial silicides for buried conductor applications and layered structures (VII), are emerging subjects related to the recent miniaturization and complication of semiconductor devices.

In this thesis semiconductor metallization by ion beams is investigated with two purposes. The first one is to solve problems in semiconductor metallization by improving the film structure and the interface properties through sputter cleaning, enhancement of adatom migration, formation of nucleation sites, etc.[2,3] The problems such as spiking shorts in shallow junctions (alloy penetration), electromigration, material reaction in a multilayered structure, hillock growth, etc. are all related to the diffusion, especially grain boundary diffusion, of metal or semiconductor atoms in the metal film, and are also related to the existence of oxide or other impurities at the interface.[4-7] As can be understood from the fact that the diffusion rate in single crystal is often smaller by a few orders of magnitude than that in polycrystal,[4,8] the high diffusion rate of atoms in metallic films, which are polycrystalline in usual semiconductor devices, can be reduced considerably by making the film structure similar to that of single crystal. In addition, the sputter cleaning effect of ion beams improves the cleanliness of the interface and the mixing effect of ion beams increases the interface bonding.[2,3] Thus the improvement of the film structure and the interface properties by ion beams is sure to solve the above-mentioned problems in metallization. Usually the problems above are met by using alloy or compound films that are more

resistant to the problems, or by utilizing multilayered structures.[5-7,9-11] However, complicated material composition and structure in metallization cause other problems, for example, precipitation of the added impurities at an interface,[12-14] material reaction in a multilayered structure,[15,16] decrease in etchability, increase in mechanical stress[9,10] and complication of the metallization step. Thus, the best way to solve the problems in metallization is to improve the film structure and the interface properties as much as possible. This improvement cannot be readily attained by conventional film deposition techniques but is attainable by using ion beams.

The second objective for the use of ion beams in semiconductor metallization is to utilize the properties of the charged particles themselves. For example, ion beams can be focused, mass-analyzed and deflected, so the position, the amount and the species of deposition can be determined electromagnetically. For another example, a buried metallic layer can be formed under the surface because the accelerated ions can penetrate into a solid material. Thus the use of ion beam realizes what cannot be realized by conventional deposition methods.

The structure of this thesis is as follows:

Chapter 2 describes the ion-surface interactions that characterize metallization by ion beams. Among them, sputtering, sticking, implantation, enhancement of adatom migration, formation of nucleation sites, etc. are included. How these ion-surface interactions improve the quality of metallization and how they determine the experimental conditions will also be explained in this chapter.

In Chapter 3, the metallization by mass-analyzed atomic ion beams will be discussed. The use of the atomic ion beams is motivated by the second objective, ie. utilizing the properties of the charged particle itself and realizing what cannot be realized

by conventional deposition methods. The special features in this chapter are formation of very thin films by low-energy ion beam deposition and formation of buried conductive layers by high-dose ion implantation.

Chapter 4 is devoted to Al metallization by ionized cluster beam (ICB) which efficiently realizes the characteristics of low-energy ion beams using macroaggregates of atoms (clusters). The first purpose, ie. improving the film structures and the interface properties to solve the problems in semiconductor metallization, is mainly considered. First, the preliminary experiment in a moderately high vacuum shows the possibilities of ICB and secondly the properties of the epitaxial Al film are discussed in detail to reveal the ultimate form of Al metallization.

In Chapter 5, results in this study are summarized comparing the atomic ion beams and ICB in terms of semiconductor metallization.

---

Note:

In this thesis, MKSA units are mainly used. However, CGS units are adopted in Chap. 2 following the custom in nuclear physics literature.

References (Chapter 1)


1) J.L. Vossen: Bibliography on Metallization Materials and Techniques for Silicon Devices (Am. Vac. Soc., New York, 1983).

2) T. Takagi, J. Vac. Sci. Technol. A2(2) (1984) 382-388.

3) T. Takagi: Thin Solid Films 92 (1982) 1-17.

4) J.M. Poate, K.N. Tu, and J.W. Mayer (eds.), Thin Films -Interdiffusion and Reactions- (Wiley, New York, 1978).

5) D. Pramanik and A.N. Saxena: Solid State Technol. 26(1) (1983) 127-133; 26(3) (1983) 131-138.

6) A.J. Learn, J. Electrochem. Soc. 123 (1976) 894.

7) J.L. Vossen, J. Vac. Sci. Technol. 19 (1981) 761.

8) M.J. Howes and D.V. Morgan (ed.): Reliability and Degradation -semiconductor devices and circuits- (John Wiley and Sons, New York, 1981).

9) S.P. Murarka: J. Vac. Sci. Technol. 17(4) (1980) 775-792.

10) A.K. Sinha: J. Vac. Sci. Technol. 19(3) (1981) 778-785.

11) K.N. Tu: J. Vac. Sci. Technol. 19(3) (1981) 766-777.

12) M. Mori, IEEE Trans. Electron Devices ED-30 (1983) 81.

13) T.M. Reith and J.D. Schick, Appl. Phys. Letters 25 (1974) 524.

14) T.M. Reith: Appl. Phys. Letters 28 (1976) 152-154.

15) P.S. Ho: Thin Solid Films 96 (1982) 301-316.

16) R.S. Nowicki and M.-A. Nicolet: Thin Solid Films 96 (1982) 317-326.

17) J. Nishizawa in: Semiconductor Technologies (Ohmsha Ltd., Tokyo, 1981) pp.201-219.

18) J. Nishizawa, T. Terasaki and J. Shibata: IEEE Trans. Electron Devices ED-22 (1975) 185-197.

19) C.O. Bozler and G.D. Alley: Proc. IEEE 70 (1982) 46-52.

# Chapter 2

# ION-SURFACE INTERACTIONS

## 2.1 Introduction

In this thesis of semiconductor metallization by ion beams, three different methods are discussed. These are low-energy mass-analyzed ion beam deposition (IBD), high-dose ion implantation, and ionized cluster beam (ICB) deposition. These three methods fall into the same category called ion-based processing techniques. This category can be further divided into subgroups, such as film formation, etching, doping, lithography, etc. and each subgroup consists of different kinds of methods. For example, ion-based film formation[1)] includes ion plating, sputter deposition, plasma chemical vapor deposition (PCVD), ionized cluster beam (ICB) deposition, ion beam deposition (IBD), etc. Although there are many methods in the ion-based processing techniques, they utilize similar physical and chemical phenomena and have common characteristics as a processing technique.

In this chapter, the underlying physical and chemical phenomena in the ion-based techniques will be described first, in order to explain how high energy should be used to realize desirable film deposition, etching, implantation, etc., and how the fundamental phenomena affect the properties of the products. Second, fundamental characteristics of the ion-based techniques and of their products will be described and improvements which can be expected in semiconductor metallization by use of ion beams will be discussed.

## 2.2 Fundamental Physical and Chemical Phenomena

Figure 2.1 shows the energy regions which correspond to various engineering applications of ions and to their underlying fundamental physical and chemical phenomena. Based on this figure, the energy dependencies of the fundamental phenomena and their relations to properties of the products of ion-based techniques will be described. Taking an argon ion-germanium target combination as an example, Fig. 2.1 also shows the related characteristic energies, such as $E^*$, $E_s$, $E_1$, $E_2$, and $E_A$, which will be discussed in the following sections.

### 2.2.1 Sputtering

Sputtering of solid surfaces by ion bombardment strictly limits the energy region used in film deposition, because build-up of a film does not occur if the self-sputtering yield of the incident ion exceeds unity. This is also the case with buried layer formation by high-dose ion implantation, because the attainable concentration of the implanted species is limited by sputtering.[2] In general, sputtering yield, defined as the average number of atoms removed from the surface of a solid per incident particle, begins to increase from zero at threshold energy which lies between 10 and 200 eV[3-5] and reaches its maximum at a few to a hundred keV[6]. Although there is an accepted theory by Sigmund[6] that describes well the sputtering from linear collision cascade (a few to a few hundreds keV for medium mass ion and target), no theory exists that precisely predicts the sputtering yield in the low energy region near the sputtering threshold. Recently, Matsunami et al. proposed a semiempirical formula for low energy sputtering yield fitted to a wide range of ion-target combinations.[4] In the Sigmund's theory, sputtering yield for keV heavy and medium-mass ions of orthogonal incidence is expressed as follows:

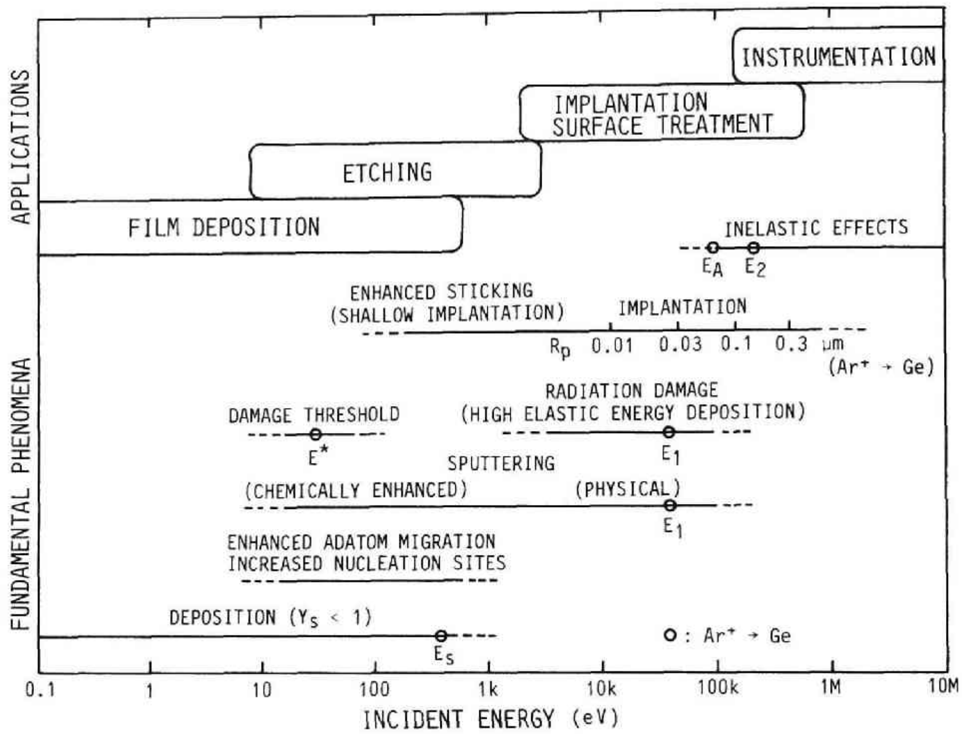


Fig. 2.1
Energy regions corresponding to various engineering applications of ions and the fundamental physical and chemical phenomena underlying in them.

$$Y_s(E) = 0.42 \frac{\alpha}{U_s} S_n(E) \tag{2.1}$$

where

$E$: energy of incident ions

$\alpha$: dimensionless quantity depending on the ion mass ratio $M_2/M_1$

$U_s$: surface binding energy (eV)

$S_n(E)$: nuclear stopping cross section ($eVcm^2/10^{15}atoms$)

Matsunami et al. introduced the correction factor to eq.(2.1) to express low-energy sputtering yield:

$$Y_s(E) = 0.42 \frac{\alpha}{U_s} S_n(E) \left[1 - \left(\frac{Eth}{E}\right)^{1/2}\right] \tag{2.2}$$

where

$E_{th}$: threshold energy for sputtering

They derived empirical expressions for $\alpha$ and $\xi$ (= $E_{th}/U_s$) by using collected experimental data:[7)]

$$\begin{aligned} \alpha = \; & 0.1019 + 0.0842\,(M_2/M_1)^{0.9805} && \text{for} \quad M_2/M_1 < 2.163 \\ & -0.4137 + 0.6092\,(M_2/M_1)^{0.1708} && \text{for} \quad M_2/M_1 > 2.163 \end{aligned} \tag{2.3}$$

$$\begin{aligned} \xi = \; & 4.143 + 11.46\,(M_2/M_1)^{-0.5004} && \text{for} \quad M_2/M_1 < 3.115 \\ & 5.809 + 2.791\,(M_2/M_1)^{0.4816} && \text{for} \quad M_2/M_1 > 3.115 \end{aligned} \tag{2.4}$$

Figure 2.2 shows the calculated self-sputtering yield of several materials as functions of ion energy. Sputtering yield begins to increase from zero at threshold energy several times larger than the surface binding energy and has less than linear sensitivity to ion energy. Fig. 2.3 shows the critical energy $E_s$ at which self-sputtering yield of incident ions becomes unity, as

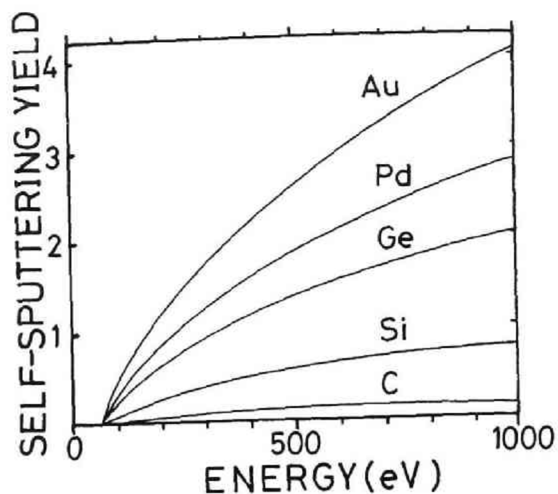


Fig. 2.2
Self-sputtering yield of various elemental targets as a function of ion energy.

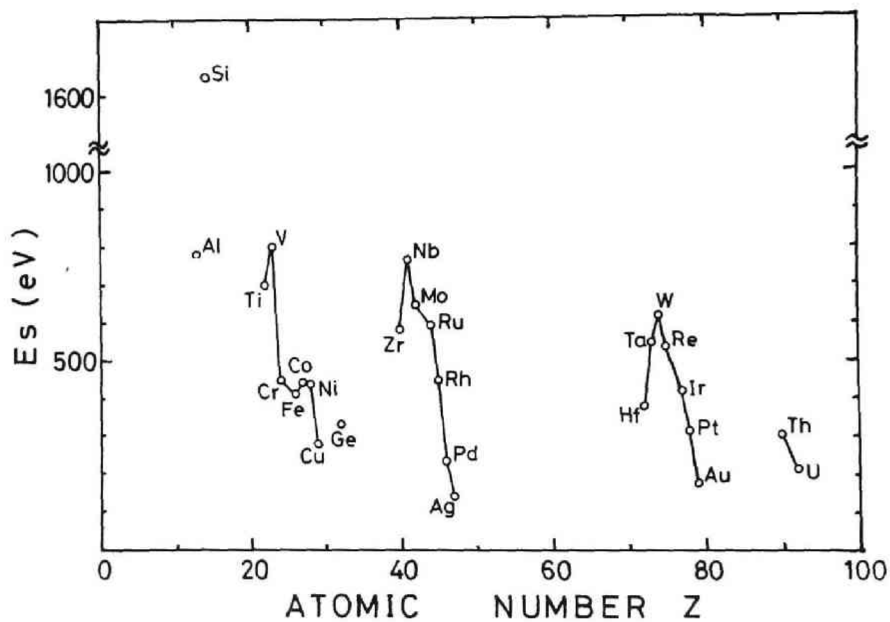


Fig. 2.3
The threshold energy $E_S$ where self-sputtering yield of elemental target becomes unity.

a function of atomic number.*) As can be seen from the figures, energy range used in film deposition is limited to less than a few hundreds of eV ( if all the incident atoms onto the substrate surface are energetic ions ).

In the case of etching applications, the energy region where sputtering is efficient is to be used, if damage caused by the ion bombardment does not matter. Since a series of elastic nuclear collisions causes sputtering (see eqs. (2.1) and (2.2)), the energy dependence of the nuclear stopping cross-section $S_n(E)$ must be examined. Lindhard et al.[10] derived a generalized expression of $S_n(E)$ based on Thomas-Fermi model:

$$S_n(E) = 4\pi a z_1 z_2 e^2 M_1/(M_1+M_2)\, s_n(\varepsilon) \quad \text{(CGS)} \qquad (2.5)$$

$Z_1$, $Z_2$: atomic numbers of the incident ion and the target atom, respectively

---

Note:

*) The critical energies $E_s$ in Fig. 2.3 are somewhat lower than those reported by Fontell and Arminen.[8] In their experiments, owing to the roughness and porocity of graphite substrate, it was not certain whether the deposition was done on the same material as that of ions (ie. whether the substrate was completely covered with the deposited film). Their data shows that the sticking probability of an ion on the same material decreases as the ion energy decreased. This disagrees with the fact that sticking probability of evaporated material is unity in the case of self-deposition[26,27] and indicated that their graphite substrate was not completely covered with the deposited material and as a result they did not measure the true self-sputtering yield. Recent experimental data by Thomas et al.,[9] in which care has been taken to measure the true sputtering yield, agree quite well with Fig. 2.3.

a: Thomas-Fermi radius
( $0.4685/(Z_1^{2/3}+Z_2^{2/3})^{1/2}$ Å )
$s_n(\varepsilon)$: nuclear stopping cross section in the reduced unit

$s_n(\varepsilon)$ is given by a universal function of the reduced energy $\varepsilon$ :

$$\varepsilon = \frac{M_2}{M_1+M_2} \frac{a}{Z_1 Z_2 e^2} E \tag{2.6}$$

Figure 2.4 shows the dependence of $s_n$ on $\varepsilon^{\frac{1}{2}}$. It also shows the reduced electronic stopping cross-section $s_e$ for future references (section 2.2.3). As is seen from Fig. 2.4, nuclear stopping cross section reaches a maximum value around $\varepsilon = 0.35$, denoted as $\varepsilon_1$ in the figure, where elastic processes including sputtering and damage creation are dominant. Table 2.1 shows the $\varepsilon_1$ for several ion-target combinations. $\varepsilon_1$ lies between a few keV and a hundred keV for most medium-mass ion-target combinations. At energy $\varepsilon_1$, etching by physical sputtering is the most efficient. However, in usual etching applications, one must take account of the radiation damage. Since the compositionally altered or crystallographically damaged layer extends to a depth comparable with the projected range of the incident ion,[2] energy less than 10 keV is usually used in etching applications.

From the standpoint of buried layer formation by high-dose ion implantation, energy around $\varepsilon_1$ is the most inefficient, because the implantation depth gained by the energy is wasted by sputter etching.

If molecules formed between target atoms and incident ions (or ambient gas atoms) have lower binding energy at the surface, sputtering is considerably enhanced.[11] By using this chemical or chemically enhanced sputtering, the energy of ions used in etching applications can be reduced to about 10 eV.[12] Reactive ion etching (RIE), reactive ion beam etching (RIBE), and chemically assisted ion beam etching (CAIBE)[13] which utilize this

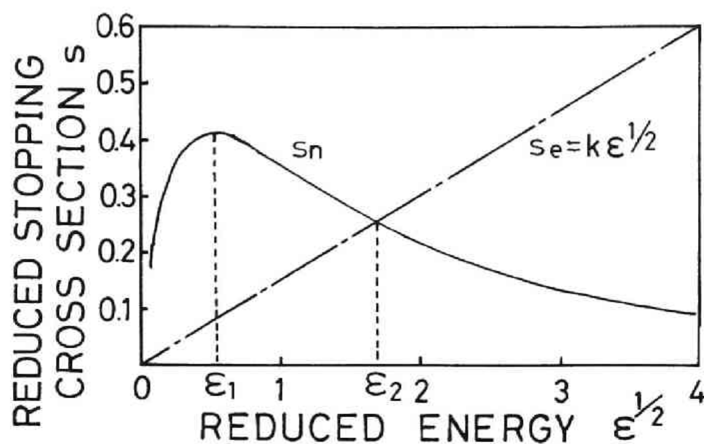


Fig. 2.4
Electronic and nuclear stopping cross-sections as a function of energy in reduced units.[10)]

Table 2.1 $E_1$ (eV) where nuclear stopping cross section $S_n(E)$ is maximum.

| PROJECTILE [$Z_1$] | TARGET [$Z_2$] | | | | |
|---|---|---|---|---|---|
| | C [6] | Si [14] | Ge [32] | Pd [46] | Au [79] |
| H [1] | 150 | 410 | 1.2 k | 1.9 k | 3.8 k |
| He[2] | 380 | 940 | 2.5 k | 3.9 k | 7.8 k |
| C [6] | 2.0 k | 3.9 k | 8.8k | 13 k | 25 k |
| Ar[18] | 16 k | 23 k | 40 k | 54 k | 93 k |
| Pd[46] | 120 k | 140 k | 190 k | 230 k | 340 k |
| Hg[80] | 430 k | 480 k | 560 k | 640 k | 830 k |

sputtering mechanism, feature low radiation damage, high etching rate, and high selectivity compared with etching by physical sputtering. Chemical or chemically enhanced sputtering is also effective in surface cleaning during film growth.

In sputtering of multicomponent materials, it is often observed that different components are being sputtered with different rate (preferential sputtering).[14,15] Preferential sputtering is an important mechanism in purification of films by ion bombardment as well as in formation of compositionally altered layers near surfaces.[2] In fact ion bombardment during deposition is reported to increase the purity of sputtered films by preferential resputtering of adsorbed impurity atoms.[16,17]

In general mass effects and bonding effects exist in preferential sputtering. When the mass ratio of the heavier component to the lighter component is large, the lighter component tends to be sputtered preferentially, mainly because more energy is distributed to the lighter component in a collision cascade.[18,19] Even if the energy distribution is equal, the light atom is sputtered more, because light atoms can be reflected by heavy atoms, and have longer ranges in the solid to escape more easily from the target suface.[2,20] Considering that oxygen and carbon, which are common contaminants encountered in film formation, are relatively light elements, ion bombardment during film formation causes preferential sputtering of them and helps purify the deposited film.

Bonding effects are caused by the difference in the surface binding energies of the constituent atoms and give rise to preferential ejection of the atoms with lower binding energy.[18,19] From the standpoint of film formation, this effect serves to densify the film during deposition by removing atoms weakly bonded on the film surface.

### 2.2.2 Sticking

Even at low energy, sticking of ions on a solid surface is greatly enhanced due to shallow implantation. Sticking probability $\eta$ of ions, defined as the ratio of the numbers of trapped to incident ions, increases rapidly as the ion energy increases and becomes almost unity at around 100 eV[8)] in the case of solid-material ions and around 1 keV in the case of gas ions[24,25)] even if the target consists of other elements than that of ions. The sticking probability decreases as the radiation dose increases because of the resputtering of the deposited material. The dose level where the sticking probability begins to decrease is proportional to the ion range in the target and inversely proportional to the sputtering yield of the ion if the yield is appreciably larger than unity.

Compared with the fact that sticking probability of neutral atoms or molecules with thermal energy on a foreign material is often far below unity[28)], high $\eta$ of the energetic ions is very useful. In fact it is successfully applied to the high-efficiency doping during deposition[29,30)] and the deposition of materials with high vapor pressure.[31)]

### 2.2.3 Inelastic Effects

Ion bombardment causes inelastic effects such as ionization and excitation of target atoms that are accompanied by emission of secondary electrons, optical photons and X-rays. In the high energy region, inelastic effects are the dominant process in deceleration (stopping) of incident ions in the target. Lindhard et al. derived an electronic (inelastic) stopping cross section in the reduced form, which is proportional to the velocity v of incident ion:[21)]

$$s_e(\varepsilon) = k\varepsilon^{1/2}, \text{ in } v < v_B z_1^{2/3} \qquad (2.7)$$

where

$v_B$: Bohr velocity ( $e^2/\hbar$ )

k: proportionality constant given by

$$k \sim \frac{0.0793\, z_1^{1/6} (z_1 z_2)^{1/2}}{(z_1^{2/3} + z_2^{2/3})^{3/4} M_2^{1/2}} \left(\frac{M_1 + M_2}{M_2}\right)^{3/2} \quad (2.8)$$

In this equation, $M_1$ and $M_2$ are in atomic mass unit (amu). k is between 0.1 and 0.25 for most ion-target combinations. As shown in Fig. 2.4 electronic stopping and nuclear stopping become equal at energy around $\varepsilon = 3$, denoted as $\varepsilon_2$ in the Fig. 2.4, above which the inelastic (electronic) process is dominant. Table 2.2 shows the $\varepsilon_2$ for several ion-target combinations. In the energy region $\varepsilon \gg \varepsilon_2$, violent eleastic collision (large-angle scattering) is rare and lattice disorder or radiation damage in the surface layer is small. Backscattered ions can be considered to have experienced only one large-angle scattering, which is one of the basic assumptions in Rutherford backscattering spectrometry (RBS).[22] Particle induced X-ray emission (PIXE) analysis can also be performed in this energy range.[23]

### 2.2.4 Implantation

An ion which has entered the target loses its energy by elastic and inelastic processes which have been described above and finally ceases its movement. The distribution of the implanted atoms is often calculated based on Lindhard, Scharff and Schiott (LSS) theory[21] and expressed in terms of projected range $R_p$, standard deviation of the projected range $\Delta R_p$, lateral standard deviation $R_\perp$, etc. Table 2.3 shows the projected range $R_p$ for several ion-target combinations. Since the depth of a layer altered by ion implantation in usual applications is a few tens to a few hundreds of nanometers, the energy range between a few to a few hundreds of keV is commonly used. Such an energy range is also adopted in the formation of buried conductive layers

Table 2.2 $E_2$ (eV) where nuclear stopping cross section $S_n(E)$ is equal to electronic stopping cross section $S_e(E)$.

| PROJECTILE [$Z_1$] | TARGET [$Z_2$] | | | | |
|---|---|---|---|---|---|
| | C [6] | Si [14] | Ge [32] | Pd [46] | Au [79] |
| H [1] | 150 | 410 | 1.2 k | 1.9 k | 3.8 k |
| He[2] | 2.0 k | 2.0 k | 2.5 k | 3.9 k | 7.8 k |
| C [6] | 19 k | 21 k | 17 k | 14 k | 25 k |
| Ar[18] | 190 k | 220 k | 230 k | 230 k | 200 k |
| Pd[46] | 1.4 M | 1.5 M | 1.6 M | 1.7 M | 1.6 M |
| Hg[80] | 4.6 M | 5.1 M | 5.3 M | 5.6 M | 5.7 M |

Table 2.3 Projected range $R_p$ (microns) of various ions.

| | H [1] | He [2] | C [6] | Ar [18] | Pd [46] | Hg [80] |
|---|---|---|---|---|---|---|
| a. In Silicon | | | | | | |
| 10 keV | 0.1612 | 0.0857 | 0.0233 | 0.0124 | 0.0090 | 0.0085 |
| 30 keV | 0.4009 | 0.2359 | 0.0677 | 0.0310 | 0.0193 | 0.0176 |
| 100 keV | 1.0019 | 0.6091 | 0.2174 | 0.0991 | 0.0483 | 0.0405 |
| 300 keV | 2.6819 | 1.3032 | 0.5907 | 0.3067 | 0.1262 | 0.0920 |
| 1 MeV | 13.8002 | 3.0948 | 1.6861 | 0.9548 | 0.4207 | 0.2575 |
| b. In Germanium | | | | | | |
| 10 keV | 0.1084 | 0.0549 | 0.0200 | 0.0088 | 0.0057 | 0.0050 |
| 30 keV | 0.3070 | 0.1649 | 0.0594 | 0.0214 | 0.0124 | 0.0103 |
| 100 keV | 0.8656 | 0.4884 | 0.2084 | 0.0655 | 0.0307 | 0.0239 |
| 300 keV | 2.4227 | 1.1520 | 0.6064 | 0.2028 | 0.0791 | 0.0543 |
| 1 MeV | 12.1646 | 2.8588 | 1.7217 | 0.6738 | 0.2590 | 0.1517 |
| c. In Indium Antimonide | | | | | | |
| 10 keV | 0.1134 | 0.0603 | 0.0229 | 0.0106 | 0.0067 | 0.0055 |
| 30 keV | 0.3293 | 0.1828 | 0.0646 | 0.0250 | 0.0144 | 0.0116 |
| 100 keV | 0.9745 | 0.5786 | 0.2246 | 0.0734 | 0.0353 | 0.0267 |
| 300 keV | 2.7805 | 1.4475 | 0.6849 | 0.2219 | 0.0892 | 0.0605 |
| 1 MeV | 13.6952 | 3.5976 | 2.0840 | 0.7502 | 0.2859 | 0.1669 |

by ion implantation described in Chap. 3.

### 2.2.5 Radiation Damage

Suitable numbers of defects on a substrate surface act as nucleation sites and modify the film growth desirably.[32] On the other hand, radiation damage which would remain in an active semiconductor layer must be eliminated. Since atoms in a crystal lattice are displaced by elastic nuclear collisions, damage is created mainly in the energy region where nuclear stopping cross section is large (see section 2.2.1).

Onset of damage creation can be characterized by displacement cross section $\sigma_d$, which is defined as the cross section for a collision in which energy greater than the threshold energy $E_d$ is transferred:[33]

$$\sigma_d(E) = \int_{E_d}^{E_m} \left(\frac{d\sigma}{dE}\right) dE \qquad (2.9)$$

where

$(d\sigma/dE)$: differential scattering cross section

$E_m$: maximum transferred energy given by

$$E_m = \frac{4 M_1 M_2}{(M_1 + M_2)^2} E \qquad (2.10)$$

The threshold energy $E_d$ required to displace an atom from its substitutional site is around 25 eV for most crystalline materials and is rather lower for compound semiconductors. Table 2.4 shows $E_d$ for several materials.[33] In order to calculate the energy dependence of the cross section, interaction potential between projectile (ion) and target atoms must be known. In the high energy region where internuclear distance included in a collision is smaller than the screening length of the electron cloud around a nucleus, Coulomb potential is a good approximation to the interaction potential.[34] That is, Coulomb potential holds when

Table 2.4 Experimental threshold energy $E_d$ for atomic displacement.

| MATERIAL | $E_d$ (eV) | REFERENCES |
|---|---|---|
| DIAMOND | $35 \pm 5$ | Phys.Rev.B14(1976)3690. |
| SILICON | 21 | Phys.Rev.138(1965)A555. |
| GERMANIUM | 27.5 | Phys.Rev.161(1967)698. |
| GaAs | 7 - 11 | J.Appl.Phys.51(1980)2038. |
| InSb | 6.4-9.9 | Phys.Rev.135A(1964)1394. |
| InAs | 6.7-8.3 | Z.Naturforsch.14a(1959)1069. |
| GaSb | 6.2-7.5 | Phys.Rev.174(1968)938; 179(1969)920. |

$$2a_B(z_1 z_2)\frac{M_1+M_2}{M_2}\frac{E_R}{E} \ll a_B/(z_1^{2/3}+z_2^{2/3})^{1/2} \quad (2.11)$$

(minimum inter-nuclear distance) (screening length)

where

$E_R$: Rydberg energy (13.59 eV)

$a_B$: Bohr radius (0.53 Å)

The energy limit $E_A$, obtained by setting the both sides of (2.11) equal, is listed in Table 2.5 for several ion-target combinations. In the low energy region ($E \ll E_A$), where the screening by an electron cloud is effective and the scattering is nearly isotropic (in the center of mass system), hard-sphere-collision approximation is feasible.[34] In this case the differential scattering cross section is given by

$$\left(\frac{d\sigma}{dE}\right)=\frac{\pi R^2}{E_m} \quad (2.12)$$

where

R: hard sphere radius

Minimum internuclear distance in a head-on collision is usually adopted as R.[35] Thus R satisfies the following equation:

$$\frac{M_2}{M_1+M_2}E=U(R) \quad (2.13)$$

where

$M_2E/(M_1+M_2)$: relative energy in the center of mass system

$U(r)$: interaction potential between projectile and target atoms

By using Born-Mayer potential[36] of the form

$$U(r)=A\,exp(-br) \quad (2.14)$$

Table 2.5 Upper energy limit $E_A$ (eV) for the existence of the effect of the screening electrons.

| PROJECTILE [$Z_1$] | TARGET [$Z_2$] | | | | |
|---|---|---|---|---|---|
| | C [6] | Si [14] | Ge [32] | Pd [46] | Au [79] |
| H [1] | 370 | 1.0 k | 2.9 k | 4.7 k | 9.5 k |
| He[2] | 960 | 2.4 k | 6.3 k | 9.9 k | 20 k |
| C [6] | 5.0 k | 9.8 k | 22 k | 34 k | 64 k |
| Ar[18] | 41 k | 59 k | 100 k | 140 k | 230 k |
| Pd[46] | 300 k | 360 k | 470 k | 580 k | 850 k |
| Hg[80] | 1.1 M | 1.2 M | 1.4 M | 1.6 M | 2.1 M |

where

A, b: constants for a particular combination of projectile and target.

we can derive the energy dependence of the displacement cross-section $\sigma_d$:

$$\sigma_d = \pi \left[\frac{1}{b} \ln \left(\frac{M_1+M_2}{M_2} \frac{A}{E}\right)\right]^2 \left(1-\frac{E_d}{E_m}\right) \quad (2.15)$$

Figure 2.5 shows the dependence of the displacement cross section on the energy of incident ion. The cross section is zero at a threshold energy E* given by

$$E^* = \frac{(M_1+M_2)^2}{4M_1M_2} E_d \quad (2.16)$$

increases rapidly to reach a maximum value, and then decreases gradually. Table 2.6 shows E* for several ion-target combinations. If one wants to avoid radiation damage completely, an energy less than E* must be used. However, a suitable number of defects on a substrate surface act as nucleation sites during film growth and contribute to formation of a continuous film at an early stage of deposition (see Chap. 3).

### 2.2.6 Activation of Chemical Reactions by Ionization

Chemical reaction is remarkably enhanced by ionization. Table 2.7 shows the rate constants of various ion-molecule reactions and neutral atomic or molecular reactions.[37,38] It can be said that the rate constant of ion-molecule reactions is around $10^{-10}$ - $10^{-9}$ $cm^3$/sec which is considerably higher than that of neutral atomic or molecular reactions. Another important characteristic of ion-molecule reactions is that the rate constant is almost independent of temperature.[37] Although these rate constant data are from gas-phase reactions, it is probable that chemical reaction is also enhanced on a solid surface by using

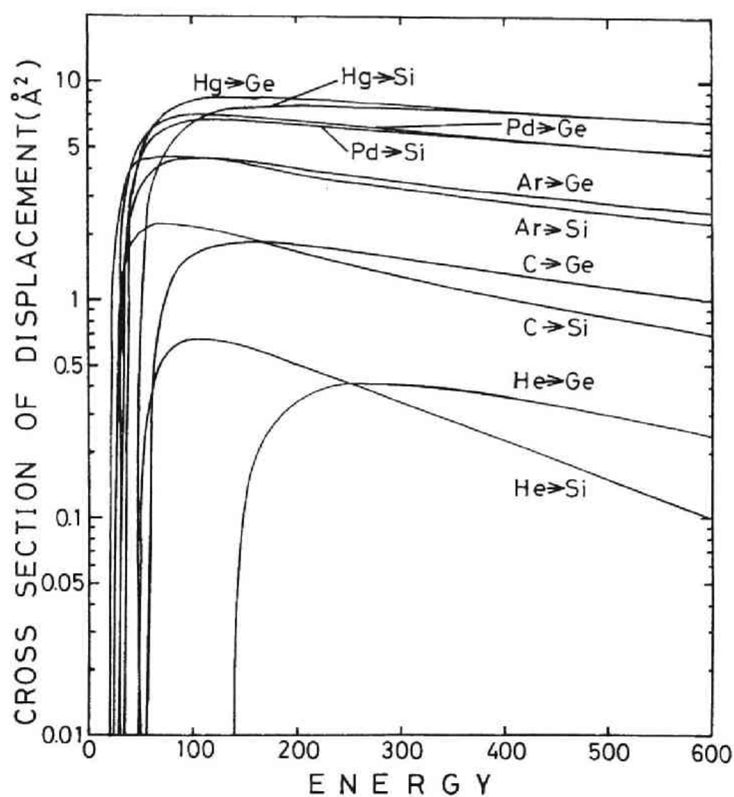


Fig. 2.5
Displacement cross sections in a low-energy region for various ion-target combinations.

Table 2.6 Upper energy limit $E^*$ (eV) which causes no radiation damage.

| PROJECTILE $[Z_1]$ | TARGET | | | | |
|---|---|---|---|---|---|
| | DIAMOND | Si | Ge | GaAs | InSb |
| H [1] | 120 | 160 | 510 | 130-200 | 190-300 |
| He[2] | 47 | 48 | 140 | 35- 55 | 51- 78 |
| C [6] | 35 | 25 | 56 | 14- 23 | 19- 30 |
| Ar[18] | 49 | 22 | 30 | 7.6- 12 | 8.5- 13 |
| Pd[46] | 96 | 32 | 29 | 7.3- 11 | 6.4-9.9 |
| Hg[80] | 160 | 49 | 35 | 9.0- 14 | 6.9- 11 |

Table 2.7 Rate constants of various ion-molecule reactions compared with neutral atomic or molecular reactions.

| REACTIONS | RATE CONST. k ($cm^3/sec$) | RATIO (%) | ENERGY (K) |
|---|---|---|---|
| POSITIVE ION-MOLECULE REACTIONS | | | |
| $O^+ + CO_2 \rightarrow O_2^+ + CO$ | $9.4 \times 10^{-10}$ | | 300 |
| $O^+ + H_2 \rightarrow HO^+ + H$ | $1.7 \times 10^{-9}$ | | 300 |
| $C^+ + CO_2 \rightarrow CO^+ + CO$ | $1.1 \times 10^{-9}$ | | 300 |
| $C^+ + O_2 \rightarrow CO^+ + O$ | $9.9 \times 10^{-10}$ | 38 | 300 |
| $\rightarrow O^+ + CO$ | | 62 | |
| $O^+ + N_2 \rightarrow NO^+ + N$ | $1.2 \times 10^{-12}$ | | 300 |
| $N_2^+ + O \rightarrow NO^+ + N$ | $1.4 \times 10^{-10}$ | ≧ 96 | 295 |
| $\rightarrow O^+ + N_2$ | | ≦ 4 | |
| $O_2^+ + N \rightarrow NO^+ + O$ | $1.2 \times 10^{-10}$ | | 296 |
| $N^+ + O_2 \rightarrow O_2^+ + N$ | $6.1 \times 10^{-10}$ | 51 | 300 |
| $\rightarrow NO^+ + O$ | | 43 | |
| $\rightarrow O^+ + NO$ | | 6 | |
| NEGATIVE ION-MOLECULE REACTIONS | | | |
| $C^- + CO_2 \rightarrow e + 2CO$ | $4.7 \times 10^{-11}$ | | 300 |
| $C^- + O_2 \rightarrow O^- + CO$ | $4.0 \times 10^{-10}$ | ≧ 85 | 300 |
| $\rightarrow e$ + products | | ≦ 15 | |
| $H^- + H_2O \rightarrow HO^- + H_2$ | $3.7 \times 10^{-9}$ | | 297 |
| $H^- + SiH_4 \rightarrow SiH_3^- + H_2$ | $5.7 \times 10^{-10}$ | | 297 |
| $H^- + H \rightarrow e + H_2$ | $1.8 \times 10^{-9}$ | | 296 |
| ATOMIC OR RADICAL REACTIONS | | | |
| $O + CO \rightarrow CO_2$ | $1.2 \times 10^{-15}$ | | 400 |
| $O + CO_2 \rightarrow O_2 + CO$ | $4.1 \times 10^{-19}$ | | 1500 |
| $O + H_2 \rightarrow HO + H$ | $2.0 \times 10^{-16}$ | | 400 |
| $H + H_2O \rightarrow HO + H_2$ | $2.2 \times 10^{-25}$ | | 300 |
| $O + NO_2 \rightarrow NO + O_2$ | $6.1 \times 10^{-12}$ | | 300 |
| $C_2H_5 + H_2 \rightarrow C_2H_6 + H$ | $2.8 \times 10^{-23}$ | | --- |
| MOLECULAR REACTIONS | | | |
| $O_2 + CO \rightarrow CO_2 + O$ | $6.5 \times 10^{-19}$ | | 1750 |
| $H_2 + O_2 \rightarrow 2OH$ | $3.4 \times 10^{-18}$ | | 1400 |
| $2NO_2 \rightarrow 2NO + O_2$ | $1.6 \times 10^{-31}$ | | 298 |
| $HI + C_2H_5I \rightarrow C_2H_6 + I_2$ | $1.6 \times 10^{-28}$ | | 298 |
| $NO + O_3 \rightarrow NO_2 + O_2$ | $1.5 \times 10^{-14}$ | | 298 |

ions as one of the source materials. In fact low temperature formation of various compounds can be attained by ion-based techniques (see Section 2.3.1).

## 2.3 Fundamental Characteristics of Ion-Based Techniques

### 2.3.1 Lowering of Processing Temperature

Since a chemical reaction is greatly enhanced by ionization of material, the temperature necessary to make compounds is considerably lowered. Table 2.8 shows an example attained by plasma chemical vapor deposition (PCVD).[39] Deposition temperature is lowered by more than 500°C by PCVD.[*] In addition to these, compounds such as $Al_2O_3$,[40,41] ZnO,[42,43] BeO,[44] GaN,[45] TiC,[46] SiC,[47] etc. are successfully formed at low temperature by various ion-based techniques. Lowering of processing temperature is also observed in physical processes such as epitaxial growth by vacuum evaporation. Si epitaxial temperature is reduced by more than 150°C using ionized cluster beam (ICB) deposition,[48] partially ionized vapor deposition (PIVD),[49-51] etc. This is probably caused by the enhancement of adatom migration and the increase in nucleation sites by ion irradiation.

Low temperature processing in very much required in recent semiconductor metallization. Because many of the trouble in metallization such as spiking shorts of shallow junction[91] and interdiffusion in layered structure[92] are thermally induced. Low temperature formation of silicides with high conductivity is also anticipated.[93]

---

Note:

*) Recently, CVD utilizing a microwave plasma is reported to have capabilities to produce $SiO_2$ and $Si_3N_4$ films at about 100°C with the same quality as that of high-temperature CVD films.[52]

Table 2.8 Comparison of deposition temperature between CVD (atmospheric pressure) and plasma CVD.

| FILM | SOURCE MATERIAL | TEMPERATURE (°C) | |
|---|---|---|---|
| | | CVD | Plasma CVD |
| $Si_3N_4$ | $SiH_4$, $NH_3$, ($N_2$) | 700 - 900 | 300 - 500 |
| $SiO_2$ | $SiH_4$, $N_2O$ | 900 - 1200 | 200 - 300 |
| $Al_2O_3$ | $AlCl_3$, $O_2$ | 700 - 1000 | 100 - 500 |

### 2.3.2 Formation of Metastable Materials

From the relationship between electrical energy and thermodynamic temperature, $kT/e = T/1.16 \times 10^4$ (eV), ion energy as low as a few eV corresponds to extremely high temperature, which enhances the formation of structually or compositionally unusual phases.

Since the high-temperature state caused by ion irradiation is quickly quenched in $10^{-11}$ - $10^{-12}$ sec,[53,54] the unusual phase is retained as a metastable without phase transformation. For example, diamond and cubic BN are produced by ion beam deposition (IBD),[55-58] plasma chemical vapor deposition (PCVD),[59-61] dual beam sputter deposition,[62] etc. Single crystal metastable alloys of $(III\text{-}V)_{1-x}IV_x$ semiconductors with x values within the miscibility gap are prepared by sputter deposition.[54,63] Metastable alloy formation by ion implantation is also intensively studied.[53] Formation of a high temperature phase of silicide at room temperature by ion irradiation will be discussed in Chap.3.

### 2.3.3 Reduction of Film Stress

Reduction of film stress by ion irradiation*) is reported by many authors.[64-72] Ion bombardment causes implantation of ion itself and knock-on implantation of target atoms. The implanted interstitials swell the film and cause compressive stress, which compensates the intrinsic tensile stress.[68] The mechanism of ion-beam annealing is also proposed to explain the reduction of film stress by ion irradiation.[67]

In semiconductor metallization using silicides, stress in a film leads to a concern about the mechanical stability.[94] Such a problem may be readily solved by controlling film stress through

---

Note:

*) In the case of sputter deposition, energetic neutral atoms take part in the reduction of film stress.[69]

ion irradiation.

### 2.3.4 Increase of Adhesion Strength of Depositied Film

One of the most important features of the ion-based film formation technique is that it can make films with high strength adhesion to the substrate. Concerning this characteristic two mechanisms are considered to exist.[66] One is the strengthening of the interfacial bonding through the formation of a transition layer by ion mixing.[73-75] The other is the reduction in the intrinsic film stress which has been discussed above. Increase of the adhesion strength by more than an order of magnitude is usually attained.[70,76] Materials such as Ge and $MgF_2$, which have high intrinsic stress and cannot be deposited without fracturing at room temperature, are successfully deposited by the use of ion irradiation during deposition.[66,77]

### 2.3.5 Change in Morphology

In usual vacuum evaporation, film grows with many voids at intergrain boundaries and the film surface shows a domed appearance if the substrate temperature is low (less than $0.3T_m$, where $T_m$ is the film material melting point). At higher temperature ($0.3 - 0.5T_m$) the film shows a typical columnar structure with mat film surface.[78] Using ion bombardment during film deposition, these morphologies can be changed into one consisting of densely packed grains with relatively smooth film surface. Voids and columns which extend through the film thickness also disappear.[79,80] It is considered that these changes are induced by the enhancement of adatom migration[81] and forward sputtering of deposited materials[80] which would transport materials to shadowed areas and erode peaks in the structure. The changes in morphology are usually observed as an increase in film packing density, mechanical strength, and optical reflectance (see section 2.3.6).

In semiconductor metallization, surface flatness and step coverage are of particular importance.[95] The mechanisms of enhanced adatom migration and resputtering of deposited material can be expected to improve these properties and increase reliability of metallization.[96]

It should be noted that ion bombardment sometimes induces surface topography and degrades surface flatness.[82-84] Differential sputter etch rates depending on crystal grain orientation and preferential etching of higher sputter yield sites which are prepared by clustered impurities, precipitates, initial irregularity of surface, etc. may cause ion-beam-induced topography.[83]

### 2.3.6 Densification of Deposited Film

Substantial improvement in the film packing density by ion bombardment during or after deposition is reported in such materials as Cu,[85] Cr,[80] $ZrO_2$, $TiO_2$, $SiO_2$, $Al_2O_3$,[86-88] SeGe,[89] etc. Ion bombardment is thought to selectively sputter the weakly bonded atoms on the surface of the growing film, filling voids through enhanced adatom migration and forward sputtering during deposition and giving rise to implanted interstitials. Such phenomena may lead to increase in film packing density.

### 2.3.7 Improvement of Crystallinity, Purity, Oxidation Resistance of Film, etc.

Many kinds of film properties are investigated and found to be improved by ion bombardment. Such phenomena mostly have the same root as those of the above-mentioned instances. Improvement of crystallinity[42,76,85,90] is similar to the lowering of epitaxial temperature in that it is due to the enhancement of adatom migration and nucleation by ion bombardment. Improvement of film purity[16,17] is based on the selective sputtering of the adsorbed light contaminants such as oxygen and carbon.

Improvement of oxidation resistance of the film[68] originates from the increased packing density and improved crystallographical perfection.

High crystallinity, purity and oxidation resistance are basic requirements in semiconductor metallization. Because thermal diffusion[97] and electromigration[98] in a film are greatly affected by its crystalline structure, impurities in a film often cause problems of increased electrical resistance[99] and instability in contact properties after heat treatment,[100] and oxidation of film surface usually leads to poor bondability and increased contact resistance between two metal layers in multilevel metallization.[91]

## 2.4 Conclusions

Fundamental phenomena observed in ion-based process techniques and general characteristics expected in them and their products have been summarized. Consideration of fundamental phenomena shows that film deposition occurs only at ion energy less than $E_s$ (Fig. 2.3), where self-sputtering yield of ion becomes unity. Deposition without lattice damage can be realized at energy less than the threshold energy $E^*$ (Table 2.6). If ion energy does not exceed $E^*$ by too much, suitable numbers of defects may serve as nucleation sites for film growth. Even at ion energy less than $E^*$, there may still exist sputtering of weakly-bonded atoms or molecules on surface, such as adsorbed impurities and deposited material itself. Enhancement of adatom migration, which is important in crystal growth, can also be expected. Without acceleration, ionization by itself can enhance chemical reactions. All these phenomena promise to contribute to high-quality semiconductor metallization at low temperature.

From the standpoint of buried layer formation by ion implantation, energy around $E_1$ (Table 2.1) where nuclear stopping

cross section is maximum must be avoided, because damage creation rate and sputtering yield is maximum at that energy. At energy more than $E_1$ a unique metallization step of buried layer formation by implantation can be attained.

These energy considerations will be utilized to set the experimental conditions in the following chapters. Unique characteristics of ion-based techniques described in this chapter will also appear in the specific experiments in the following chapters and the effectiveness of these characteristics in semiconductor metallization will be defined.

References (Chapter 2)


1) T. Takagi: Thin Solid Films 92 (1982) 1.
2) Z.L. Liau and J.W. Mayer, in: Ion Implantation, Treatise on Material Science and Technology, Vol. 18, ed., J. K. Hirvonen (Academic Press, New York, 1980) p.17
3) D.E. Harrison, Jr. and G.D. Magnuson: Phys. Rev. 122 (1961) 1421.
4) N. Matsunami, Y. Yamamura, Y. Itikawa, N. Itoh, Y. Kazumata, S. Miyagawa, K. Morita, and R. Shimizu: Radiat. Eff. Lett. 57 (1980) 15.
5) J. Bohdansky, J. Roth and H.L. Bay: J. Appl. Phys. 51 (1980) 2861.
6) L. Sigmund: Phys. Rev. 184 (1969) 383.
7) R. Shimizu, Y. Yamamura, N. Matsunami, K. Morita, M. Saidoh and N. Itoh: Oyo Butsuri (Applied Physics ) 50 (1981) 470 [in Japanese].
8) A. Fontell and E. Arminen: Can. J. Phys. 47 (1969) 2405.
9) G.E. Thomas, L.J. Beckers, J.J. Vrakking and B.R. de Koning: J. Crystal Growth 56 (1982) 557.
10) J. Lindhard, V. Nielsen and M. Scharff: Mat.- Fys. Medd. Dan. Vid. Selsk. 36 (1968) No.10.
11) J. Roth, in: Sputtering by Particle Bomberdment II, Topics in Applied Physics, Vol.52, ed. R. Behrisch (Springer-Verlag, Berlin, 1983) p.91.
12) K. Suzuki, S. Okudaira, S. Nishimatsu, K. Usami and I. Kanomata: J. Electrochem. Soc. 129 (1982) 2764.
13) E.D. Wolf, I. Adesida and J.D. Chinn: J. Vac. Sci. Technol. A2 (1984) 464.
14) G.K. Wehner: J. Vac. Sci. Technol. A1 (1983) 487.
15) G. Betz and G. K. Wehner: in Ref. 11, p.11.

References (Chapter 2)


16) J.J. Cuomo, J.M.E. Harper, C.R. Guarnieri, D.S. Yee, L.J. Attanasio, J. Angilello and C.T. Wu: J. Vac. Sci. Technol. 20 (1982) 349.

17) A.F. Mayadas, R.B. Laibowitz and J.J. Cuomo: J. Appl. Phys. 43 (1972) 1287.

18) N. Andersen and P. Sigmund: Mat.-Fys. Medd. Dan. Vid. Selsk. 39 (1974) No. 3.

19) H.F. Winters and P. Sigmund: J. Appl. Phys. 45 (1974) 4760.

20) Z.L. Liau, J.W. Mayer, W.L. Brown and J.M. Poate: J. Appl. Phys. 49 (1978) 5295.

21) J. Lindhard, M. Scharff and H.E. Schiott: Mat.-Fys. Medd. Dan. Vid. Selsk. 33 (1963) No. 14.

22) W.-K. Chu, J.W. Mayer and M.-A. Nicolet: Backscattering Spectrometry (Academic Press, New York, 1978).

23) S.A.E. Johansson and T.B. Johansson: Nucl. Inst. Meth. 137 (1976) 473.

24) G. Carter, D.G. Armour, S.E. Donnely, D.C. Ingram and R.P. Webb: Radiat. Eff. 53 (1980) 143.

25) E.V. Kornelsen: Can. J. Phys. 42 (1964) 364.

26) B. Lewis and J.C. Anderson: Nucleation and Growth of Thin Films (Academic Press, New York, 1978) p.4.

27) K.L. Chopra: Thin film Phenomena (McGrow-Hill, New York, 1969) p.149.

28) S. Wexler: Rev. Mod. Phys. 30 (1958) 402.

29) T. Takagi, I. yamada and A. Sasaki: Ion Implantation in Semiconductors, ed. S. Namba (Plenum Press, New York, 1975) p.275.

30) Y. Ota: J. vac. Sci. Technol. A2 (1984) 393.

31) S. Shimizu, O. Tsukakoshi, S. Komiya and Y. Makita: Proc. Int'l Ion Engineering Congress - ISIAT'83 & IPAT'83, Kyoto, 1983 (IEEJ, Tokyo, 1983) p.1087.

References (Chapter 2)


32) V.O. Babaev, Ju, V. Bykov and M.B. Guseva: Thin Solid Films, 38 (1976) 1.

33) J. Bourgoin and M. Lannoo: Point Defects in Semiconductors II (Springer-Verlag, Berlin, 1983) p.218.

34) H. Kinchin and R.S. Pease: Rep. Prog. Phys. 18 (1955) 1.

35) G. Dearnaley, J.H. Freeman, R.S. Nelson and J. Stephan: Ion Implantation (North-Holland, Amsterdam, 1973) p.154.

36) A.A. Abrahamson: Phys. Rev. 178 (1969) 76.

37) J.S. Chang, R.M. Hobson, U. Ichikawa and T. Kaneda: Denri Kitai no Genshi-Bunshi Katei (Atomic and Molecular Processes of Ionized Gasses), (Tokyo Denki Univ. Press, Tokyo, 1982) p. 229 [in Japanese].

38) The Chemical Society of Japan (ed.): Kagaku Binran, Kisohen (Handbook of Chemistry, Part I), 2nd ed. (Marzen Co. Ltd., Tokyo, 1975) p.1007 [in Japanese].

39) O. Matsumoto in: Handotai Plasma Process Gijutsu (Application of Plasma Process to VLSI Technology), (Sangyo Tosho Press, Tokyo, 1980) p.50 [in Japanese].

40) R.F. Bunshah and R.J. Schramm, Thin Solid Films 40 (1977) 211.

41) R.S. Nowicki: J. Vac Sci. Technol. 14 (1977) 127.

42) T. Takagi, I. Yamada, K. Matsubara and H. Takaoka: J. Crystal Growth 45 (1978) 318.

43) T. Takagi, K. Matsubara, H. Takaoka, and I. Yamada: Thin Solid Films 63 (1979) 41.

44) T. Takagi, K. Matsubara, and H. Takaoka: J. Appl. Phys. 51 (1980) 5419.

45) K. Matsubara, T. Horibe, H. Takaoka and T. Takagi: Proc. 4th Symp. on Ion Sources and Appl. Technol. (IEEJ, Tokyo, 1980) p.137

References (Chapter 2)

46) R.F. Bunshah and A.C. Raghuram: J. Vac. Sci. Technol. 9 (1972) 1385.

47) K. Mameno, H. Takaoka, K. Matsubara and T. Takagi: Proc. Int'l Ion Engineering Congress -ISIAT'83 & IPAT'83-, Kyoto (IEEJ, Tokyo, 1983) p.1233.

48) I. Yamada, F.W. Saris, T. Takagi, K. Matsubara, H. Takaoka and S. Ishiyama: Jpn. J. Appl. Phys. 19 (1980) L181.

49) T. Itoh, T. Nakamura, M. Muromachi and T. Sugiyama: Jpn. J. Appl. Phys. 16 (1977) 553.

50) T. Narusawa, S. Shimizu, and S. Komiya: J. Vac. Sci. Technol. 16 (1979) 366.

51) S. Shimizu and S. Komiya: J. Vac. Sci. Technol. 17 (1980) 489.

52) S. Matsuo and M. Kiuchi: Jpn. J. Appl. Phys. 22 (1983) L210.

53) J.M. Poate and A.G. Cullis in: Ion Implantation, Treatise on Material Science and Technology, Vol. 18, ed., J.K. Hirvonen (Academic Press, New York, 1980) p.85.

54) J.E. Greene: J. Vac. Sci. Technol. B1 (1983) 229.

55) S. Aisenberg nad R. Chabot: J. Appl. Phys. 42 (1971) 2953.

56) E.G. Spencer, P.H. Schmidt, D.C. Joy, and F.J. Sansalone: Appl. Phys. Letters 29 (1976) 118.

57) S. Aisenberg: J. Vac. Sci. Technol. A2 (1984) 369.

58) S. Shanfield and R. Wolfson: J. Vac. Sci. Technol. A1 (1983) 323.

59) S. Berg and L.P. Andersson: Thin Solid Films 58 (1979) 117.

60) B.V. Spitsyn, L.L. Bouilon and B.V. Derjaguin: J. Crystal Growth 52 (1981) 219.

61) M. Kamo, Y. Sato, S. Matsumoto and N. Setaka: J. Crystal Growth 62 (1983) 642.

62) G. Gantherin and Chr. Weissmantel: Thin Solid Films 50 (1978) 135.

References (Chapter 2)

63) J.L. Zilko and J.E. Greene: J. Appl. Phys. 51 (1980) 1560.
64) D.W. Hoffman and J.A. Thornton: Thin Solid Films 45 (1977) 387.
65) J.A. Thornton and D.W. Hoffman: J. Vac. Sci. Technol. 14 (1977) 164.
66) E.H. Hirsch and I.K. Varga: Thin Solid Films 52 (1978) 445.
67) E.H. Hirsch and I.K. Varga: Thin Solid Films 69 (1980) 99.
68) D.W. Hoffman and M.R. Gaerttner: J. Vac. Sci. Technol. 17 (1980) 425.
69) J.A. Thornton and D.W. Hoffman: J. Vac. Sci. Technol. 18 (1981) 203.
70) M. Laugier: Thin Solid Films 81 (1981) 61.
71) J.J. Cuomo, J.M.E. Harper, C.R. Guarnieri, D.S. Yee, L.J. Attanasio, J. Angilello and C.T. Wu: J. Vac. Sci. Technol. 20 (1982) 349.
72) J.R. McNeil, A.C. Barron, S.R. Wilson, and W.C. Herrmann, Jr. : Appl. Opt. 23 (1984) 552.
73) J.L. Mukherjee, L.C. Wu, J.E. Greene and H.E. Cook: J. Vac. Sci. Technol. 12 (1975) 850.
74) J.E. Greene and M. Pestes: Thin Solid Films 37 (1976) 373.
75) A. Pan and J.E. Greene: Thin Solid Films 97 (1982) 79.
76) T. Takagi, I. Yamada and A. Sasaki: Thin Solid Films 39 (1976) 207.
77) C.M. Kennemore III and U.J. Gibson: Appl. Opt. 23 (1984) 3608.
78) B.A. Movchan and A.V. Demchishin: Fiz. Metall. Metalloved. 28 (1969) 653.
79) J.A. Thornton: J. Vac. Sci. Technol. 11 (1974) 666.
80) R.D. Bland, G.J. Kominiak and D.M. Mattox: J. Vac. Sci. Technol. 11 (1974) 671.

References (Chapter 2)


81) R. Messier, A.P. Giri and R.A. Roy: J. Vac. Sci. Technol. A2 (1984) 500.

82) G.M. McCracken: Rep. Prog. Phys. 38 (1975) 241.

83) G. Carter, B. Navinsek and J.L. Whitton in: Sputtering by Particle Bombardment II, Topics in Applied Physics, Vol. 52, ed. R. Behrisch (Springer-Verlag, Berlin, 1983) p.231.

84) R.S. Robinson and S.M. Rossnagei: J. Vac. Sci. Technol. 21 (1982) 790.

85) T. Takagi, I. Yamada and A. Sasaki: Inst. Phys. Conf. Ser. No. 38 (1978) Chap. 3, p.142.

86) P.J. Martin, H.A. Macleod, R.P. Netterfield, C.G. Pacey and W.G. Sainty: Appl. Opt. 22 (1983) 178.

87) P.J. Martin, R.P. Netterfield, W.G. Sainty and C.G. Pacey: J. Vac. Sci. Technol. A2 (1984) 341.

88) W.G. Sainty, R.P. Netterfield and P.J. Martin: Appl. Opt. 23 (1984) 1116.

89) K.L. Chopra, K.S. Harshavardhan, S. Rajagopalan and L.K. Malhotra: Appl. Phys. Lett. 40 (1982) 428.

90) I. Yamada, Y. Hirose, H. Inokawa, and T. Takagi: Proc. 4th Symp. on Ion Sources and Ion Appl. Technol. (IEEJ, Tokyo, 1980) p.141.

91) D. Parmanik and A.N. Saxena: Solid State Technol. 26(1) (1983) 127-133; 26(3) (1983) 131-138.

92) P.S. Ho: Thin Solid Films 96 (1982) 301-316.

93) R.S. Nowicki and M.-A. Nicolet: Thin Solid Films 96 (1982) 317-326.

94) S.P. Murarka: J. Vac. Sci. Technol. 17 (1980) 775-792.

95) J.L. Vossen: J. Vac. Sci. Technol. 19 (1981) 761-765.

96) J.L. Vossen and J.J. O'neill, Jr.: RCA Rev. June, 1970, pp.276-292.

97) G.J. Van Gurp: J. Appl. Phys. 44 (1973) 2040.

References (Chapter 2)

98) S. Vaidya and A.K. Sinha: Thin Solid Films 75 (1981) 253-259.

99) A.J. Learn: J. Electrochem. Soc. 123 (1976) 894-906.

100) S. Iwata and N. Yamamoto: The Fall Meeting of JSAP, Paper No. 9p-B-1, p.716, 1981 [in Japaneae].

# Chapter 3

# METALLIZATION BY MASS-ANALYZED ION BEAMS

## 3.1 Introduction

Metallization by mass-analyzed ion beam can be classified into two methods. One method is the direct deposition of low-energy metal ions on the substrate.[1-23] In this method the energy of the ion beam must be selected so that the self-sputtering yield of the ion is less than unity and build-up of a film occurs. The other is the formation of a buried layer by high-energy ion implantaion.[24-26] This second method prevents build-up of film on the substrate surface, but a continuous conductive layer can be formed under the substrate surface when appropriate conditions are satisfied. The two have several advantages in common. Mass deposited or collected can be measured and controlled accurately as an integrated ion current. Direct patterning of the metallization can also be realized by controlling the ion path electromagnetically. Adoption of mass analysis excludes incorporation of unwanted impurities. In reality the characteristics above cannot be attained by conventional deposition methods. In addition, the synthesis of thermally nonequilibrated materials can be expected as the result of the high kinetic energy of the ions.[5]

In the case of low-energy ion beam deposition, the sticking coefficient of ions is much higher than that of thermally evaporated atoms as the result of shallow ion implantation.[2] Irradiation by ions creates defects on the substrate surface, which leads to increased density of nucleation sites. In

addition, it is difficult for the shallowly implanted low-energy ions to diffuse on the surface. This lack of surface diffusion prevents the agglomeration of adatoms into large islands, and a continuous film forms at a much lower average thickness. Because the path of the low-energy ions is influenced by small potential differences caused by the charges built up on an insulator, selective deposition on a conductor is possible. A low-energy ion beam for film deposition is difficult to obtain owing to space charge effect. The ion beam equipment for low-energy ion beam deposition is discussed first in Section 3.2, and then in Section 3.3 the fundamental properties of Pd ion beam deposition on Si are described along with a discussion of the possibilities of forming ultrathin films and of depositing selectively on a conductor.

During metallization by high-energy implantation, a buried layer is formed. Because high-energy ions are easily focused, direct patterning of the metallization by a fine beam can be realized. However, it is not clear whether a continuous conductive layer is formed by ion implantation. During implantation the irradiated surface is continuously sputtered, and the concentration of implanted species in the target material saturates to a steady-state value as the implanted species themselves are sputtered away. In case of implantation of ion species A into target B, the steady-state surface composition is described by the equation,[27]

$$N_a / N_b = r \cdot (S - 1)^{-1} \tag{3.1}$$

where $N_a$ and $N_b$ are the surface concentrations (per unit volume) of A atoms and B atoms, respectively, r is the ratio of the probability of a B atom being sputtered to the probability of an A atom being sputtered, and S is the total sputtering yield. If preferential sputtering does not take place, the concentration of A atoms (per total number of atoms) is given by the relationship

$$\frac{N_a}{N_a + N_b} = \frac{1}{S} \qquad (3.2)$$

which is the reciprocal of sputtering yield.

On the other hand, the concentration of implanted species must exceed some threshold for the implanted metal to form a continuous conductive layer. This threshold concentration has been investigated theoretically and experimentally through the use of granular metal films prepared by the co-sputtering of metal and insulator materials. The theoretical value predicted by the site percolation model is 15 vol.%, the value predicted by the continuum percolation model is 29 vol.%, and the value predicted by the resister network model is 25 vol.%.[28] The experimental values are nearly 50 vol.%.[29]

These considerations show that if one wishes to form a continuous conductive layer by implantation, the sputtering yield must not exceed 2 - 3 atoms per ion. This upper limit value is lowered when the preferential sputtering of implanted atoms takes place or the size of an implanted atom is smaller than that of a target atom. In Section 3.4 of this chapter, described are the results of Pd, Ag, and Al implantation into Si, which has a very low sputtering yield and seems suitable for the formation within it of a buried conductive metal layer by ion implantation.

In the following experiments, Pd ions are mainly used for several reasons. Since Pd reacts with Si to form a silicide at as low as 200°C and $Pd_2Si$ grows epitaxially on Si(111),[30-32] the degree of reaction and the crystallinity of the $Pd_2Si$ can be a good measure of the enhancement of chemical reaction by ion bombardment. As can be understood from the facts that a laterally uniform silicide layer can be formed by ion beam mixing of a Pd film with the substrate Si[33,34] and that the epitaxial $Pd_2Si$ films retain their crystallinity even after prolonged ion bombardment[35], palladium silicide is highly stable to ion

irradiation and is compatible with ion-based processing techniques. In addition, as a noble metal, Pd is hardly oxidized even at a low deposition rate or in a high background pressure. Relatively low temperature for vaporization is also useful in ion production.

## 3.2 Low-Energy Ion Beam Transport and Related Problems

In the apparatus used in low-energy ion beam deposition, the ion beam is initially extracted by a high negative potential (30 kV), mass separated, and then decelerated to low enough energy for film deposition (less than a few hundred eV), because the low energy ion beam is difficult to transport owing to space charge effect. In the following sections space charge effect involved in ion beam transport and ion beam deceleration is discussed mainly from the point of view of beam divergence and current limitation.

### 3.2.1 Beam Divergence in an Equipotential Space

A beam diverges or increases in radius during transport because of space charge repulsion effect. Let us consider the case that a parallel beam whose initial radius is $R_o$ and energy is $\Phi_o$ enters an equipotential space and travels a distance d. The final beam radius R is related to transport distance d by the following equation.

$$kd = 3\sqrt{2}\int_0^{\sqrt{\log(R/R_0)}} e^{w^2}\,dw \qquad (3.3)^*$$

---

Note:

*) Derivation of this equation appears in Appendix A.2.

where

$$k = \frac{3}{2}\left(\frac{J_0}{\varepsilon_0}\right)^{1/2}\left(\frac{m}{2e}\right)^{1/4}\Phi_0^{-3/4} \qquad (3.4)*$$

$J_o$: the initial current density of the beam

m: mass of the ion

e: charge of the ion

$\varepsilon_o$: dielectric constant of vacuum

Figure 3.2 shows the relation between $R/R_o$ and kd expressed by eq. (3.3). For example, since $\Phi_o$ = 100eV, $J_o$ = 10 μA/cm$^2$, m = 105 amu ($Pd^+$), and d = 0.73 cm satisfy the condition kd = 1, as can be seen in Fig. 3.1, the radius of the beam becomes 5 times larger than its original value after traveling a distance of only 7.6 cm (kd = 10.4). Considering that the beam current of 10 μA/cm$^2$ corresponds to the deposition rate of only 0.55 nm/min as shown in Fig. 3.3, the divergence of the beam is unacceptable. Thus high-energy beam transport with deceleration just in front of the substrate are combined to obtain low-energy ions in the following experiments.

### 3.2.2 Deceleration of Ion Beams and Related Problems

Deceleration of ion beams will be discussed under three conditions shown in Fig. 3.4. First, deceleration of uniform current between infinite-size parallel plates (Fig. 3.4 (a)) is

---

Note:

*) k is defined so that the equation kd=1 gives Langmuir's space-charge-limited current between plane parallel electrodes, ie.

$$(J_0)_{kd=1} = \frac{4\varepsilon_0}{9}\left(\frac{2e}{m}\right)^{1/2}\frac{\Phi_0^{3/2}}{d^2} \equiv J_s \qquad (3.5)$$

The relation between m, $\Phi_o$, d and $J_s$ are shown in Fig. 3.1.

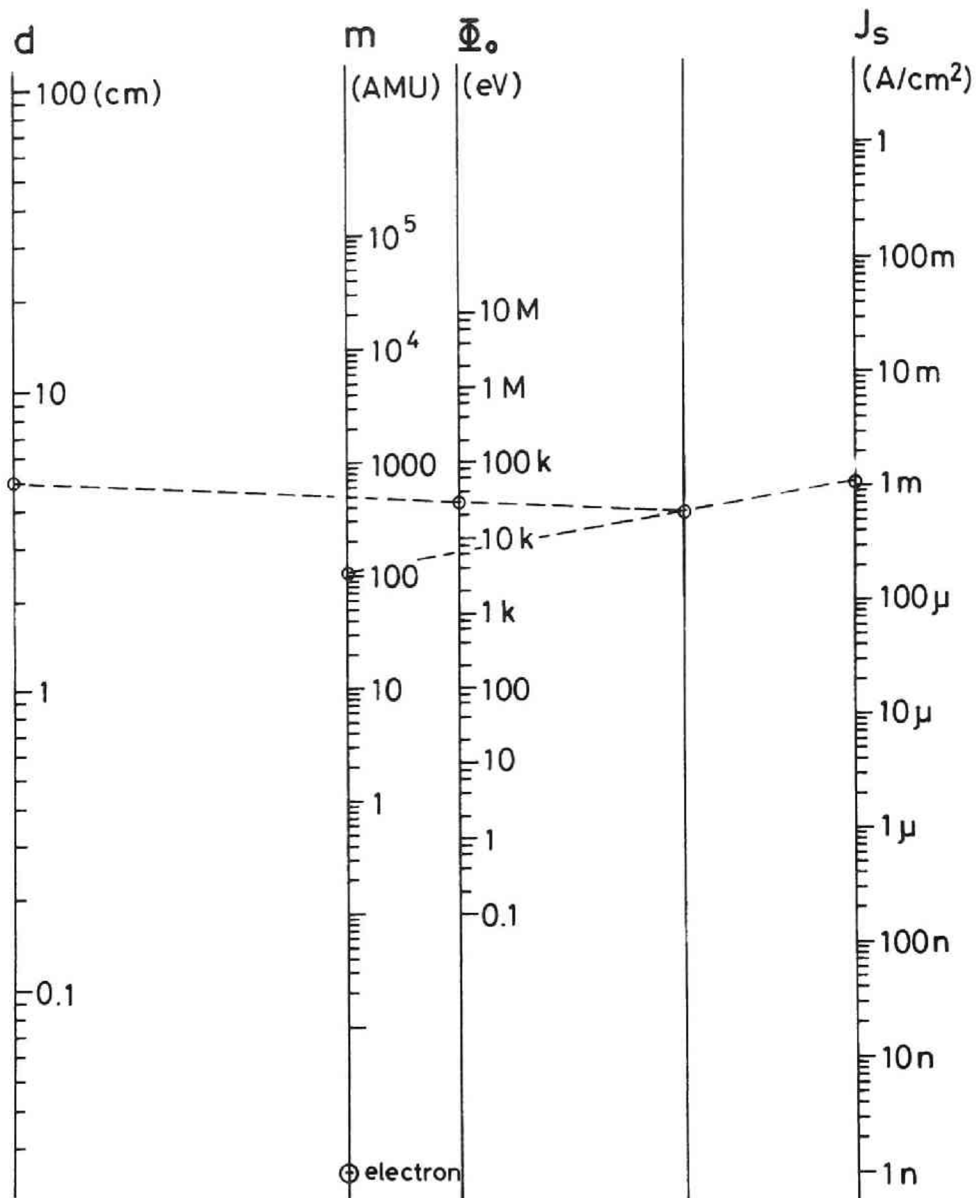


$$kd = \frac{3}{2}\sqrt{\frac{J_s}{\varepsilon_0}\sqrt{\frac{m}{2e}}}\ \Phi_0^{-3/4} d = 1$$

SPACE-CHARGE-LIMITED CURRENT ($J_s$)

Fig. 3.1
Langmuir's space-charge-limited current between plane parallel electrodes.

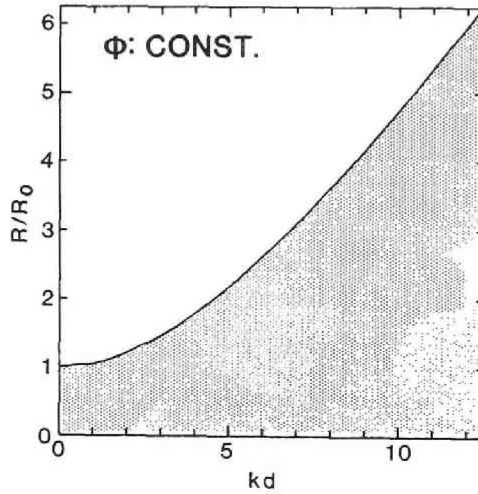


Fig. 3.2
Beam divergence during transport in an equipotential space.

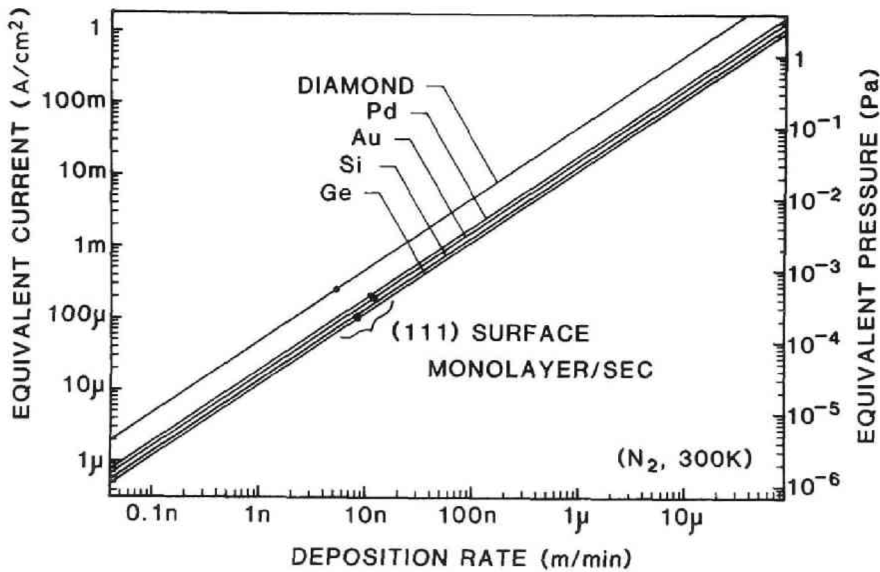


Fig. 3.3
Ion current and gas pressure equivalent to a given deposition rate in terms of impinging particle flux.

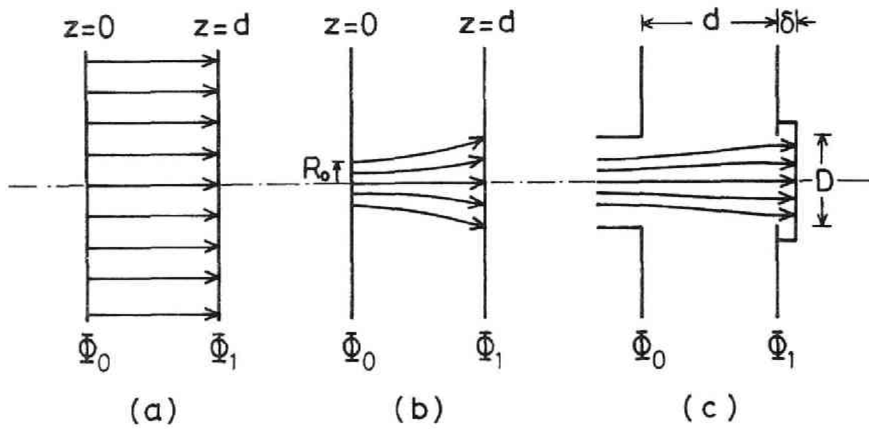


Fig. 3.4

Schematic diagrams of deceleration conditions. (a) Deceleration of uniform current between infinite-size parallel plates, (b) deceleration of a beam in a given deceleration field, and (c) deceleration of a beam in a practical deceleration lens system.

discussed to evaluate the maximum current that can be cecelerated. Secondly, deceleration of an ion beam in a given deceleration field (Fig. 3.4 (b)) is discussed to evaluate the beam divergence during deceleration. Thirdly, ion trajectories in a practical deceleration lens system (Fig. 3.4 (c)) are discussed based on computer simulation and experimental results.

Under the first condition, since ion trajectories are parallel to each other and perpendicular to the parallel plates, the main problem is to obtain the potential distribution along the beam axis. Let the initial energy and the final energy be $\Phi_o$ and $\Phi_1$, respectively. If there is no ion current, the ionic potential decreases linearly from $\Phi_o$ to $\Phi_1$. As the current increases, the potential curve bends downward because of a build-up of positive space charge. Further increase of ion current results in higher space charge density, which comes to inhibit the passage of ion current. Finally the ion current is limited to a certain value. It is found that there are two modes in potential distribution. In mode 1, the potential $\Phi$ decreases monotonically from $\Phi_o$ to $\Phi_1$ and in mode 2, the potential $\Phi$ decreases first, reaches a minimum at $z = z_2$ and increases again.

In mode 1, the potential $\Phi$ is given as the root of the equation

$$w^3 - 3C_1 w + kz - C_2 = 0 \quad (3.6)^*$$

where

$$w = (u + C_1)^{1/2} \quad (3.7)$$

---

Note:

*) Derivation of the following equations will appear in Appendix A.3.

$$u = (\Phi/\Phi_0)^{1/2} \qquad (3.8)$$

u: ion velocity relative to the initial value

$C_1$, $C_2$: integration constants

$C_1$ is obtained by solving the equation

$$kd = (1+C_1)^{1/2}(1-2C_1) - (u_1+C_1)^{1/2}(u_1-2C_1) \qquad (3.9)$$

where

$$u_1 = (\Phi_1/\Phi_0)^{1/2} \qquad (3.10)$$

$u_1$: ratio of the final and the initial velocities

$C_2$ is related to $C_1$ by

$$C_2 = (1+C_1)^{1/2}(1-2C_1) \qquad (3.11)$$

kd is expressed as a function of $C_1$ in Fig. 3.5. In mode 1, kd assumes its maximum denoted as $(kd)_1$ at $C_1 = -u_1$ and decreases monotonically to zero as $C_1$ increases.

In mode 2, the potential $\Phi$ is given as the root of the equations

$$w^3 - 3C_1 w + kz - C_2 = 0 \qquad 0 \leq z \leq z_2 \qquad (3.12)$$

$$w^3 - 3C_1 w - (kz - C_2) = 0 \qquad z_2 \leq z \leq d \qquad (3.13)$$

$C_1$ is obtained by solving the equation

$$kd = (1+C_1)^{1/2}(1-2C_1) + (u_1+C_1)^{1/2}(u_1-2C_1) \qquad (3.14)$$

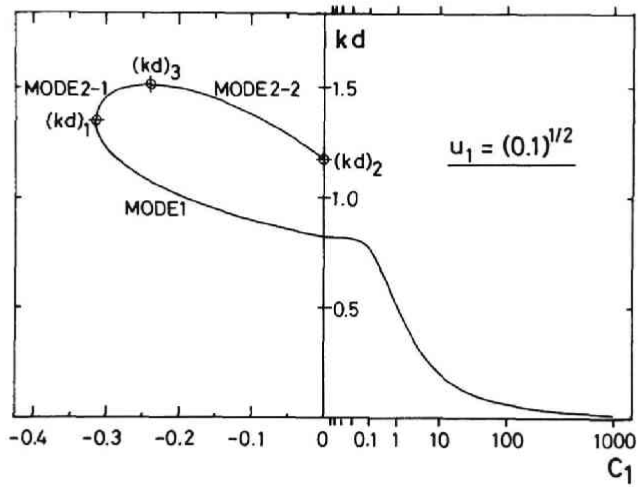


Fig. 3.5
Relation between space charge effect parameter kd and integration constant $C_1$.

$C_2$ is also given by eq. (3.11) and $z_2$ is expressed as

$$z_2 = C_2 / k \qquad (3.15)$$

Figure 3.5 also shows kd given by eq. (3.14). In mode 2, kd reaches a maximum denoted as $(kd)_3$ at $C_1 = -u_1/(1+u_1)$ where mode 2 is devided into mode 2-1 and mode 2-2. As shown in Fig. 3.5 mode 2-1 is bounded by $C_1 = -u_1$ at which kd assumes $(kd)_1$, and mode 2-2 is bounded by $C_1 = 0$ at which kd assumes $(kd)_2$.

Figure 3.6 shows $(kd)_1$, $(kd)_2$ and $(kd)_3$ as a function of $u_1$. Since $(kd)_3$ is always larger than $(kd)_2$, $(kd)_3$ determines the maximum current density $J_{max}$ that can be decelerated from $\Phi_o$ to $\Phi_1$.

$$J_{max} = (kd)_3^2 J_s = (1 + u_1)^3 J_s \qquad (3.16)$$

For example, under the condition of $\Phi_o$ = 30 keV, $\Phi_1$ = 20 eV, d = 5 cm and m = 105 amu ($Pd^+$), $J_{max}$ assumes 1.1 $mA/cm^2$, which corresponds to a deposition rate of 60 nm/min (see Figs. 3.1 and 3.3). As can be understood from eq. (3.5), $J_{max}$ can be increased by increasing the initial ion energy $\Phi_o$ or decreasing the gap distance d. Figure 3.7 shows an example of the potential distribution corresponding to several values of current density. Although Figs. 3.5 and 3.6 indicate that mode 2-2 may exist simultaneously with mode 1 and mode 2-1 for a given kd, it cannot exist in reality because of relatively high electrostatic energy stored in the field.

In order to evaluate the beam divergence during deceleration under the condition shown in Fig. 3.4 (b), the following beam radius equation is used.

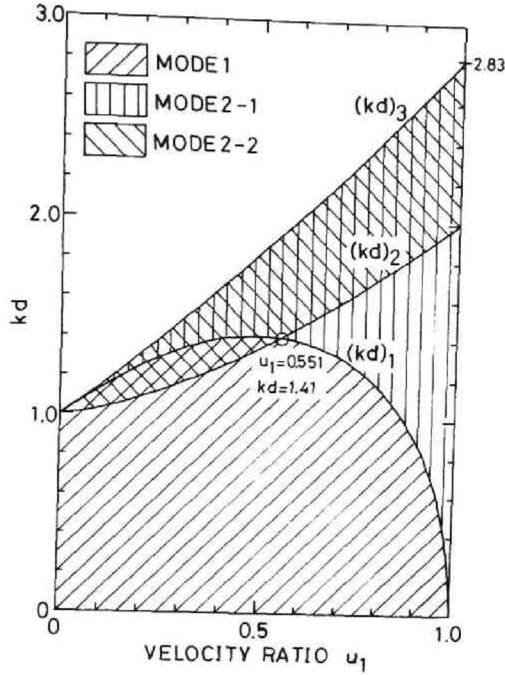


Fig. 3.6
Characteristic (kd)s as a function of $u_1$, ratio of initial and final velocities.

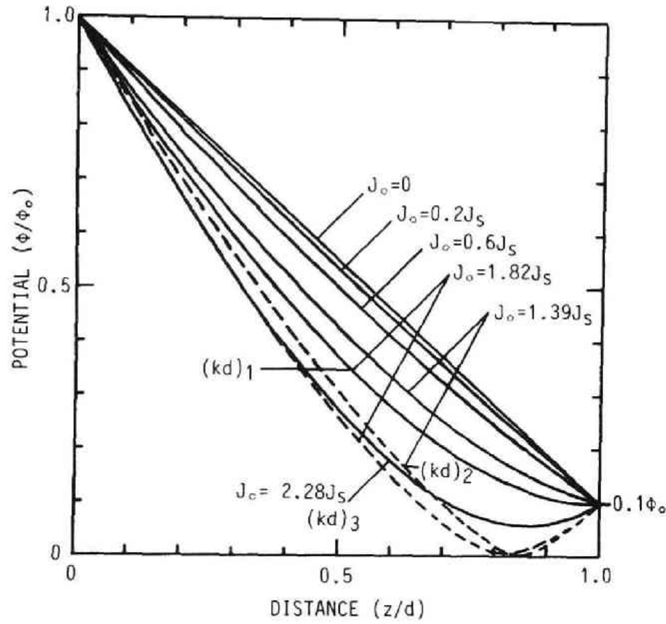


Fig. 3.7
An example of potential distribution induced by space charge effect, corresponding to several values of current density for $u_1 = (0.1)^{1/2}$.

$$\frac{d^2\xi}{d\eta^2}+\frac{1}{2\psi}\frac{d\psi}{d\eta}\frac{d\xi}{d\eta}+\frac{1}{4\psi}\frac{d^2\psi}{d\eta^2}\xi-\left(\frac{kd}{3}\right)^2\frac{1}{\psi^{3/2}}\frac{1}{\xi}=0 \qquad (3.17)^*$$

where

$$\xi=R/R_0,\ \ \eta=z/d,\ \ \psi=\Phi/\Phi_0 \qquad (3.18)$$

This equation is numerically solved for a given potential distribution $\Phi(z)$ under the initial condition

$$\xi=1,\ \ d\xi/d\eta=0 \qquad \text{at} \qquad \eta=0 \qquad (3.19)$$

This means that the beam is parallel at the entrance and its original radius is $R_O$. Figure 3.8 shows the increase of beam radius under the linearly gradient potential, that is

$$\Phi=(\Phi_0-\Phi_1)[1-(z/d)]+\Phi_1 \qquad (3.20)$$

Figure 3.9** is for the potential which is proportional to the 4/3 power of the distance from the end side, that is

$$\Phi=(\Phi_0-\Phi_1)[1-(z/d)]^{4/3}+\Phi_1 \qquad (3.21)$$

---

Note:

*) Derivation of this equation appears in Appendix A.1.

**) In this figure, $R/R_O$ is less than unity where kd is small. This is because the potential distribution expressed as eq. (3.21) acts as a focusing lens as is understood from the fact that the second derivative of $\Phi(z)$ is positive. However, such a $\Phi(z)$ does not exist under the condition shown in Fig. 3.4 (b) when kd is small, and even when kd is large, the potential distribution does not act as a focusing lens owing to increased space charge.

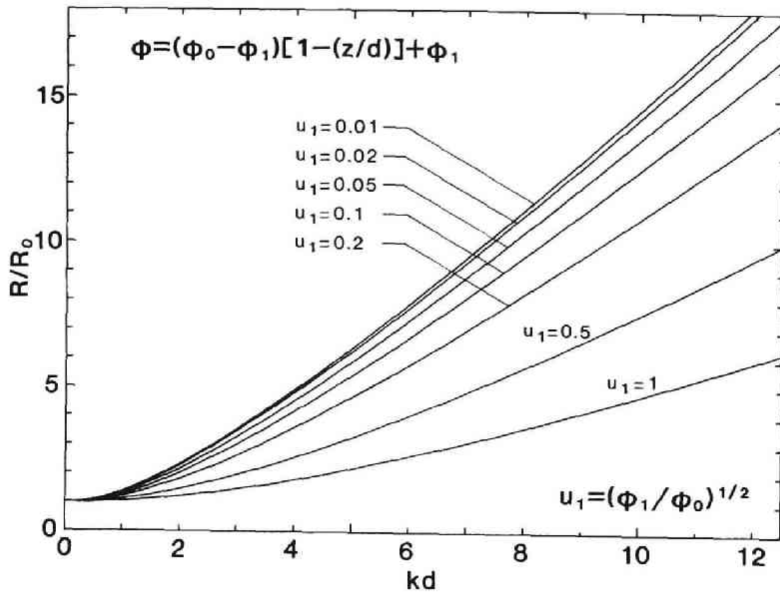


Fig. 3.8
Increase of beam radius under a linearly gradient potential distribution.

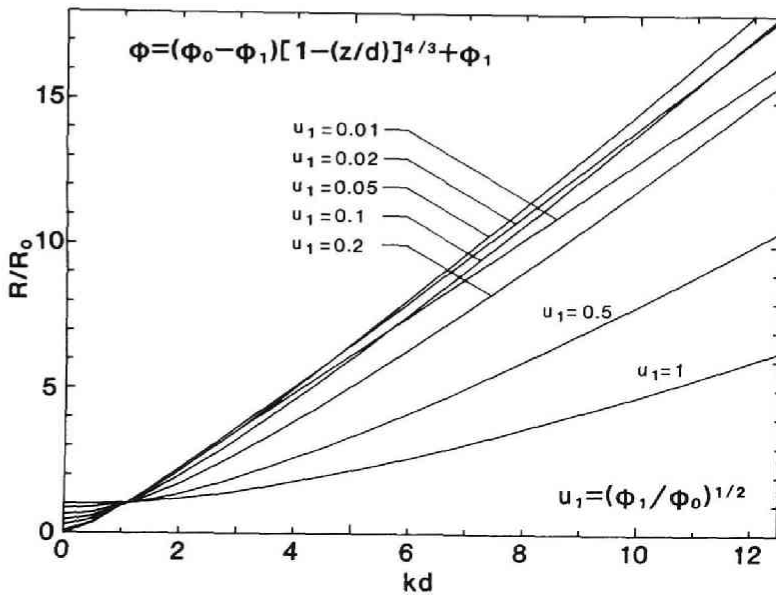


Fig. 3.9
Increase of beam radius under a potential distribution proportional to the 4/3 power of the distance from the end side.

which can be associated with the potential distribution in a planar space-charge-limited diode. It should be noted that in both cases the degree of beam divergence during deceleration ($u_1 < 1$) is on the same order as that during transport in a equi-potential space with the initial beam energy $\Phi_o$ ($u_1 = 1$). Thus a low-energy ion beam can be efficiently obtained by combining high-energy ion beam transport and deceleration of the ion beam just in front of the target.

A practical deceleration system shown in Fig. 3.4 (c) is used in the deposition experiments. This is basically a two-element aperture lens, in which a beam is defocused near the first aperture and is focused near the second aperture. Since the beam is almost fully decelerated near the second aperture, the beam is efficiently focused. Thus the beam divergence due to the space charge effect and the defocusing lens near the first aperture can be corrected by adjusting $\delta$ in Fig. 3.4 (c). The ion trajectories in the deceleration system were numericallly calculated by using a computer program originally developed by Dr. J. Ishikawa (Department of Electronics, Kyoto University) and Dr. F. Sano (Plasma Physics Laboratory, Kyoto University), and later adapted by S.C. Cheng (University of Wuhang, China) for deceleration systems. In the program, space charge effect is taken into account by repeated calculation of electric field, ion trajectories and space charge. Figure 3.10 shows the ion trajectories and the equipotential lines for various aspect ratios $\delta/D$ when a $^{108}Ag^+$ beam of 20 μA (6.4 μA/cm2) is decelerated from 30 keV to 20 eV. Since the beam current is considerably smaller than $J_s$ (1.1 mA/cm2), space charge effect is negligible as long as the $\delta/D$ is small and therefore the divergent beam is gradually focused as the $\delta/D$ is increased. When $\delta/D$ is large, the beam blows up and some of the ions are accelerated backward. Compared with the trajectories obtained without the space charge correction (Fig. 3.10 (f)), it is found that the beam blow-up is caused by

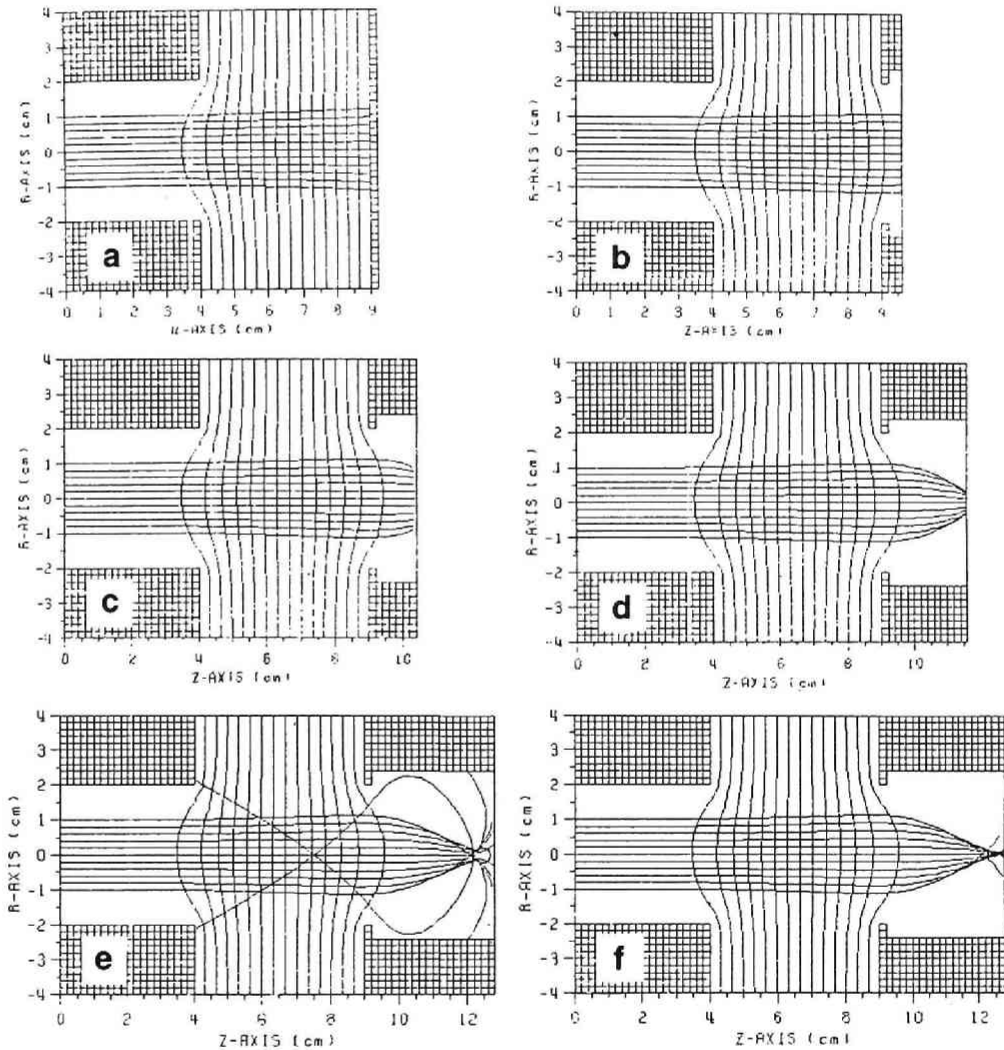


Fig. 3.10

Calculated ion trajectories and equipotential lines under the condition that a $^{108}Ag^{+}$ beam of 20 µA is decelerated from 30 keV to 20 eV. Aspect ratios $\delta/D$ are 0 (a), 0.15 (b), 0.35 (c), 0.65 (d), 0.95 (e) and 0.95 (f), respectively. (e) and (f) are in the same condition except that in (f) space charge effect is not corrected.

the space charge effect resulting from the large transport length at low energy and from increased space charge density due to focusing of the beam.

Set-up of an experimental deceleration system is shown in Fig. 3.11. This is the same as that used in film deposition experiments except that the elimination of high-energy neutrals and secondary electrons is not considered. A hot-filament hollow cathode ion source equiped with a high-temperature oven (Model 911A, Danfysik/High Voltage Engineering, Burlington, U.S.A.) is used as an ion source. This source is characterized by its high-temperature operation (1700°C max.) which realizes the production of heavy metal ions such as $Ag^+$ and $Pd^+$, and by low discharge voltage (20 - 50 eV) which results in low energy spread beams. The ions are extracted by 30 kV, focused by an einzel lens, and mass-analyzed by a sector-type magnet whose mass resolution $M/\Delta M$ is larger than 100. Figure 3.12 shows an example of the deceleration behavior. Using a simple aperture lens deceleration system, a 30 keV $Ag^+$ beam of 22 μA can be decelerated to 10 eV with little loss in intensity when $\delta/D$ is 0.1. Onset of beam current decrease seems to be at a somewhat higher energy when $\delta/D$ is 0.6 and 0.9 considering the results shown in Fig. 3.10. This is probably because the beam is already divergent at the entrance and therefore the beam divergence during deceleration is enhanced by refraction. Another reason is the existence of the transverse components of the ion velocity which are observed as the beam energy spread.

### 3.2.3 Other Problems Related to Ion Beam Deceleration

High-energy neutrals produced by charge exchange collisions between ions and residual gas atoms may hit the substrate and cause damage. Figure 3.13 shows 1.5-MeV $He^+$ channeling spectra of Si(111) wafers bombarded by 50 eV, 300 eV and 1 keV $Ar^+$ ions to a dose of $5 \times 10^{16}$ $cm^{-2}$ using the apparatus shown in Fig. 3.11.

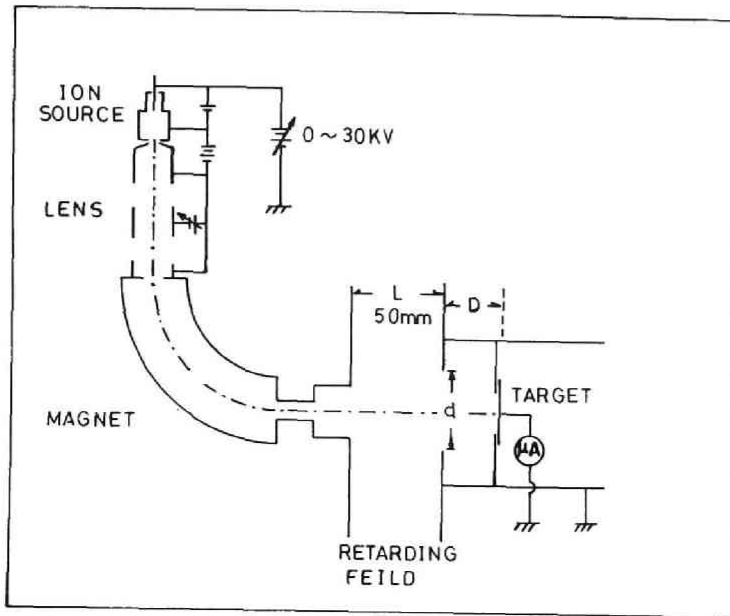


Fig. 3.11
Set-up of experimental ion beam equipment used to evaluate the deceleration behavior of the beam.

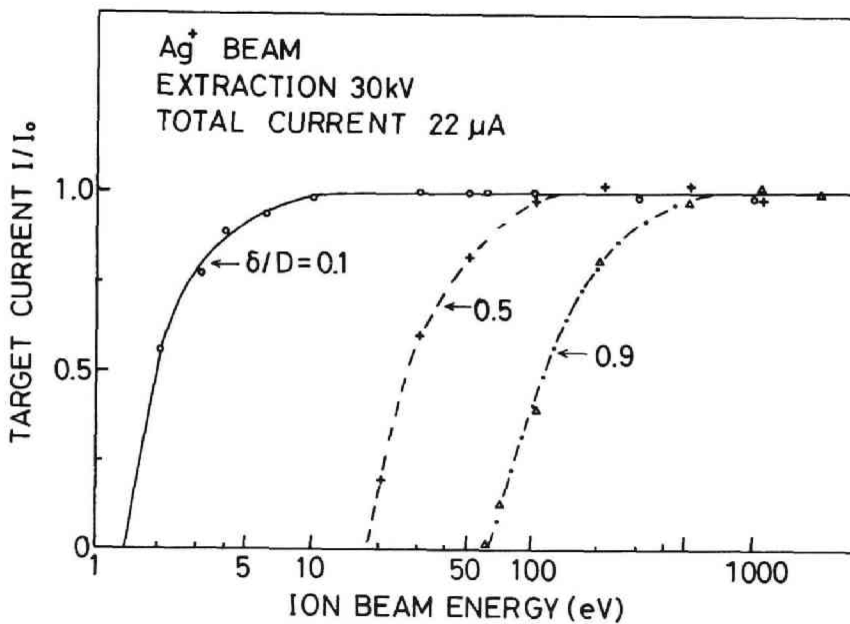


Fig. 3.12
Current-energy characteristics of the experimental ion beam equipment shown in Fig. 3.11.

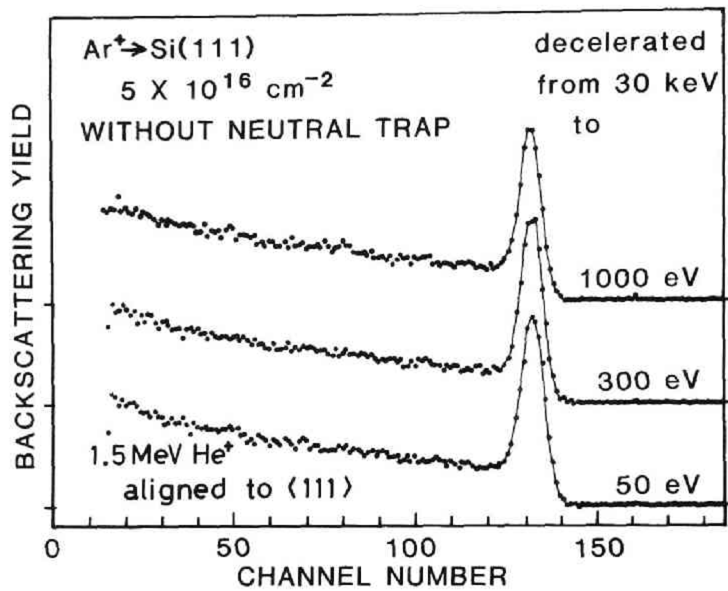


Fig. 3.13
1.5-MeV $He^+$ channeling spectra of Si(111) wafers bombarded by 50-eV, 300-eV and 1-keV $Ar^+$ ions using apparatus shown in Fig. 3.11.

The damage peaks in these spectra are almost the same in height and width regardless of ion energy, indicating that the damage is produced by particles which are not influenced by decelerating electric field, ie. high-energy neutrals. Let us consider the case where singly charged ions collide with residual gas atoms and are changed into neutrals. Fraction $F_0$ of energetic neutrals in a beam, fraction $F_1$ of singly charged ions, and transport distance z (cm) are related by the following equations.

$$\frac{dF_0}{dz} = \frac{P}{1.01 \times 10^5} \frac{273.15}{T} L \sigma_{10} F_1 \qquad (3.22)$$

$$F_1 + F_0 = 1 \qquad (3.23)$$

where

P: pressure of the residual gas (Pa)

T: temperature of the residual gas (K)

$\sigma_{10}$: cross section for a charge exchange collision ($cm^2$)

L: Loschmidt's number ($2.69 \times 10^{19}$ $cm^{-3}$)

For example, $P = 5 \times 10^{-4}$ Pa, Z = 30 cm, $\sigma_{10} = 5 \times 10^{-16}$ $cm^2$,[36) T = 300K yields 0.2 % of energetic neutrals in a beam. Since energy of the neutrals (a few tens of keV) is much larger than that of the decelerated ions (less than a few hundred eV), such a fraction of high-energy neutrals can have a serious effect on the target. Deflection of the beam and decrease of residual gas pressure are effective in eliminating the high-energy neutrals. The former approach is taken in the following deposition experiments.

Secondary electrons generated when ions hit apertures (slits) or walls on the high-energy side are accelerated toward the target during ion deceleration and cause error in beam current measurement, temperature rise of the target and damage to a certain target material sensitive to electron bombardment.[37)]

These secondary electrons can be suppressed electrostatically and trapped magnetically.

Secondary electrons and ions emitted from the target may cause error in beam current measurement. However, these secondary electrons are automatically suppressed by the electric field for ion deceleration and the secondary ions produced by low-energy ion bombardment can be neglected because of the small yield.

Figure 3.14 shows the deceleration electrode system used in the deposition experiments. The incident ion beam which has been decelerated from 30 keV to 8 keV beforehand is deflected by an electric field between plates to eliminate high-energy neutrals. Secondary electrons emitted from the defining aperture placed after the deflector are suppressud by a negative electric potential (-320 V) and those emitted from other places are trapped by a transverse magnetic field (200 G). Figure 3.15 shows the result of secondary electron elimination. By using the magnetic trap and the electrostatic suppressor, the number of incident electrons is reduced to one-fortieth of the original value. It is to be noted that the ion current is not zero even if the beam energy is zero. Since the beam energy here is defined as the acceleration voltage applied between the target and the ion source anode, the true beam energy can be higher than the nominal beam energy if ions have an initial energy. In fact, the potential of the ion-emitting plasma boundary is slightly higher than that of the anode, because the anode potential is not enough to reflect ions,[2] resulting in an appreciable initial energy. From now on, the nominal beam energy will be used without notice.

### 3.2.4 Ion Beam Engineering Experimental System

The low-energy ion beam equipment above and a high-energy beam line are combined to construct the Ion Beam Engineering Experimental System installed in Kyoto University, which is shown

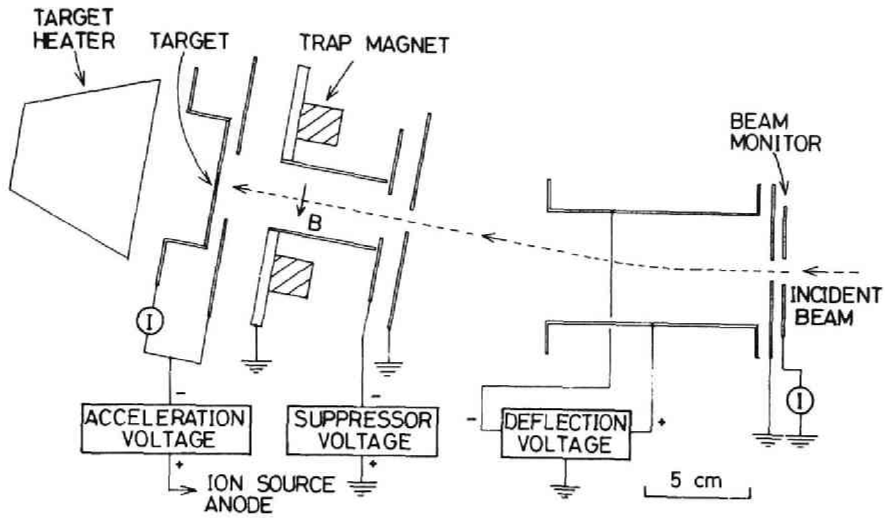


Fig. 3.14
Schematic diagram of the deceleration electrode system for ion beam deposition.

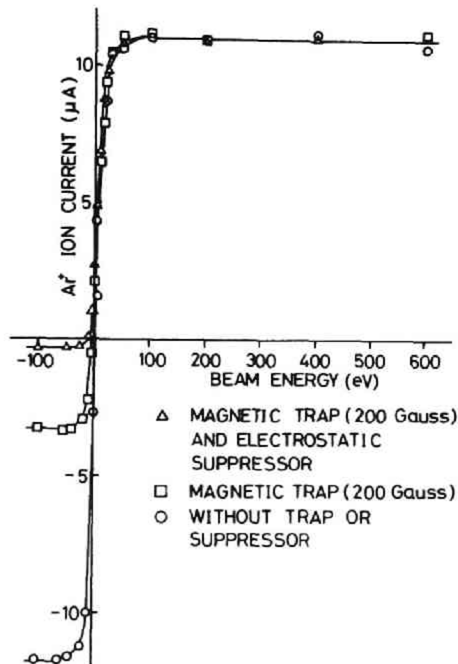


Fig. 3.15
Effect of secondary electron elimination on the current-energy characteristics of the ion beam deceleration system.

schematically in Fig. 3.16. The high-energy beam line (the upper line with acceleration tube) is to produce ions of 30 keV - 400 keV and the low-energy beam line (the lower line with deceleration electrode system) is to produce ions of 10 eV - 30 keV. By using both lines, ion energy range from 10 eV to 400 keV is continuously covered.

## 3.3 Formation of Very Thin Films by Low-Energy Ion Beam Deposition

### 3.3.1 Experiment

Using the low-energy beam line of the Ion Beam Engineering Experimental System described in Section 3.2, a single-crystal Si(111) substrate is irradiated by a $^{105}Pd^{+}$ ion beam. Experimental conditions are summarized on Table 3.1. Ion energy is 10 - 400 eV, current is 1 - 3 $\mu A/cm^2$, and beam diameter is 20 mm. The substrate is at room temperature and in a background pressure of 3 - 5 X $10^{-4}$ Pa.

### 3.3.2 Collection Efficiency of Pd on Si

Figure 3.17 shows the energy dependence of the collection efficiency of Pd ions on Si(111). Collection efficiency is defined as the ratio of collected to incident material amounts. The collection efficiency decreases as the ion enenrgy increases, and it decreases more sharply with higher dose irradiation. This is true because the self-sputtering yield of Pd increases as the ion energy increases and the surface concentration of Pd atoms increases as the ion dose increases. A collection efficiency of over 90% is attainable at an ion energy around a few tens of eV. This observation is useful when one needs to deposit materials with high vapor pressure, such as P and As, whose sticking coefficient on the surface is low.

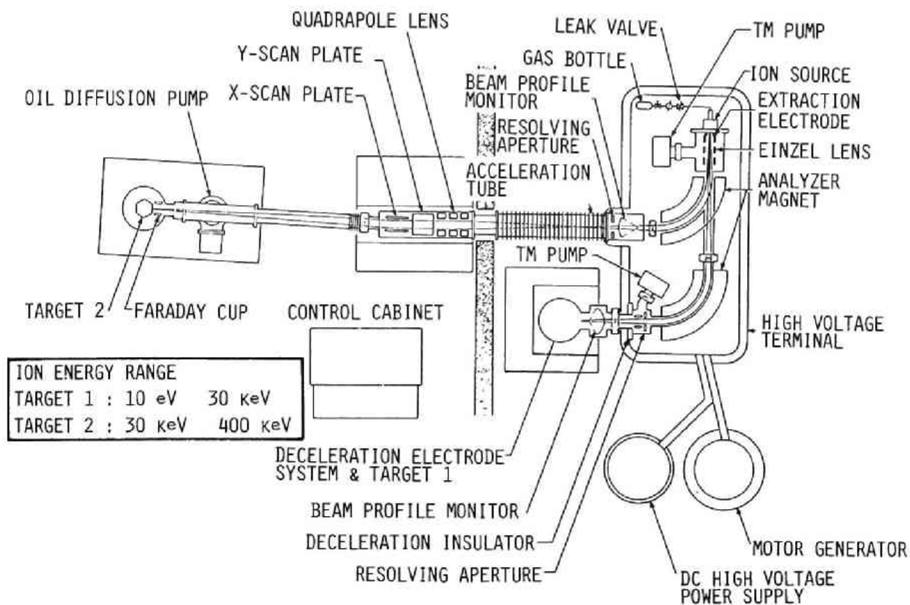


Fig. 3.16
Schematic diagram of the Ion Beam Engineering Experimental System installed in Kyoto University

Table 3.1 Experimental Conditions of Metallization by Low-Energy Ion Beam Deposition.

| | |
|---|---|
| Substrate | Single-Crystal Si(111) |
| Ion Species | $Pd^+$ |
| Energy | 10 - 400 eV |
| Current | 1 - 3 $\mu A/cm^2$ |
| Beam Diameter | 20 mm |
| Substrate Temp. | Room Temp. |
| Background | 3 - 5 X $10^{-4}$ Pa |

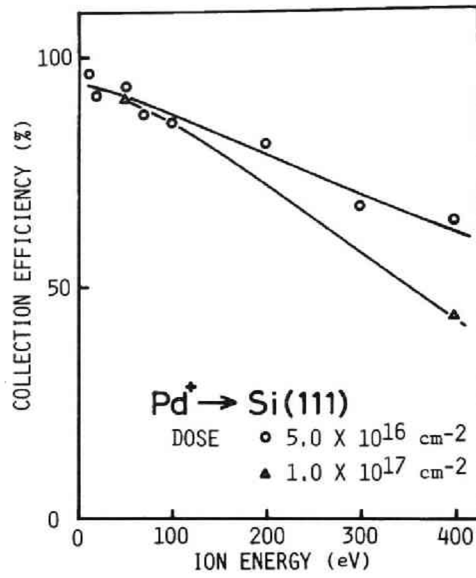


Fig. 3.17
Energy dependence of the collection efficiency of Pd ions on Si(111) surface.

### 3.3.3 Energy Dependence of Film-Substrate Reaction

Energetic ions can be utilized to desorb carbon, oxygen, and other impurities from a substrate surface to make a clean interface and to mix film and substrate materials as well. These effects promote interface reactions between film and substrate. However, energetic ions could cause lattice damage to the substrate and growing film, which would degrade the crystalline quality of the film. Pd is known to react with Si to form silicides, one of which, $Pd_2Si$, grows epitaxially when Si(111) is used as the substrate.[31] The degree of the reaction and the crystalline quality of the silicide is a good measure of the above-mentioned effects of ion beam energy. Figure 3.18 shows the reflective electron diffraction (RED) patterns of ion beam deposited Pd films on Si(111), postannealed at 400°C for 30 min. The film formed by thermally evaporated Pd and that by Pd ions at 20 eV (Fig. 3.18 (b)) are of textured polycrystal showing the lack of interface cleanliness. The film formed by ions at 400 eV (Fig. 3.18 (d)) shows a polycrystalline pattern with little orientation, which seems to be the result of the radiation damage to the film and the substrate. With films formed by ions at the intermediate energy level of 50 - 100 eV (Fig. 3.18 (c)), $Pd_2Si$ grows epitaxially showing the cleanliness of the interface and negligible damage to the crystalline quality. The pattern of Fig. 3.18 (c) is indexed in Fig. 3.19.

### 3.3.4 Resistivity of Ultrathin Films

Figure 3.20 shows the electrical resistivity of films as a function of the Pd film thickness measured by Rutherford back-scattering. Bulk resistivity and the theoretical resistivity corrected for the size effect according to Fuchs' theory are also shown.[38] Ion beam deposited films as thin as a few nanometers have a resistivity of the same order as that of the bulk material. No sharp increase of the resistivity is observed at the lower side

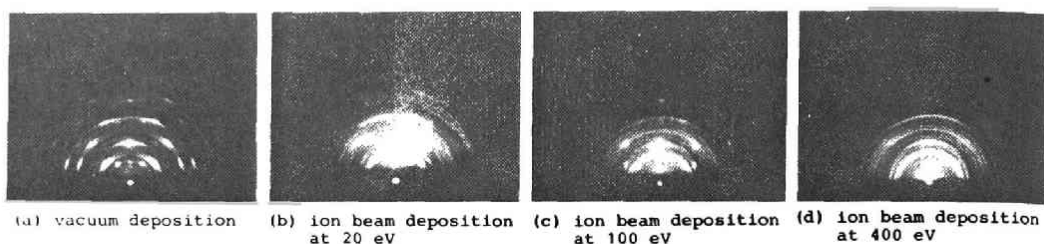


Fig. 3.18
RED patterns from Pd films on Si(111), formed by mass-analyzed ion beam deposition and conventional vacuum deposition, postannealed at 400°C for 30min.

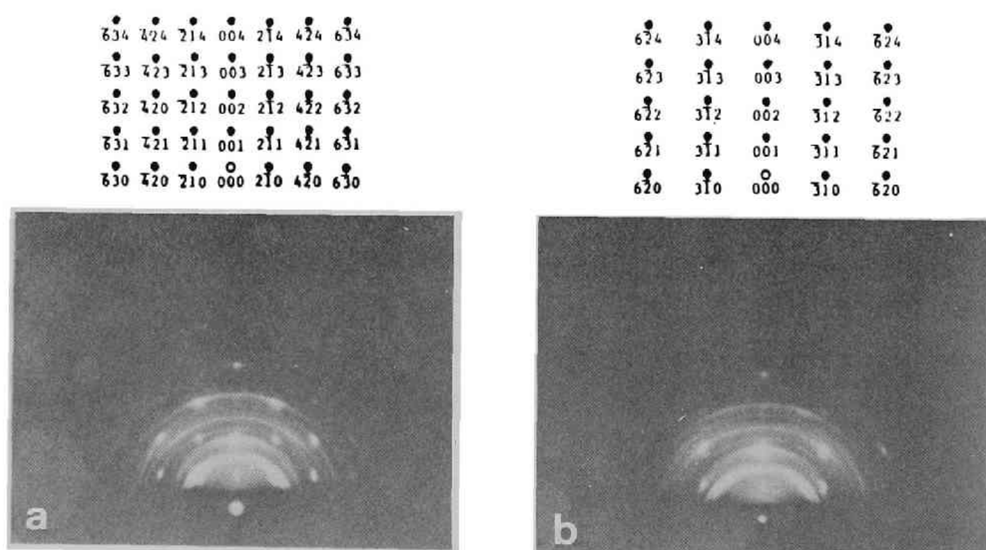


Fig. 3.19
Examination of the pattern in Fig. 3.18 (c). (b) is obtained by a azimuthal rotation of about 11° from the condition (a). Patterns are indexed as hexagonal $Pd_2Si$ with a = 6.49 Å and c = 3.43 Å.

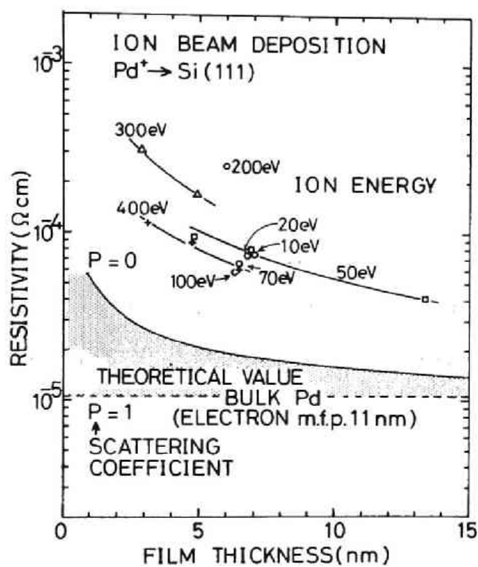


Fig. 3.20

Relation between resistivity and thickness of Pd films formed by mass-analyzed ion beam deposition on Si(111).

of the thickness range shown in Fig. 3.20, which indicates that films are already continuous. In the early stage of ion beam deposition, the arriving ions are shallowly implanted, and the surface defects created by ion impact work as preferential nucleation sites, so that the number of nuclei increases and agglomeration of adatoms into large islands is prevented. This can be clearly seen in the transmission electron micrographs of the early stage of Pd ion beam deposition on Si, as shown in Fig. 3.21. With conventional vacuum deposition, the film has an island structure at this stage of film formation, whereas the film deposited by ions at 10 eV consists of much smaller islands and the films deposited at 50 eV, 100 eV, or more have a continuous structure constructed with small grains.

### 3.3.5 Observation by Auger Electron Spectroscopy

That a very thin and continuous film is formed by low-energy ion beam deposition is further confirmed by Auger electron spectroscopy (AES). Fig. 3.22 shows differentiated Auger spectra of ion beam deposited Pd films whose original thickness is about 6 nm, sputter etched by 2 nm just before AES measurement. Spectra of pure Si, Pd, and $Pd_2Si$ are also shown in Fig. 3.22 as references. In the case of films deposited at the energy level of 20 - 200 eV, Auger peaks corresponding only to Pd can be seen in the spectra, which shows that the substrate is fully covered with Pd films even in such thin films. In the case of a film deposited at 400 eV, a $Si_{LVV}$ Auger peak which is splitted off into four[39] and different from that of pure Si can be seen. This indicates that the $Si_{LVV}$ peaks are not from the Si substrate not covered by the Pd film, and that a silicide intermediate layer is formed under the film surface. The formation of a silicide layer at the interface would be due to the intermixing of the substrate and the film materials by energetic ions, and also due to the

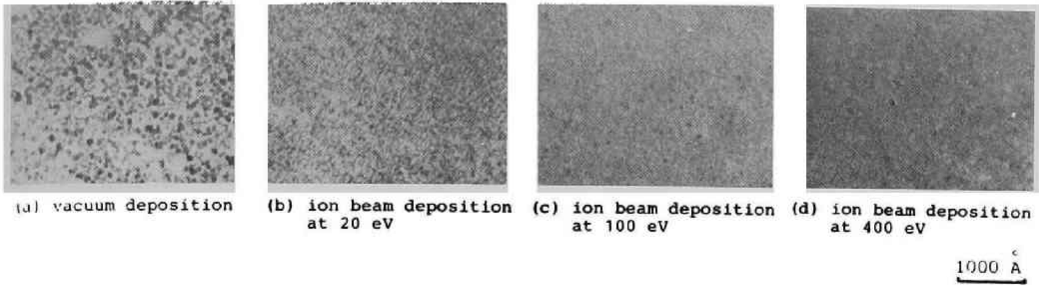


Fig. 3.21
Electron micrographs of Pd films on Si(111), formed by mass-analyzed ion beam deposition and conventional vacuum deposition.

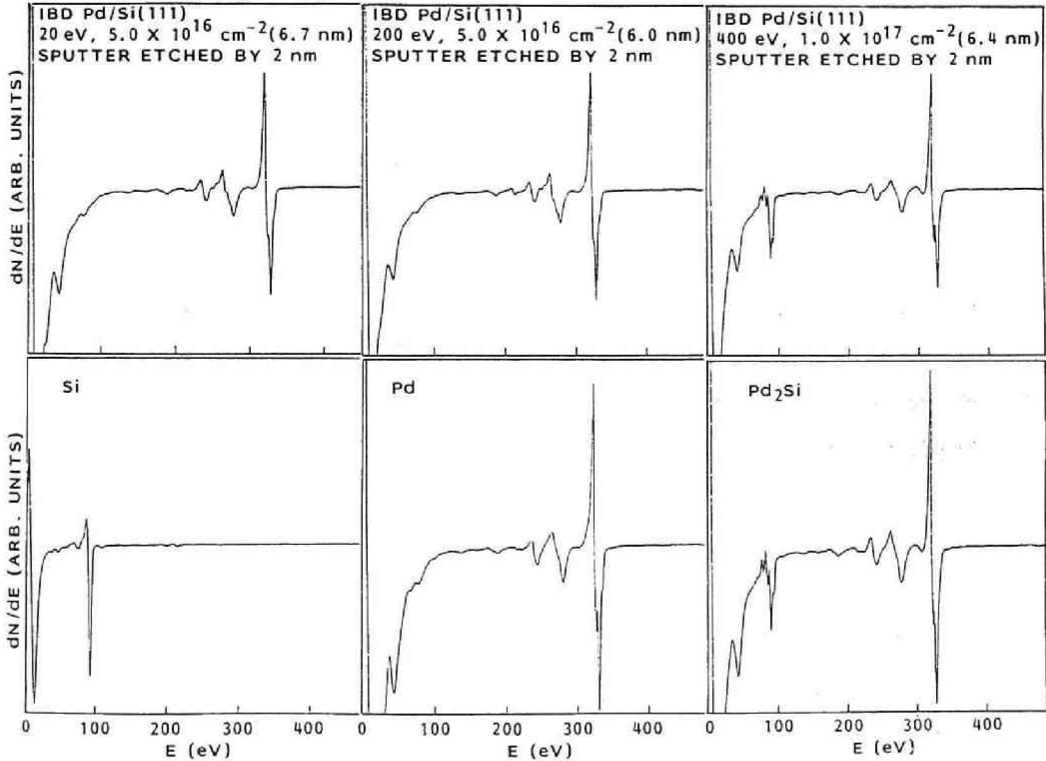


Fig. 3.22
Auger spectra of Pd films deposited on Si(111) by mass-analyzed ion beams at various energies and those of pure Si, Pd, and $Pd_2Si$.

activation of chemical reactions by ionization (see Chap. 2).

### 3.3.6 Selective Deposition on Conductor

During ion beam deposition, insulators such as $SiO_2$ on Si are charged up to high enough potentials to prevent the entrance of low-energy ions. This phenomenon is confirmed with a 660-nm layer of oxidized silicon, etched into a line-and-space pattern with a 400-μm period, used as the substrate. Line analysis by Auger electron spectroscopy of the samples deposited at 70 eV and 400 eV with a $1.7 \times 10^{16}$ $cm^{-2}$ dose is shown in Fig. 3.23. At 70 eV, Pd is deposited with high selectivity. On the contrary Pd is deposited almost uniformly at 400 eV. Figure 3.24 shows the dependence of the selectivity on ion energy. Selectivity reaches a maximum at around 70 - 100 eV and decreases on both sides. The decrease of the selectivity on the high-energy side is probably caused by increase in leakage current in $SiO_2$ due to voltage increase at the surface or decrease in electrical resistance at the $SiO_2$ surface due to ion irradiation. It is estimated that the decrease of the selectivity on the low-energy side is caused by screening of Si surface potential by the charges on the $SiO_2$.

## 3.4 Formation of Buried Conductive Layers by High-Dose Ion Implantation

### 3.4.1 Experiment

Pd, Ag, and Al ions are selected as the ion species and single-crystal Si(100) as the target. Pd is known to form silicides which are stable in contact with Si and useful in device applications.[32] Ag, which has nearly the same mass as Pd and does not form any compounds with Si, can serve as a good contrast to Pd.[40] Al has been thoroughly studied as a dopant. Experimental conditions are summarized in Table 3.2. The ion beam energy is 320 keV for Pd, 320 keV for Ag, and 73 keV for Al

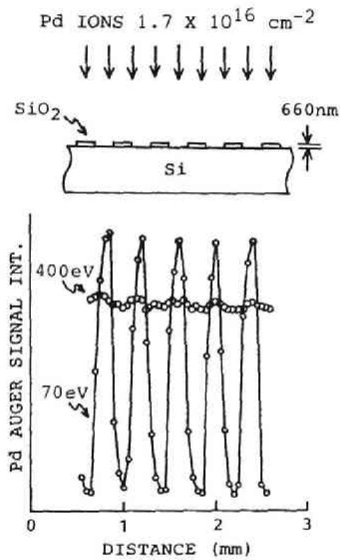


Fig. 3.23
AES line analysis of ion beam deposited Pd on a $Si-SiO_2$ line-and-space pattern.

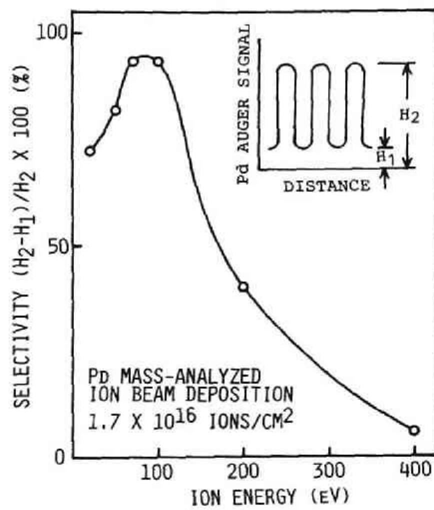


Fig. 3.24
Selectivity of ion beam deposition on conductor as a function of ion energy.

Table 3.2 Experimental Conditions of Metallization by High-Dose Ion Implantation.

| | |
|---|---|
| Target | Si(100) and Si(111) |
| Ion Species | $Pd^+$, $Ag^+$ and $Al^+$ |
| Energy | 320*keV for $Pd^+$<br>320 keV for $Ag^+$<br>73 keV for $Al^+$ |
| Projected Ion Beam Range | 130 nm (for all three) |
| Current | a few $\mu A/cm^2$ |
| Dose | $5 \times 10^{16} - 4 \times 10^{17}$ $cm^{-2}$ |
| Target Temp. | 20 - 100°C |
| Background | $4 \times 10^{-5}$ Pa |

* 50 - 400 keV in additional experiments.

with a projected ion beam range in Si of 130 nm for all three.[41] Ion current is a few $\mu A/cm^2$, and the dose is varied from 5 X $10^{16}$ to 5 X $10^{17}$ $cm^{-2}$. Implantation is performed at room temperature in a vacuum of less than 4 X $10^{-5}$ Pa and samples are postannealed at various temperatures. In addition to these experiments, ion energy is varied from 50 to 400 keV in the case of Pd implantation and results are compared.

### 3.4.2 Depth Profile of the Implanted Metal

Depth profiles are measured by Rutherford backscattering and Auger electron spectroscopy combined with sputter etching. Figures 3.25 - 3.27 are the annealing behaviors of the buried conductive layer. Figure 3.25 is the 1.5-MeV $He^+$ Rutherford backscattering spectra of the samples implanted with Pd ions to a dose level of 2.0 X $10^{17}$ $cm^{-2}$ and postannealed at various temperatures in vacuum for 30 min. It is noticeable that the distribution of Pd does not change drastically and the peak concentrations are almost the same after an anneal of 300, 600, and 800°C. This is probably due to the thermal stability and low mobility of Pd silicide in Si.[32] In contrast, as shown in Fig. 3.26, implanted Ag is diffused away in accordance with the annealing temperature. Figure 3.27 shows depth profiles of the samples implanted with Al ions, measured by Auger electron spectroscopy. Al is also diffused appreciably after an anneal of 500 or 700°C. Surface enrichment or out-diffusion of implanted species after annealing is characteristic in Al and Ag implanted samples. This phenomenon is observed quite commonly in ion-implanted semiconductors. The cases of Sb, Se and Cd implanted Si,[42] N and Al implanted Si to much lower doses, and C and Mg implanted Ge[43] are reported.

Another observation is that the peak concentrations of Ag and Al exceed 50 at.% in as-implanted samples at dose level of 4 X $10^{17}$ $cm^{-2}$ (Figs. 3.26 and 3.27), whereas the peak concentration of

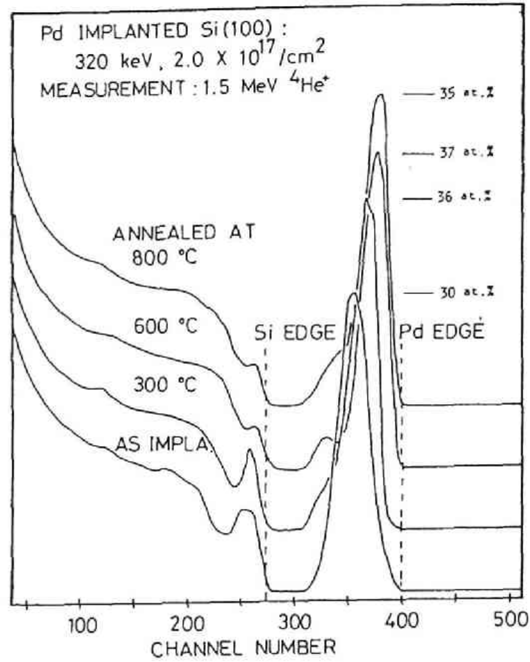


Fig. 3.25
RBS spectra of Pd-implanted (320 keV, 2.0 X $10^{17}$ $cm^{-2}$) Si(100), postannealed at various temperatures.

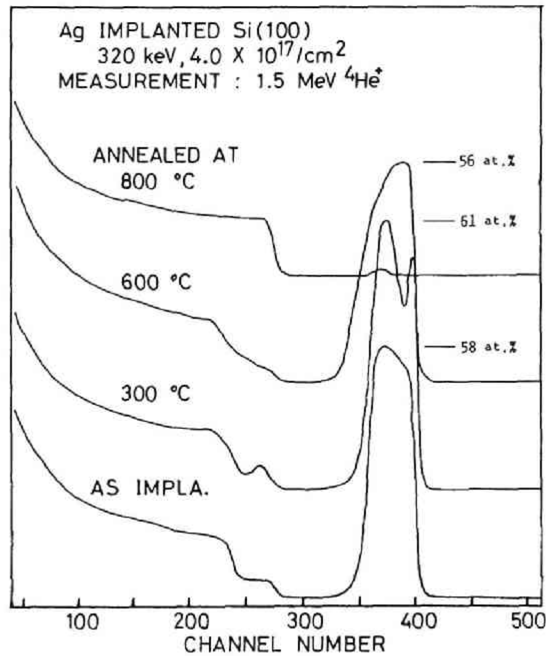


Fig. 3.26
RBS spectra of Ag-implanted (320 keV, 4.0 X $10^{17}$ $cm^{-2}$) Si(100), postannealed at various temperatures.

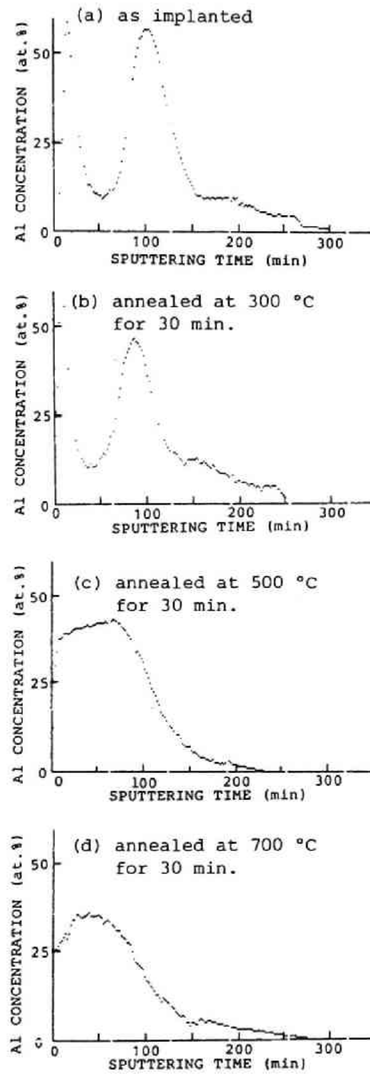


Fig. 3.27
Al concentration profiles of Al-implanted (73 keV, $4.0 \times 10^{17}$ $cm^{-2}$) Si(100), postannealed at various temperatures, measured by AES with sputter etching.

Pd is about 30 at.% at dose level of 2 X $10^{17}$ $cm^{-2}$ (Fig. 3.25) and is found to saturate at about 40 at.% at dose level of 3 X $10^{17}$ $cm^{-2}$. This difference in attainable peak concentrations can be attributed to larger increase in total sputtering yield of Pd-implanted Si.

### 3.4.3 Collection Efficiency and Collected Amount of Implanted Pd

As mentioned earlier, attainable concentration of the implanted species is restricted by the sputtering process. Fig. 3.28 shows collection efficiency and collected amount of Pd implanted in Si, measured by 1.5-MeV $He^+$ Rutherford backscattering. Here, collection efficiency means the ratio of collected to incident material amounts. Collection efficiency is nearly 100 % to the dose level of 2 X $10^{17}$ $cm^{-2}$. Above this level, efficiency gradually decreases because a Pd-rich layer appears at the front as the surface recedes due to sputtering and Pd itself comes to be sputtered away. It is somewhat curious that in a dose range between 3 X $10^{17}$ $cm^{-2}$ and 4 X $10^{17}$ $cm^{-2}$, collected amount decreases when implanted dose increases. This phenomenon can be attributed to the following two incidences.

(1) Pd concentration becomes high because the sputtering yield of Si is low and it takes high dose for the Pd-rich layer to appear at the surfacxe.

(2) Sputtering yield of the Pd-rich layer is high because the contained Pd, whose mass is large, contributes to large stopping power of the layer for incident ions.

In order to clarify the phenomenon, a simple computer simulation is performed. Figure 3.29 shows the flow chart of the calculation and the assumptions made in it. The total number of implanted ions is divided into small doses. For each dose, distribution of newly implanted Pd is calculated using Gaussian distribution ($R_p$ = 130 nm, $\Delta R_p$ = 40 nm for 320-keV $Pd^+$ ion)[41] and is added to the former concentration profile. Range shorten-

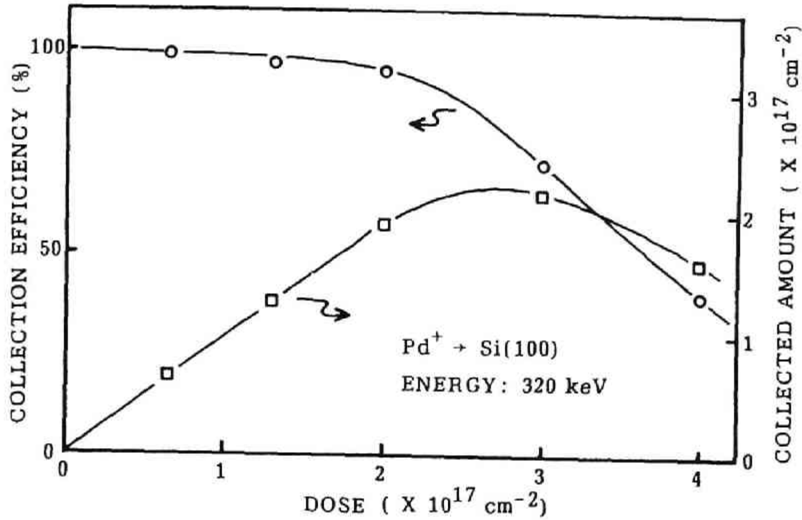


Fig. 3.28
Collection efficiency and collected amount of Pd implanted into Si at 320 keV, as a function of dose.

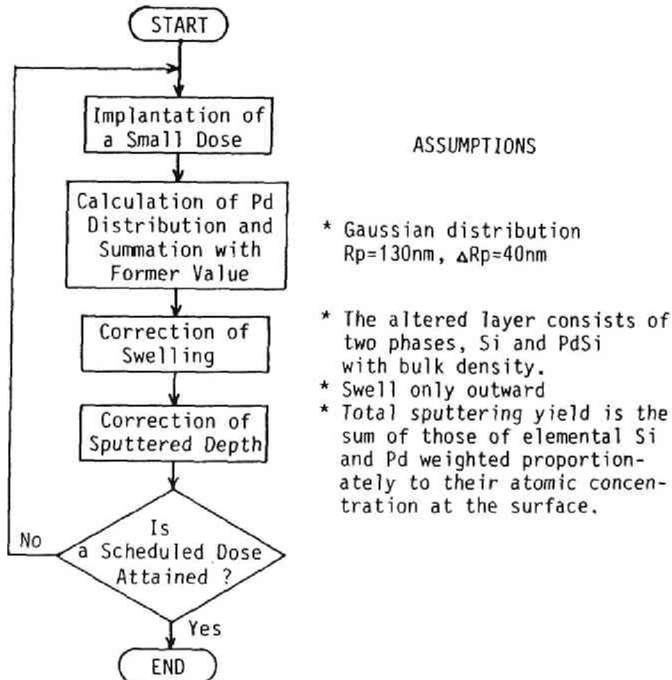


Fig. 3.29
Flow chart of the computer simulation of high-dose implantation and the assumptions made in it.

ing[44] due to the increased Pd concentration is not considered. Next, swelling of the implanted layer is corrected for on the assumption that the layer swells only outward in the direction normal to the surface and the implanted Pd exists as PdSi (see Section 3.4.4) with bulk density. Lastly, the recession of the surface due to sputtering is calculated, where the total sputtering yield is considered to be the sum of the elemental sputtering yield of Si ($Y_{Si}$) and that of Pd ($Y_{Pd}$), weighted proportionately to their atomic concentrations at the surface ($C_{Si}$ and $C_{Pd}$, respectively).

$$Y_{total} = ( C_{Si}\, Y_{Si} + C_{Pd}\, Y_{Pd} ) / ( C_{Si} + C_{Pd} ) \qquad (3.24)$$

The calculations above are repeated until a scheduled dose is attained. Figure 3.30 shows the depth distributions of Pd for various doses. As the dose increases, the position of the concentration peak shifts toward the surface because of sputter etching, and the peak concentration increases at first but decreases at higher doses. Figure 3.31 shows the calculated collection efficiency and collected amount, which agree quite well with the experimental result (Fig. 3.28) indicating that a collected amount may decrease theoretically even when the dose increases.

Some other investigators have also reported a decrease of collected amount as the dose was increased. Almén and Bruce reported the case with Cr and Fe ions in Ta,[45] and Kr ions in Be, Mg, Zn and Hf.[46] Fontell and Arminen reported the case with Cu ions in Al.[2] Their explanations on the phenomenon were different but the phenomenon itself seems to be a quite common one.

### 3.4.4 Phase Identification

X-ray diffractometry is employed to examine the phase structure of the sample. Figure 3.32 shows the traces of the

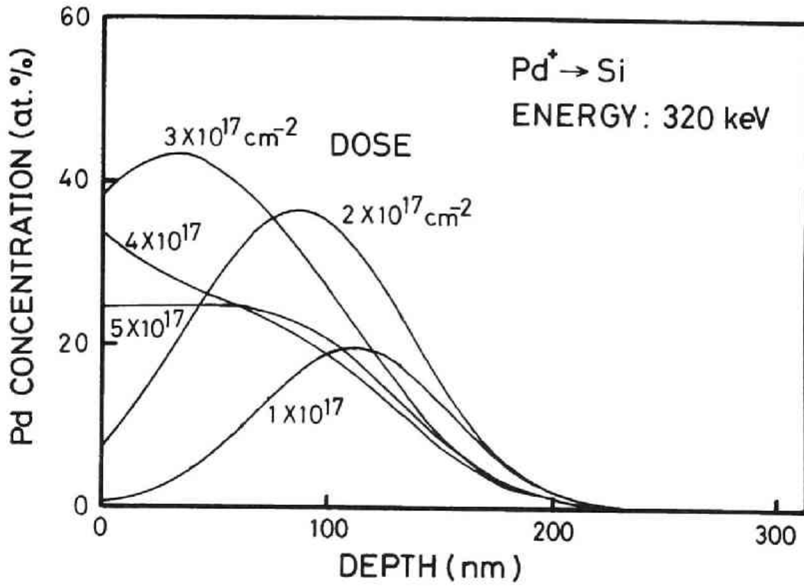


Fig. 3.30
Calculated Pd depth distribution for various ion doses at energy level of 320 keV. Sputtering yields of Si and Pd by Pd ion are assumed to be 2.7 and 20, respectively.

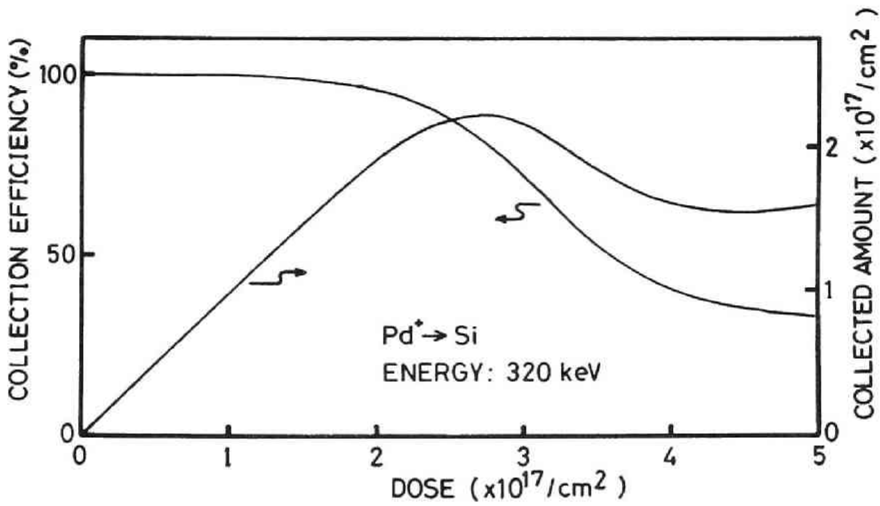


Fig. 3.31
Calculated collection efficiency and collected amount.

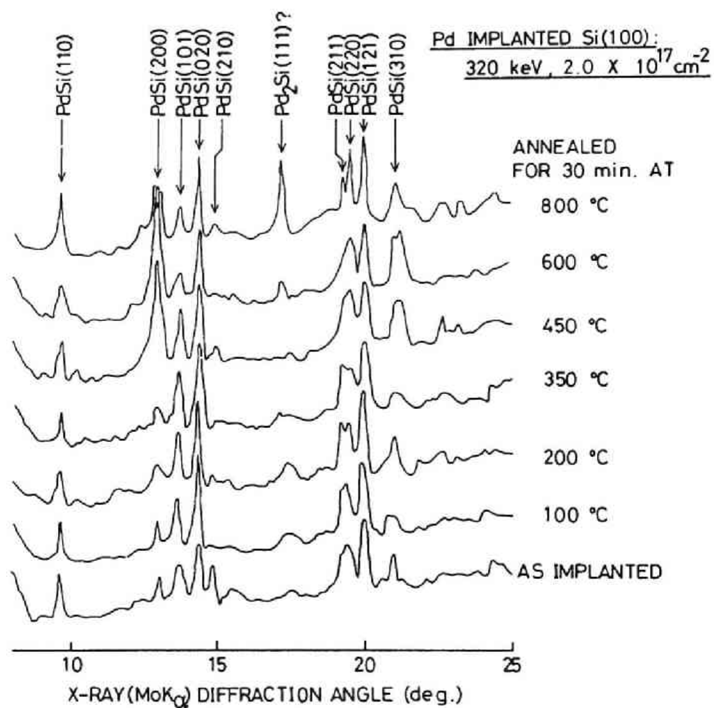


Fig. 3.32
X-ray diffractometer traces of Pd-implanted (320 keV, 2.0 X $10^{17}$ $cm^{-2}$) Si(100), postannealed at various temperatures.

samples implanted with Pd ions to 2.0 X $10^{17}$ $cm^{-2}$ and annealed at various temperatures. The PdSi phase is found in the as-implanted sample. Even though there are slight changes in crystalline orientation, PdSi is the only phase identified up to 800°C. With Ag and Al, which form no compounds with Si and and whose solubilities in Si are small,[40] only the normal Ag and Al phases, respectively, are found.

### 3.4.5 Sheet Resistance of Metal-Implanted Si

Figure 3.33 shows the relationship between dose and sheet resistance for the samples implanted with Pd ions and annealed at 300°C in vacuum for 30 min. Sheet resistance begins to fall near 9 X $10^{16}$ $cm^{-2}$, decreasing sharply to about 6 Ω/□. This means that isolated grains of PdSi begin to connect with each other at that dose.

Figure 3.34 shows the relationship between dose and sheet resistance for Al implantation. Sheet resistance begins to fall near 1.8 X $10^{17}$ $cm^{-2}$, again reaching about 6 Ω/□. The dose level of 1.8 X $10^{17}$ $cm^{-2}$ is twice that with Pd implantation, probably due to the fact that Al does not form conductive compounds with Si. Rapid decrease of resistance is also observed in the case of Ag implantation around the dose level of 2 X $10^{17}$ $cm^{-2}$.

In the usual doping of semiconductors by ion implantation, high-temperature annealing is necessary to activate the heavily doped impurities and to obtain a low resistivity. Figure 3.35 [47] shows an example of the dose dependence of the sheet resistance of Al, B and P implanted Si after annealing at 800°C. From this figure it cannot be expected to get a sheet resistance of less than 100 Ω/□ by Al implantation into Si. However, in the above-mentioned approach, where implanted metals are connected with each other and conduct current as a metallic conductor, resistivity far below that attained by the doping concept can be realized without high-temperature annealing.

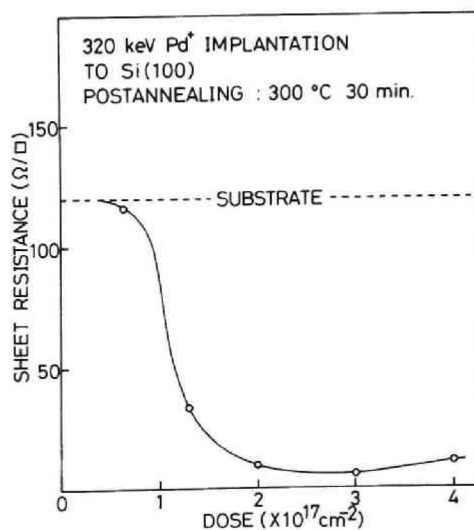


Fig. 3.33
Sheet resistance of 320-keV Pd-implanted Si(100), postannealed at 300°C for 30 min, as a function of dose.

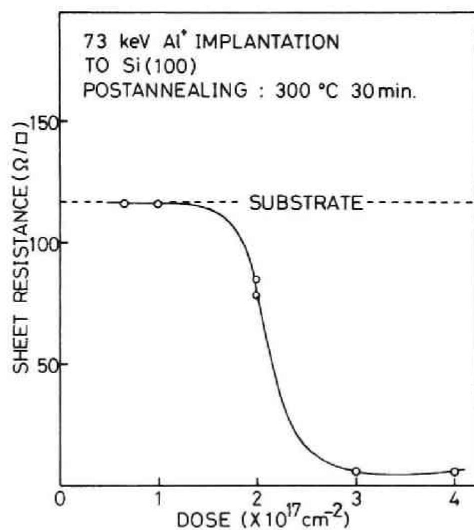


Fig. 3.34
Sheet resistance of 73-keV Al-implanted Si(100), postannealed at 300°C for 30 min, as a function of dose.

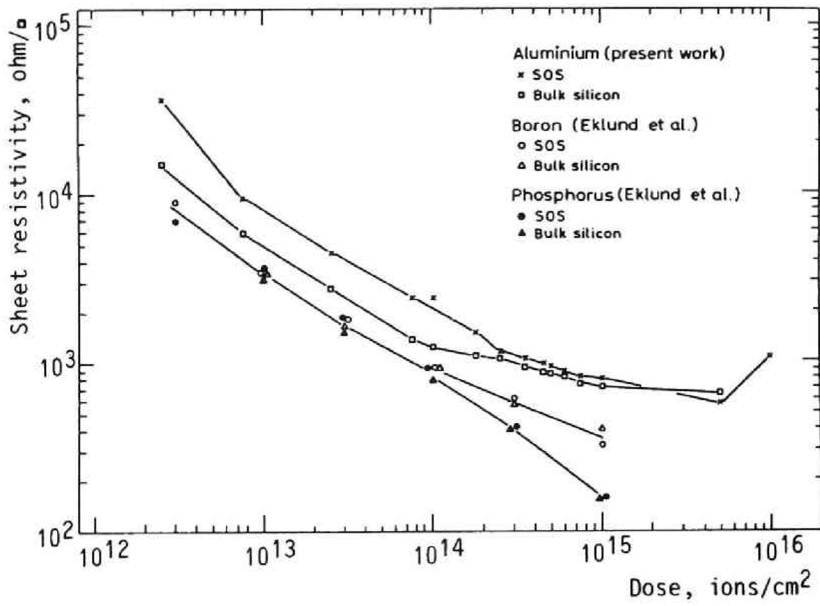


Fig. 3.35
The sheet resistance after annealing at 800°C for different doses of 40-keV Al, B and P ions implanted at room temperature in bulk silicon and silicon on sapphire.[47)]

Figure 3.36 shows the relation between peak Pd concentration and sheet resistance. Threshold Pd concentration to attain low resistance is about 20 at.% and this value corresponds to 33 vol.% of PdSi grains. In order to get resistivity lower than 10 Ω/□, peak Pd concentration must exceeds 30 at.%. This means that volume percentage of metallic material (PdSi) must exceed 52 vol.% to get a low-resistance buried conductive layer by ion implantation. Pd has an advantage of getting higher concentration of metallic material for a given dose due to metallic compound formation with Si.

### 3.4.6 Energy Dependence of Sheet Resistance of the Pd Implanted Si

Figure 3.37 shows the sheet resistance of the Pd implanted Si as a function of ion energy at a fixed dose of $2 \times 10^{17}$ $cm^{-2}$. Energy range in the Fig. 3.37 can be divided into three regions, ie. the region I where energy is less than 100 keV and the resistance is high, the region II where energy is between 100 and 350 keV and resistance is low, and the region III where energy is more than 350 keV and the resistance is high. Fig. 3.38 shows the depth profiles of Pd in the samples measured by Rutherford backscattering. At 50 keV in the region I, total amount of Pd deposited in the sample and the peak Pd concentration in the sample are both small owing to resputtering of the implanted Pd, and, as a result, sheet resistance is high. At 400 keV in the region III, because of large scatter in Pd distribution, the peak Pd concentration is small, and the obtained resistance is high. In the middle-energy region II, a low resistance buried conductive layer is obtained because moderate depth and scatter of Pd distribution avoid the resputtering of the implanted Pd and make it possible to get high concentration of Pd. From these results, it can be concluded that there exists an optimum energy and dose in buried conductive layer formation by ion implantation.

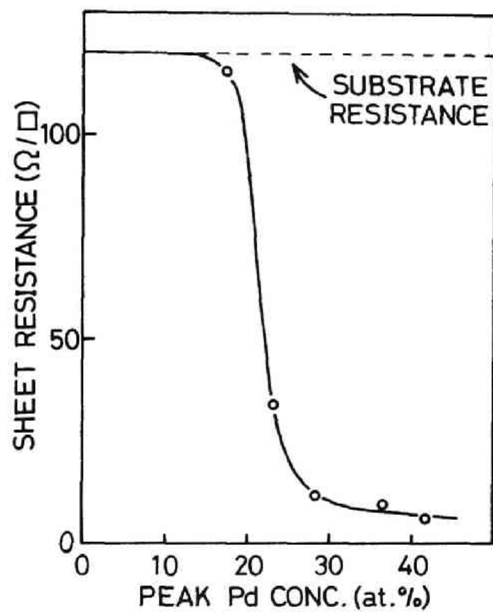


Fig. 3.36
Sheet resistance of 320-keV Pd-implanted Si(100), postannealed at 300°C for 30 min, as a function of peak Pd concentration.

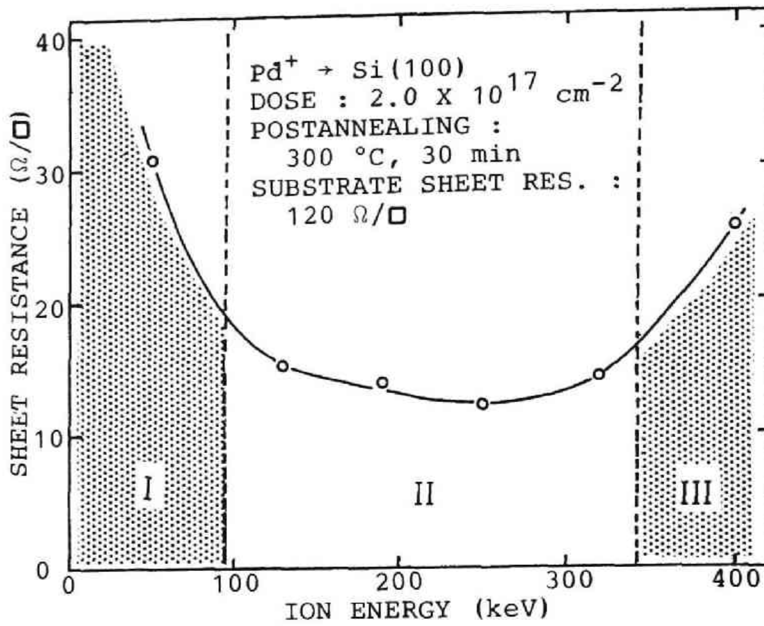


Fig. 3.37
Sheet resistance of Pd implanted Si(100) to a dose level of 2 X $10^{17}$ $cm^{-2}$ at various energies.

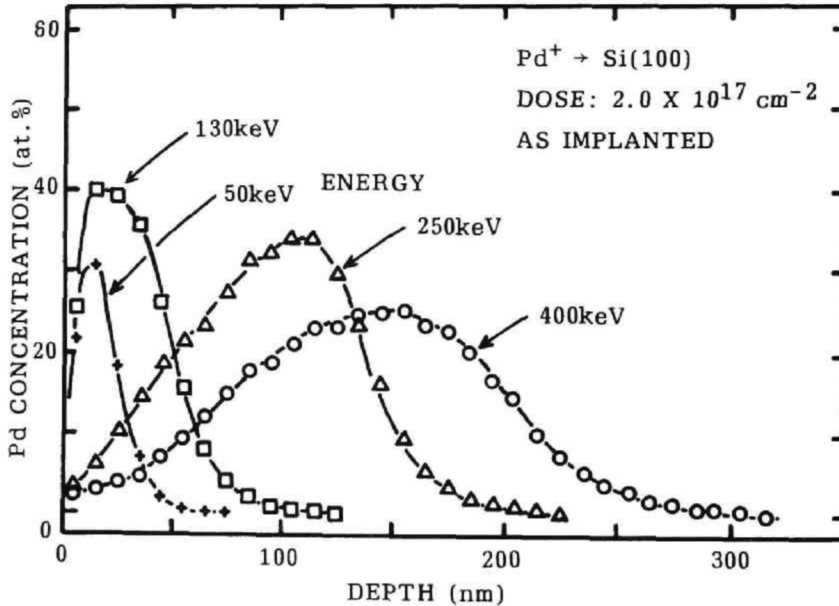


Fig. 3.38
Depth profiles of Pd implanted in Si(100) to a dose level of 2 X $10^{17}$ $cm^{-2}$ at various energies.

### 3.4.7 Recovery of the Crystallinity of Surface Si

Figure 3.39 shows the reflective electron diffraction patterns from the samples implanted with Pd ions to a dose level of 4.0 X $10^{17}$ $cm^{-2}$ and annealed at 600°C for 30 min in vacuum. Only the diffraction spots corresponding to Si can be seen. The recovery of crystallinity is better when Si(111) is used as the substrate, to the extent that the diffraction pattern becomes streaky, showing the flatness of the recovered surface.[48) These results indicates that we can grow another epitaxial layer on the sample with a buried conductive layer. Recovery of the crystallinity of the surface Si is also observed in the samples implanted with Ag or Al, but the degree of recovery is not so great.

## 3.5 Conclusions

Metallization of Si by a mass-analyzed ion beam of low energy ( 10 - 400 eV ) and high energy ( a few tens to a few hundreds of keV) has been described. With low-energy Pd ion beam deposition on Si, the optimum ion energy, in terms of the collection efficiency and the condition of the film-substrate interface, is found to be 50 - 100 eV. Continuous Pd films are obtained with resistivity of the same order as that of the bulk material, yet the films are as thin as a few nanometers in thickness. These films presumably result from the shallow implantation of Pd and the increase in nucleation sites created by ion irradiation. Selective deposition on conductor regions is also found to be possible.

In case of metallization by high-dose ion implantation, Pd, Ag, and Al ions are implanted into Si at energy level of 320 keV, 320 keV, and 73 keV, respectively. Sheet resistance of the samples decreases abruptly when the ion doses exceed 9 X $10^{16}$, 1.8 X $10^{17}$, and 2 X $10^{17}$ $cm^{-2}$, respectively, and reaches about 6 Ω/□,

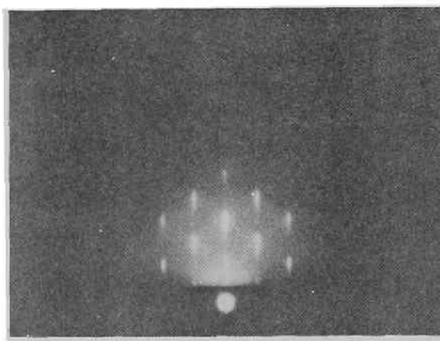

(a) $Pd^+ \rightarrow Si(100)$

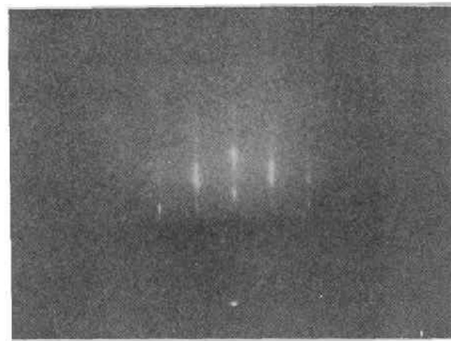

(b) $Pd^+ \rightarrow Si(111)$

Fig. 3.39
RED patterns from Pd-implanted (320 keV, $4.0 \times 10^{17}$ $cm^{-2}$) single-crystal Si, postannealed at 600°C for 30 min.

which is not readily obtained by the conventional doping concept, indicating that a continuous metallic layer is formed. Pd implantation causes a stable PdSi buried layer which endures an 800°C, 30 min anneal. The surface of the Pd implanted sample resumes the crystallinity of Si after a 600 - 800°C, 30 min anneal, which indicates that another epitaxial layer can be grown on this buried metal layer fabricated by ion implantation. Dependence of the sheet resistance on implantation energy is also measured for the Pd implanted sample. The result shows that the presence of the threshold concentration of metallic species to form a continuous layer and the sputter erosion of the surface determine the optimum energy and dose for buried layer formation.

It is concluded that in the formation of very thin films and buried conductive layers, characteristics of an atomic ion beam are effectively utilized to realize what cannot be attained by conventional deposition methods.

Refernces (Chapter 3)


1) A. Fontell and E. Arminen: Ann. Acad. Sci. Fennicae, Ser. A, VI, No.244, pp.4-13, 1967.
2) A. Fontel and E. Arminen: Can. J. Phys. 47 (1969) 2405.
3) B.A. Probyn: Brit. J. Appl. Phys. (J. Phys. D) Ser.2, 4 (1968) 457-465.
4) W.B. Shepherd: Record of the 11th Symp. on Electron, Ion, and Laser Beam Technol., ed., R.F.M. Thornley (San Francisco Press, Inc., 1971) pp.323-330.
5) S. Aisenberg and R. Chabot: J. Appl. Phys. 42 (1971) 2953.
6) E.G. Spencer, P.H. Schmidt, D.C. Joy and F.J. Sansalone: Appl. Phys. Lett. 29 (1976) 118-120.
7) J.H. Freeman, W. Temple, D. Beanland and G.A. Gard: Nucl. Instr. Meth. 135 (1976) 1-11.
8) T. Tsukizoe, T. Nakai and N. Ohmae: J. Appl. Phys. 48 (1977) 4770-4776.
9) R.P.W. Lawson, J.H. Freeman, J.S. Colligon, W.A. Grant, M.J. Nobes and J.S. Williams: Nucl. Instr. Meth. 131 (1975) 567-568.
10) J.S. Colligon, W.A. Grant, J.S. Williams and R.P.W. Lawson: Inst. Phys. Conf. Ser., No.28, pp.357-361, 1976.
11) J. Amano, P. Bryce and R.P.W. Lawson: J. Vac. Sci. Technol. 13 (1976) 591-595.
12) J. Amano and R.P.W. Lawson: J. Vac. Sci Technol. 14 (1977) 690-694.
13) J. Amano and R.P.W. Lawson: J. Vac. Sci. Technol. 14 (1977) 695-698.
14) J. Amano and R.P.W. Lawson: J. Vac. Sci. Technol. 15 (1978) 118-119.
15) K. Yagi, K. Miyake and T. Tokuyama: Inst. Phys. Conf. Ser., No.38, pp.136-141, 1978.

References (Chapter 3)

16) K. Yagi, S. Tamura and T. Tokuyama: Jpn. J. Appl. Phys. 16 (1977) 245-251.

17) K. Miyake, K. Yagi and T. Tokuyama: Inst. Phys. Conf. Ser. No.38, pp.78-83, 1978.

18) G.E. Thomas, L.J. Beckers, J.J. Vrakking and B.R. de Koning: J. Cystal Growth 56 (1982) 557-575.

19) P.C. Zalm and L.J. Beckers: Appl. Phys. Lett. 41 (1982) 167-169.

20) T. Miyazawa, S. Misawa, S. Yoshida and S. Gonda: J. Appl. Phys. 55 (1984) 188-193.

21) S. Gonda, T. Miyazawa, S. Misawa and S. Yoshida: Proc. 8th Symp. on ISIAT'84, Tokyo (1984) pp.201-206.

22) S. Shimizu, O. Tsukakoshi, S. Komiya and Y. Makita: Proc. Int'l Ion Engineering Congress -ISIAT'83 & IPAT'83-, Kyoto (1983) pp.1087-1090.

23) S. Shimizu, O. Tsukakoshi, S. Komiya and Y. Makita: Jpn. J. Appl. Phys. 24 (1985) L115-L118.

24) J.K. Hirvonen (ed.): Ion Implantation, Treatise on Material Science and Technology, Vol.18 (Academic Press, New York, 1980).

25) H.H. Andersen in: Ion Implantation and Beam Processing, eds., J.S. Williams (Academic Press, Sydney, 1984) Chap.6, p.127.

26) S.M. Myers in: Thin Films -Interdiffusion and Reactions, eds., J.M. Poate, K.N. Tu and J.W. Mayer (John Wiley & Sons, New York, 1978) Chap.14, p.533.

27) Z.L. Liau and J.W. Mayer in ref.24, p.17.

28) S. Kirkpatrick: Rev. Mod. Phys. 45(4) (1973) 574.

29) B. Abeles: Applied Solid State Science (Academic Press, New York, 1976) Vol. 6, p.1.

30) C.J. Kircher: Solid-State Elctron. 14 (1971) 507-513.

References (Chapter 3)


31) W.D. Buckley and S.C. Moss: Solid-State Electron. 15 (1972) 1331-1337.

32) R.W. Bower, D. Sigurd and R.E. Scott: Solid-State Electron. 16 (1973) 1461-1471.

33) B.Y. Tsaur. S.S. Lau and J.W. Mayer: Appl. Phys. Lett. 35(3) (1979) 225-227.

34) H. Ishiwara and N. Kuzuta: Appl. Phys. Lett. 37(7) (1980) 641-643.

35) H. Ishiwara, K. Hikosaka and S. Furukawa: Appl. Phys. Lett. 32(1) (1978) 23-24.

36) B. Chapman: Glow Discharge Processes (Wiley, New York, 1980) p.39.

37) P.C. Townsend in: Sputtering by Particle Bombardment II, ed., R. Behrisch (Springer, Berlin, 1983) p.147.

38) K.L. Chopra: Thin Film Phenomena (McGrow-Hill, New York, 1969) p.345.

39) J.A. Roth and C.R. Crowell: J. Vac. Sci. Technol. 15(4) (1978) 1317-1324.

40) M. Hansen: Constitution of Binary Alloys, (McGrow-Hill, New York, 1958).

41) J.F. Gibbons, W.S. Johnson and S.W. Mylroie: Projected Range Statistics, 2nd ed. (Dowden, Hutchinson & Ross Inc., Stroudsburg, 1975).

42) O. Meyer and J.W. Mayer: J. Appl. Phys. 41 (1970) 4166.

43) J. Räisänen: Appl. Phys. A30 (1983) 87.

44) P. Blank, K. Wittmaack and F. Schulz: Nucl. Instr. Meth. 132 (1976) 387-392.

45) O. Almén and G. Bruce: Nucl. Instr. Meth. 11 (1961) 279.

46) O. Almén and G. Bruce: Nucl. Instr. Meth. 11 (1961) 257.

References (Chapter 3)

47) G. Holmén and S. Peterström in: Ion Implantation in Semiconductors 1976, eds., F.Chernow and J.A. Borders (Plenum, New York, 1977) p.11.

48) E.M. Murt and W.G. Guldner: Physical Measurement and Analysis of Thin Films, (Plenum Press, New York, 1969), p.110.

## Chapter 4

## Al METALLIZATION BY IONIZED CLUSTER BEAM

### 4.1 Introduction

Ionized cluster beam (ICB) technique,[20-57] as one of ion-based film formation techniques, permit control over the energy and ion content of the beam, and thus control over sputter cleaning, formation of nucleation sites and adatom migration. Unlike the apparatus for low-energy mass-analyzed ion beam deposition, that of ICB deposition is quite simple and easy to be scaled up. ICB also realizes high deposition rate. These properties make the ICB technique useful in practical applications.

As an application of ICB technique, Al metallization is the most challenging because Al is widely used for contact electrodes and interconnects in Si semiconductor devices[1-3] due to its low electrical resistivity, relative ease in preparation, good etchability, good bondability, good adherence, and low cost. The problems in Al metallization such as alloy penetration, electromigration, recrystallization of Si at the interface, etc. are usually met by the adoption of Al alloys or combinations of Al alloys and other materials such as poly-Si[1] and silicides[3-6] with some success. However, the strategy in this study on Al metallization is to investigate the possibility of pure-Al metallization using ICB technique because problems above depend critically upon film structure (primarily grain size and orientation) and interface properties,[1,7,8] which are not precisely controlled under any conventional Al deposition

techniques but are readily controlled with ICB by varying deposition conditions of acceleration voltage ($V_a$) and electron current for ionization ($I_e$).

From now, brief summary of Al properties and the trouble with Al metallization will be given for understanding of how these problems are to be solved by the ICB technique.

Figure 4.1 shows the Al-Si equilibrium phase diagram.[9] It can be seen that Si has an appreciable solid solubility in Al, which amounts to 0.46 at.% at 450°C, 0.77 at.% at 500°C and 1.25 at.% at 550°C. Whereas, Al has a negligible solubility in Si($<$ 0.02 at.%).[10] In addition, the diffusion coefficient D of Si in Al is quite large as shown in Fig. 4.2.[11] Mean diffusion distance $(Dt)^{1/2}$ in 30 minutes amounts to 50 μm at 450°C, 80 μm at 500°C and 120 μm at 550°C, according to McCaldin and Sankur's data for thin films, whereas the diffusion of Al in Si is negligibly small ( $(Dt)^{1/2} < 1$ Å ).[12] These properties of the Al-Si system bring about the problems of alloy penetration [1,2,7,13] and recrystallization of Si at the Al-Si interface. [12,14-16] Figure 4.3 illustrates the formation of alloy penetration after Poate et al.[7] During annealing, Si from the single-crystal substrate diffuses into the Al film to satisfy the solubility, and Al goes into Si in the reverse direction. Since the dissolution of Si starts where the native oxide of Si has defects, the interface recedes nonuniformly exhibiting a spiked feature.

Silicon, which has been dissolved in the Al to its solubility limit, recrystallizes at the interface when the sample is cooled slowly.[12] If the Al has been intentionally doped with Si beforehand, the excess Si recrystallizes during annealing.[14-16] This recrystallized Si is heavily doped with Al (ie. $P^+$-type) and causes troubles such as the increase of contact resistance of an Al-$n^+$-Si ohmic contact and the shift of barrier height of an Al-Si Schottky diode.

It should be pointed out here that the diffusion coefficients

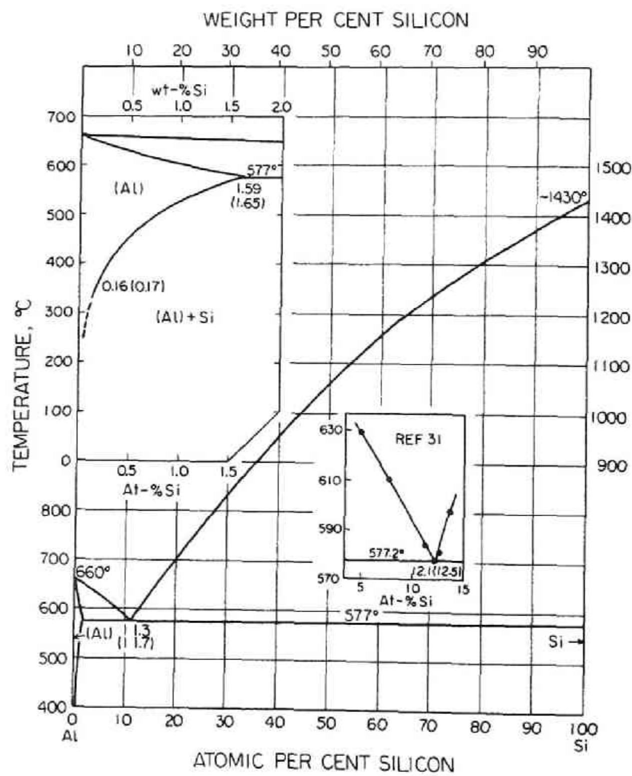


Fig. 4.1
Al-Si phase diagram.[9)]

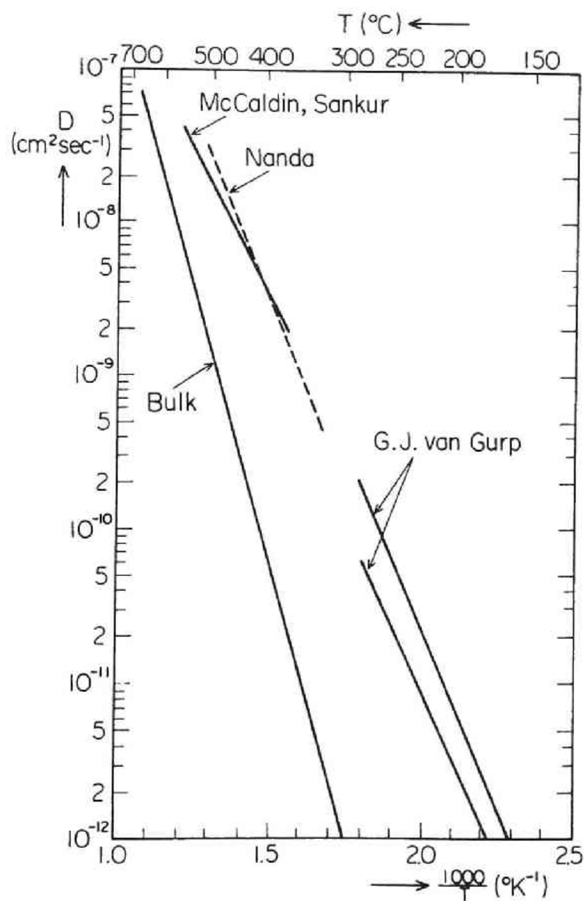


Fig. 4.2
Diffusion coefficients for Si in Al for bulk Al sample and thin film samples.[11]

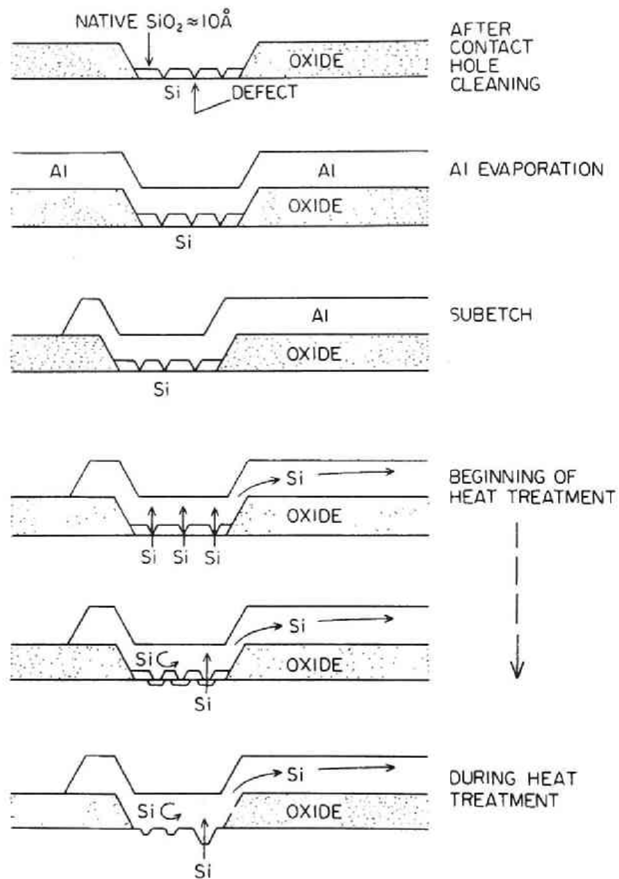


Fig. 4.3
Formation of alloy penetration pits.[7)]

of Si for Al thin films are much larger than that for bulk samples as is shown in Fig. 4.2. For example, the former is 10 times larger at 550°C, 20 times larger at 500°C and 30 times larger at 450°C. Since the rapid diffusion in the thin film samples is mainly due to the grain boundary diffusion, which greatly depends on the film structure (primarily grain size and orientation),[7] the problems above can be expected to be solved by improving the film structure by ICB technique.

Electromigration is a phenomenon in which metal atoms are transported under high current conditions and voids and hillocks are formed in the film.[1,2] Al metallization tends to suffer from the electromigration problem, because of the large grain boundary self-diffusion in Al. Again, electromigration is very sensitive to film structure. Vaidya and Sinha reported that[8]

(1) An increase in the degree of <111> orientation of Al film increases the electromigation lifetime.

(2) The lifetime increases as the median grain size s increases and decreases as the variance $\sigma^2$ of the grain size increases.

(3) The experimental lifetime data are fitted well to a structure variable $(s/\sigma^2)\log(I_{111}/I_{200})^3$, where $I_{111}$ and $I_{200}$ are the X-ray diffraction intensity of {111} and {200} peaks, respectively.

Figure 4.4 reproduces their data. It is apparent that improvements in film structure by ICB technique are sure to increase the electromigration lifetime.

Annealing hillocks, which are the small protuberances on the film surface induced by the thermal expansion mismatch stress,[1,2,17,18] can cause such problems as discontinuous interconnects and shorting through the insulation. This phenomenon is also related to the self-diffusion rate of Al as well as to grain boundary diffusion. Thus improvements of film structure leading to decrease in diffusion rate are again expected to solve the

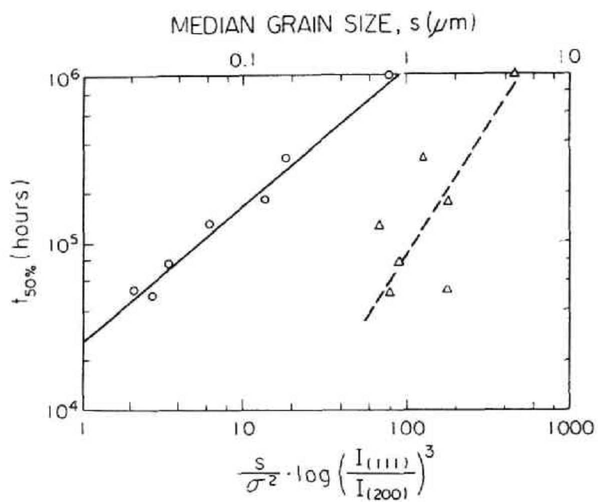


Fig. 4.4
Correlation of electromigation lifetime for Al films with the median grain size (Δ) and with the micro-structural parameter (o).[8)]

problems.[19]

It has been shown that the problems characteristic to Al metallization of Si devices, such as alloy penetration, recrystallization of Si at the interface, electromigration and annealing hillocks are all related to and sensitive to the film structure and the interface properties, which are not readily controlled by any conventional deposition method but are controllable in the ICB technique. In this chapter, fundamentals of the ICB technique are described first in Section 4.2. Then Al film deposition and epitaxy by ICB are discussed in terms of application of such film deposition to semiconductor metallization. Crystalline orientation, grain size, contact resistivity, Al-Si interface stability, annealing hillocks, oxidation resistance, step coverage, optical reflectance, etc. are evaluated. In Section 4.3, Al deposition in a moderately high vacuum ($2 \times 10^{-4}$ Pa) is described, and in Section 4.4, Al epitaxial growth on a clean Si surface[87] in an ultra-high vacuum ($2 \times 10^{-7}$ Pa) is described to show the ultimate form of Al metallization by ICB. Lastly, Al epitaxy on insulator substrates, such as sapphire and epitaxially grown $CaF_2$, are presented to realize epitaxial Al films on any level of metallization.

## 4.2 Fundamentals of ICB Technique

### 4.2.1 Characteristics of the ICB Technique

The ICB technique,[20-57] which was devised by Prof. Toshinori Takagi at Kyoto University in 1972 and has been developed by him and other workers, is one of the ion beam deposition methods where macroaggregates of atoms (clusters) formed from deposit material vapor are utilized instead of atomic or molecular state particles. Figure 4.5 shows a typical ICB source. The vaporized-metal clusters are formed in a supersaturation state caused by

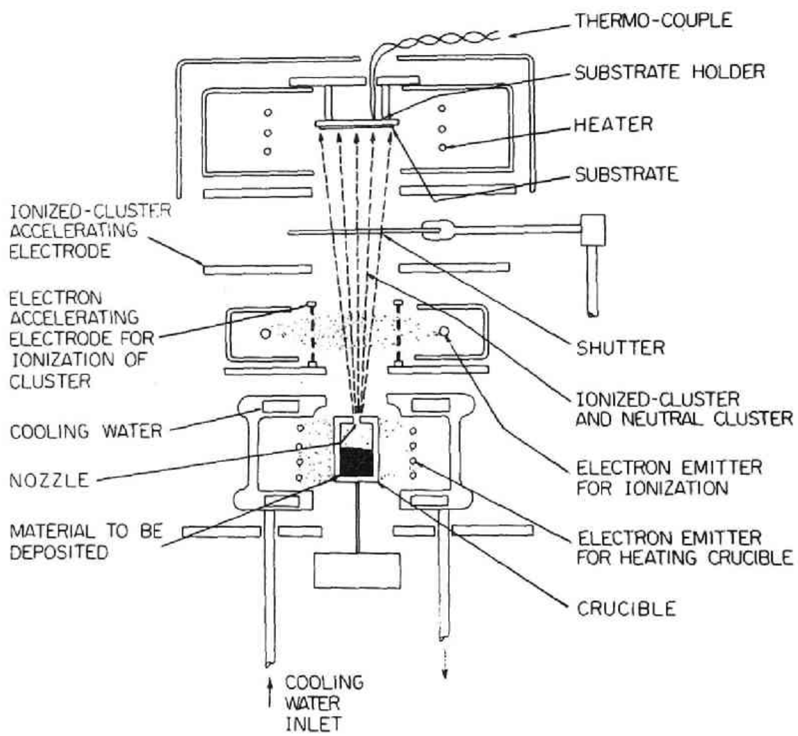


Fig. 4.5
Schematic diagram of a typical ICB source.

isentropic expansion of high-pressure vapor in a heated crucible through a small (< 2 mm) nozzle leading to a high-vacuum (< $10^{-2}$ Pa) region. Each cluster contains 500-2000 atoms loosely coupled together, which is different from the droplet (liquid particle) in that the droplet contains from 5 X $10^8$ to 5 X $10^9$ closely coupled atoms per droplet. The clusters are ionized to be singly charged by electron bombardment in the ionization electrode assembly located above the crucible. The cluster ions are accelerated towards the substrate by a high negative potential applied to the accelerating electrode. Besides the ionized clusters, there are neutral clusters which remain unionized during flow in the ionization region. Although the neutral clusters are not accelerated by the voltage, they move towards the substrate at ejection velocity. Compared with other atomic- or molecular-ion-based techniques such as sputter deposition, ion plating, etc. the ICB technique has a lot of attractive characteristics as summarized in Table 4.1.

When the clusters are broken up into the atomic state again on their arrival at the substrate, the incident momentum of the clusters is effectively transformed into the surface diffusion energy of each atom.[23-25] The migration effect of adatoms due to this enhanced surface diffusion energy contributes to forming good quality films or to adjusting the morphology of deposited films.

Effects of energy and charges of ions described as ion-surface interactions in Chap. 2 are also obvious. Low temperature epitaxy of Si,[26-29] GaAs,[30,31] GaP,[32] ZnS,[33] ZnO[34] and BeO[35,36] has been achieved by ICB technique. Improvements in crystallographic, electrical and optical properties are observed in Au, Cu,[29,37] Pb,[38] Ag,[28,39,40] PbTe,[41] ZnSb,[42] $FeSi_2$,[43] CdTe,[44] $FeO_x$,[45] GaN[46] and SiC[47] deposition. Even the crystalline structure of organic materials, such as anthracene[48] and Cu-phthalocyanine[49] were found to be controllable in ICB deposition. Increase of adhesion strength of

Table 4.1 Characteristics of ICB Technique

1. Formation of high-quality films
   1.1 Enhanced surface diffusion (Migration effect)
   2.1 Effects of energy and charges of ions (see Chap. 2)
      . Lowering of processing temperature
      . Improvement of crystallographical, electrical and optical properties
      . Increase of adhesion strength of deposited films
      . Change in morphology
      . Densification of deposited films
      . Formation of metastable materials

2. Advantages due to small charge-to-mass ratio
   2.1 Efficient low-energy high-intensity ion beam transport
   2.2 Small charge-up problem in depositing on an insulator substrate
   2.3 Small radiation damage

3. High-vacuum operation
   3.1 Small amount of contamination
   3.2 Small memory effect by preveously used materials or gases

4. Applicability to reactive deposition

5. High deposition rate

6. Relative ease in scaling up the deposition apparatus

Au, Cu,[29,37] Pb,[38] $SnO_2$[50] and PbO[38] film by ICB has been reported. Drastic improvement of surface flatness as the acceleration voltage ($V_a$) of ionized clusters was increased was observed in Pb deposition.[51] Disappearance of columnar structure in $MgF_2$ films was found in ICB deposition.[52] Improvement in packing density of Cu[29,37] films was achieved by ICB. Thermally stable hydrogenated amorphous Si was also deposited successfully.[53,54]

It seems that the above-mentioned improvements in film quality attained by ICB deposition are not restricted to specific materials but are generally observed in a wide range of materials.

As was described in Chap. 3, it is very difficult to transport high-current and low-energy ion beams because of space charge repulsion. This problem is greatly relieved by the use of ICB as ionized clusters possess a small charge-to-mass ratio. Let us consider the space-charge-limited current $J_s$ between infinite-size parallel plates. For a singly charged atomic ion with mass m, $J_s$ is given by

$$J_s = \frac{4\varepsilon_0}{9}\sqrt{\frac{2e}{m}}\,\frac{V^{3/2}}{d^2} \tag{4.1}$$

where V is the voltage difference between two plates and d is the distance between the plates. Mass flux $\Phi_1$ transported by the current of atomic ions is given by

$$\Phi_1 = \frac{J_s}{e}m = \frac{4\varepsilon_0}{9}\sqrt{\frac{2m}{e}}\,\frac{V^{3/2}}{d^2} \tag{4.2}$$

In the case of a singly charged ionized cluster whose size (number of atoms per cluster) is N, mass flux $\Phi_N$ is obtained by changing m to Nm and V to NV in eq. (4.2). The latter change is done to keep energy per atom unchanged. $\Phi_N$ is then

$$\Phi_N = \frac{4\varepsilon_0}{9}\sqrt{\frac{2Nm}{e}}\,\frac{(NV)^{3/2}}{d^2} = N^2\Phi_1 \tag{4.3}$$

As can be seen from eq. (4.3), using an ionized cluster of size N, $N^2$ times larger mass flux can be transported compared to the case with atomic ions.

The small charge-to-mass ratio of ionized clusters is also useful in deposition onto insulator substrates, because the ion current of ICB is much smaller than that of an atomic ion beam at the same deposition rate and the degree of charging up of the substrate is expected to be small.

Less radiation damage by ICB bombardment than by atomic ion bombardment at the same energy can also be attributed to the small charge-to-mass ratio. Even if the acceleration voltage ($V_a$) is 10 keV, average energy per atom is only about 10 eV, which is not enough to cause severe damage on the substrate or the growing film. The amounts of radiation damage by ICB and atomic ion beam bombardment were experimentally compared using ion backscattering / channeling.[31,55] The ICB Al films on Si(111) substrates were chemically removed after deposition and the surface of the single-crystal substrate was revealed. As standard samples for comparison, $Ar^+$ bombarded Si substrates were prepared. The $Ar^+$ bombardment was made at 0.5 keV to dose of $2 \times 10^{15}$ $cm^{-2}$. 0.5-keV $Ar^+$ beam, 5-keV ICB and 0.2-keV ICB caused $2.4 \times 10^{16}$, $1.3 \times 10^{16}$ and $0.8 \times 10^{16}$ displaced Si/$cm^2$, respectively, while the surface peak of nonirradiated Si(111) was $6.9 \times 10^{15}$ Si/$cm^2$. Thus, it was concluded that the disorder induced by ICB is significantly smaller than the disorder produced by atomic ion bombardment.

As is understood from the cluster formation mechanism and the ionization method, ICB apparatus operates in a high vacuum (< $10^{-2}$ Pa). In contrast to sputter deposition or ion plating, the ICB technique does not utilize plasma discharge and this feature realizes deposition with less contamination. ICB apparatus can also operate in an ultra-high vacuum without any difficulty.

Due to operation in a high vacuum, the ICB technique is less bothered by a memory of previously used material or gases. For

example, in fabrication of an amorphous Si p-i-n junction for a solar cell by conventional glow discharge method, three different vacuum chambers corresponding to each p-, i- and n-layer must be used to get a sharp profile of dopant distribution because a large amount of dopant gas is adsorbed on a wall and reemitted when the wall is exposed to plasma in the next step. In ICB deposition one vacuum chamber is enough because of a small amount of adsorbed gases and absence of plasma discharge due to high-vacuum operation.

Reactive deposition is also realized using the ICB technique (R-ICB). A reactive gas, e.g. oxygen, nitrogen, etc. is supplied from a gas nozzle near the metal vapor ejection area through a controlled leak valve to maintain the desired pressure in the chamber during the deposition. As the pressure during deposition is maintained at less than $10^{-2}$ Pa and the corresponding mean free path of the gas molecules is longer than the distance between the nozzle and the substrate, chemical reaction takes place mainly on the film surface. Although the pressure of the reactive gas during the deposition is lower than that of conventional reactive deposition methods, chemical reaction occurs efficiently owing to the enhanced ion-surface-interaction by ICB. Oxides such as ZnO,[34)] BeO,[35,36)] PbO,[38)] $SnO_2$,[50)] $SiO_2$[56)] and $FeO_x$,[45)] nitrides such as GaN,[46)] carbides such as SiC[47)] and hydrides such as a-Si:H[53,54)] have been successfully deposited by R-ICB at low ambient pressure.

High deposition rate achieved by ICB technique originates from the use of a nozzle beam, in which the mean free path of the vapor atoms is substantially greater than the nozzle diameter. The characteristics of a nozzle beam are also important in cluster formation and are discussed more intensively later.

ICB apparatus can be scaled up with less difficulty compared with other deposition apparatus utilizing discharge plasma, which is very hard to be generated uniformly. Figures 13 and 14 in

ref. 57 shows the structure of a commercial ICB source to deposit Cu on a large area. That source utilizes multiple nozzles which form a "curtain" beam fitted to roll-to-roll processing.

The characteristics above make the ICB technique useful in semiconductor metallization. ICB can efficiently realize low-energy high-intensity ion beam transport and can fully utilize the advantages of ion-based film formation without causing severe radiation damage or contamination problems. High deposition rate and relative ease in scaling up are important factors in using the ICB technique on an industrial basis.

### 4.2.2 Operating Conditions of ICB Source

In order to determine the operational conditions of an ICB source, properties of the nozzle source and the nucleation of clusters must be understood.

In ICB deposition, a nozzle source is adopted to cause isentropic expansion and to cool down a metal vapor into clusters.[74] The nozzle source (ie. cluster source) is operated under the condition that the nozzle diameter D is much larger than the mean free path $\lambda$ of the vapor atoms ($D >> \lambda$). This means that the atoms collide with each other in the nozzle and behave on the whole as a fluid. This collective action of the vapor atoms realizes the vonversion of thermal energy to kinetic energy of the flow through the collisions between atoms, that is, the temperature T of the vapor decreases and the mass flow velocity (translational velocity) U increases during the expansion. The counterpart of a nozzle source is an effusive source, in which orifice diameter is much smaller than the mean free path ($D << \lambda$). In this case, collision between atoms does not occur, the temperature T of the vapor does not change, and consequently clusters are not formed. A so-called "Knudsen cell", which is used in molecular beam epitaxy and sometimes looks similar to what is used in the ICB deposition in shape, is really an effusive

source.

For an effusive source, the velocity distribusion of vapor atoms in translational direction is given by

$$n_{u,c}(\text{effusive}) = \frac{1}{2}\left(\frac{m}{kT_0}\right)^2 u^3 \, exp\left[-\frac{mu^2}{2kT_0}\right] \Delta u \qquad (4.4)$$

u: velocity of atoms

$T_O$: source temperature

Total intensity at the collimator is given by

$$n_c(\text{effusive}) = \frac{S}{\pi l^2} \qquad (4.5)$$

l: the distance between the orifice and the collimator

s: the area of the small hole on the collimator

For a nozzle source, assuming that the vapor ejected from the source flows continuously to the skimmer, the velocity distribution is given by

$$n_{u,c}(\text{nozzle}) = \left(\frac{m}{2\pi kT_1}\right)^{1/2} exp\left[-\frac{m(u-U)^2}{2kT_1}\right] \Delta u \qquad (4.6)$$

U: the translational velocity

$T_1$: the translational temperature at the skimmer

The total intensity is given by

$$n_c(\text{nozzle}) = \frac{mU^2 S}{2\pi kT_1 l^2} \qquad (4.7)$$

The decrease in the translational temperature and the increase in the translational velocity is expressed by thermodynamics and hydrodynamics. Providing that the gas (metal vapor) is ideal and has the constant specific heat ratio $\gamma$, and does not have friction

or viscosity, $T_1$, U and $n_c$(nozzle) are given by[58)]

$$T_1 = T_0 \left( 1 + \frac{\gamma - 1}{2} M_1^2 \right)^{-1} \qquad (4.8)$$

$$U^2 = M_1^2 \gamma \frac{kT_0}{m} \left( 1 + \frac{\gamma - 1}{2} M_1^2 \right)^{-1} \qquad (4.9)$$

$$n_c\,(\text{nozzle}) = \frac{1}{2} \gamma M_1^2 \frac{S}{\pi l^2} \qquad (4.10)$$

$M_1$: the Mach number of the vapor flow at the skimmer

Using these equations, the calculated velocity distributions at the collimator for both sources are shown in Fig. 4.6. The relation between $T_1$ and $M_1$, and that between U and $M_1$ for the nozzle source are shown in Fig. 4.7. When high $M_1$ is attained, the vapor ejected from the nozzle source has the following characteristics in comparison with those from the effusive source;

(a) much lower temperature,

(b) much more monochromatic velocity distribution,

(c) much larger beam intensity.

It can be understood that the high deposition rate attained by ICB originates from the characteristic (c) of a nozzle beam.

The decrease in the translational temperature and the increase in the translational velocity were experimentally verified with a time-of-flight spectrometer using Ag as a source material.[31)] In Figure 4.8, dependence of the translational velocity on the crucible temperature is shown. The translational velocity increases with increasing crucible temperature. When a larger diameter nozzle was used, higher velocity can be obtained at a lower crucible temperature and the velocity of the cluster beam reaches Mach number M=6. Figure 4.9 shows the beam's translational temperature as a function of the crucible temperature for the cluster source. The translational temperature of the cluster source beam decreases with increasing crucible temperature and the

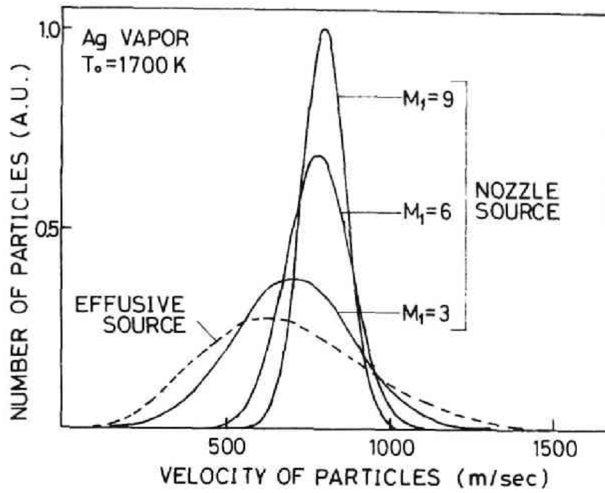


Fig. 4.6
Velocity distributions at the collimator for the nozzle source and the effusive source.

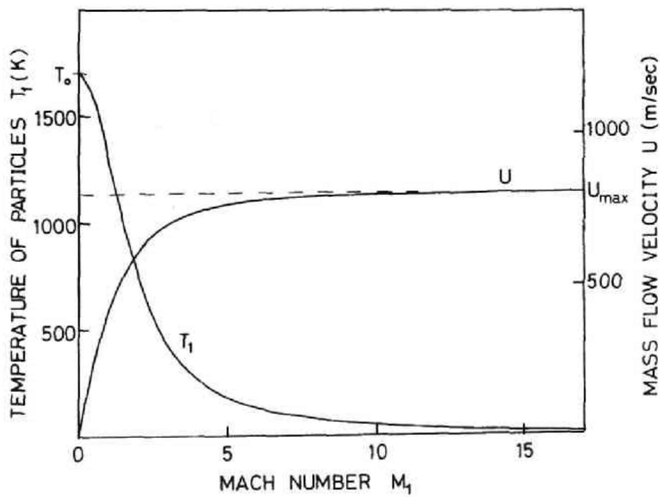


Fig. 4.7
Relation between $T_1$ and $M_1$ and that between U and $M_1$.

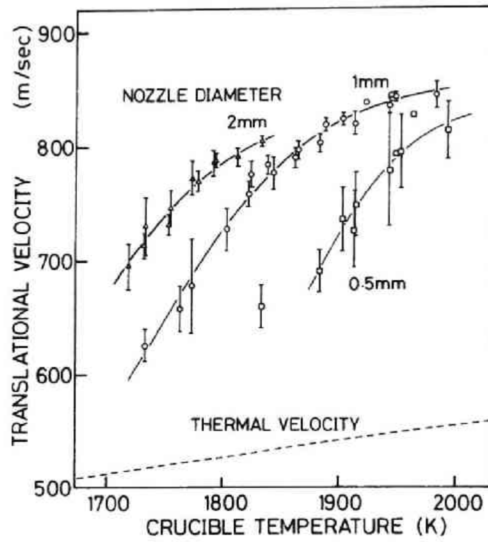


Fig. 4.8
Translational velocity for Ag cluster beam as a function of crucible temperature.[31)]

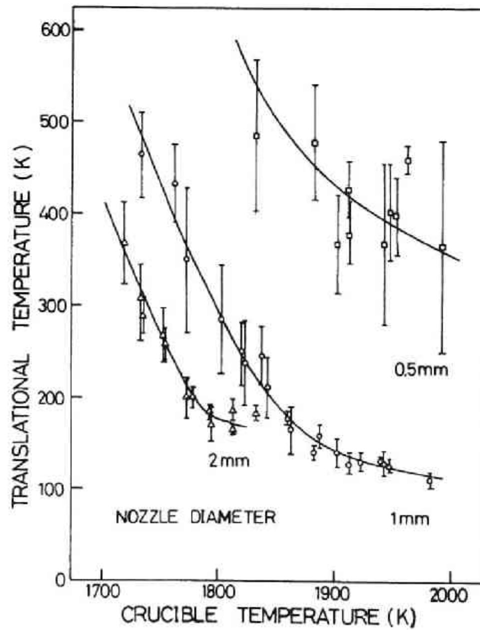


Fig. 4.9
Translational Temperature for Ag cluster beam as a function of crucible temperature.[31)]

Ag vapor becomes supersaturated.

However, cooling of a metal vapor into a supersaturation state is not enough to form clusters because there exists an energy barrier for a vapor to nucleate. Classical nucleation theory gives the nucleation rate J in a supersaturated vapor as follows.[59]

$$J = (\frac{P}{kT})^2 V_c \frac{2\sigma}{\pi m} exp\,[-\frac{4\pi\sigma(r^*)^2}{3kT}] \tag{4.11}$$

P: pressure of the beam

k: Boltzmann's constant,

$v_C$: the atomic volume in the cluster,

$\sigma$: the surface tension of the cluster,

m: atomic mass,

r*: the critical radius given as

$$r^* = \frac{2V_c\sigma}{kT\,ln\frac{P}{P_\infty}} \tag{4.12}$$

$P_\infty$: the saturated vapor pressure.

The cluster whose radius is greater than r* grows capturing the monomer upon collision. Because eqs. (4.11) and (4.12) indicate that the nucleation rate J of clusters rapidly decreases as the surface tension $\sigma$ of the cluster increases, it has been considered that metals, whose surface tensions are generally much higher than those of water and liquified gases, are reluctant to condense from a vapor phase.[60] However, recent experimental results and theoretical calculations have shown that such a simple picture is misleading.[57] Figure 4.10 shows the nucleation rate J of Al (Fig. 4.10 (a)) and Ar (Fig. 4.10 (b)) clusters in P-T diagrams, calculated by classical nucleation theory. In this calculation, dependence of the surface tension $\sigma$ on cluster radius and temperature, and dependence of the atomic volume on temperature are considered.[61-63] The dotted lines in the figure show the

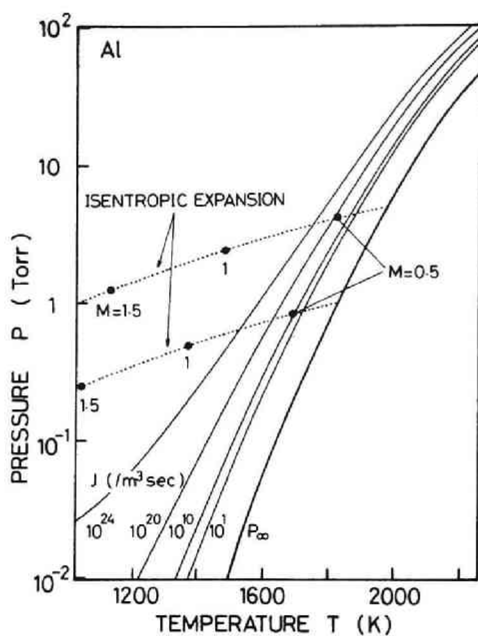


(a) Al clusters

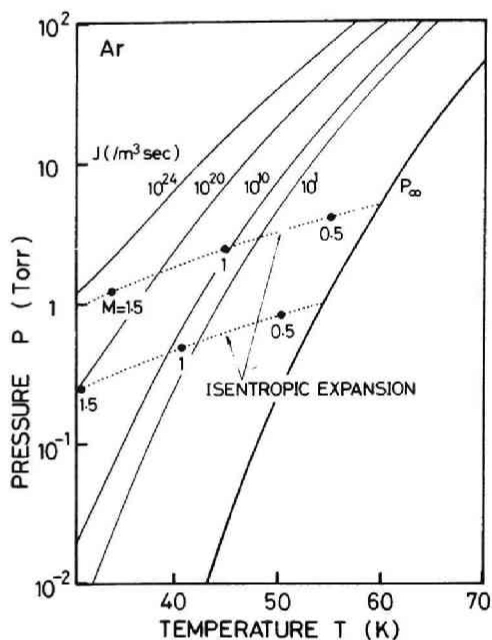


(b) Ar clusters

Fig. 4.10

Nucleation rate J of Al (a) and Ar (b) clusters in P-T diagrams. The dotted lines in the figures show the transition of vapor state along isentropic expansion starting from the saturated vapor in the crucible of 1 and 5 Torr. Mach number M is also shown on the lines.

transition from the vapor state along isentropic expansion starting from the saturated vapor in the crucible of 1 and 5 Torr. Considering that nucleation rate of $10^{24}$ $m^{-3}sec^{-1}$ can be a criterion for cluster formation,[60] nucleation in the Al vapor take place near the point of Mach number M = 0.76 for the source pressure of 1 Torr, and M = 0.62 for 5 Torr. Since the Mach number easily exceeds 3 in supersonic expansion, a sufficient number of clusters is formed in the Al vapor. Comparison with Fig. 4.10 (b) shows that the Al vapor condenses more easily than Ar. This result reflects the fact that because the nucleation rate J is expressed as a function of $\sigma/kT$, the high value of $\sigma$ does not necessarily reduce the nucleation rate if the temperature T of the vapor is high.

Experimental verification of cluster formation has been made with mass analysis (a time-of-flight method),[37] energy analysis (a retarding field method and an electrostatic method) combined with velocity measurements,[38,44] direct observation by transmission electron microscope (TEM),[64] and electron diffraction.[65] These data consistently demonstrated that clusters consisting of 500 - 2000 atoms are really formed by the nozzle source used in the ICB technique.

Theoretical considerations and experimental facts above determine the conditions of cluster source construction and operation. These are summarized in Fig. 4.11 and Table 4.2.

As is mentioned earlier the clusters are ionized by electron bombardment. Concerning the ionization of clusters, an important parameter is the ionization cross section of clusters. It can be expected that the ionization potential of a cluster decreases from that of an atom to a work function of bulk material as cluster size (the number of atoms per cluster) increases. Figure 4.12 shows the ionization potential (I.P.) of Fe cluster as a function of its size.[66] As cluster size increases, the ionization potential of the cluster decreases rapidly at first and then

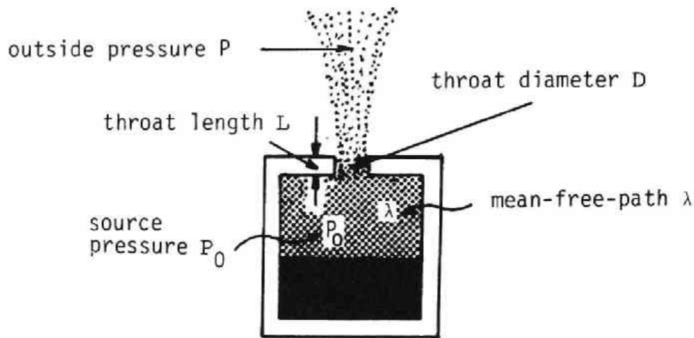


Fig. 4.11
Dimensions and parameters for the design of the cluster source.

Table 4.2 Dimension and parameter for the design of the cluster source compared with those for a molecular beam source.

| Molecular beam | Cluster beam |
|---|---|
| Nonsupersaturated vapour (Molecular flow) | Supersaturated vapour in an adiavatic expansion (viscous flow) |
| $D < \lambda$ | $D \gg \lambda$ (for example; D: 0.1 - 2 mm) |
| $\frac{P_0}{P} < 10^4 - 10^5$ (for example; P: $10^{-3}$ - $10^{-2}$ Torr) | $\frac{P_0}{P} >$ about $10^4 - 10^5$ (for example; P : $10^{-7}$-$10^{-5}$Torr, $P_0$ : $10^{-2}$-several Torr) |
| $\frac{L}{D}$ : not strong districted, tunnel type nozzle also available ( $L \gg D$ ) | $\frac{L}{D} \leq 1$ (in a case of cylindrical nozzle, experimentally $\frac{L}{D} = 1$) |

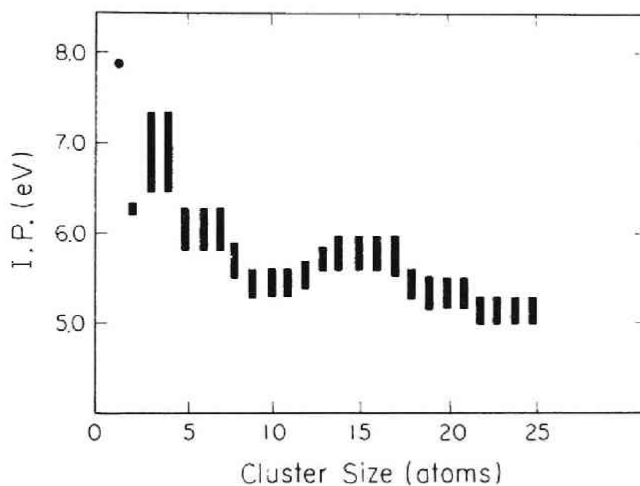


Fig. 4.12

Ionization potential (I.P.) of $Fe_x$ clusters are plotted as a function of cluster size. The solid circle is the I.P. for the iron atom. The work function of iron is 4.8 eV.[66)]

gradually. Theoretical and experimental studies[67] of the ionization cross section of the hydrogen cluster have shown that the cross section is proportional to the cluster size up to a size of 50. For larger clusters, only the surface atoms can be ionized and the cross section is proportional to the 3/2 power of the cluster size. The facts above indicate that clusters are ionized more efficiently than atoms. Figure 4.13 shows an example of the ratio of ionized clusters in the beam as a function of ionization electron current.[68] The electron current for ionization of 0 - 500 mA is found to give the ionization ratio of 0 - 50 % provided that as the dimension of the ionizer is a few cm.

## 4.3 Al Deposition in High Vacuum

### 4.3.1 Experimental Conditions

An ICB source used to deposit Al in a moderately high vacuum (2 X $10^{-4}$ Pa) is shown schematically in Fig. 4.14. This source is a typical one except that the radiation shields are set to avoid temperature rise of the substrate. Al films were deposited in a vacuum chamber evacuated by an oil diffusion pump with a freon-cooled trap. Substrates were p-type 10-Ωcm Si(100) wafers for contact resistivity measurements, polyvinylformal membranes for transmission electron micrograph (TEM) observation, and oxidized Si wafers for the other measurements. Deposition conditions are summarized in Table 4.3.

### 4.3.2 The Al-Si Contact Characteristics

The contact between the Al film and Si substrate was evaluated. Films were deposited at different acceleration voltages over a range from 0 to several kV, followed by annealing at 200°C and 450°C in vacuum for 30 min. The I-V characteristics of the contact were measured and the contact resistivity was calculated. The films deposited by ICB showed linear I-V characteristics after

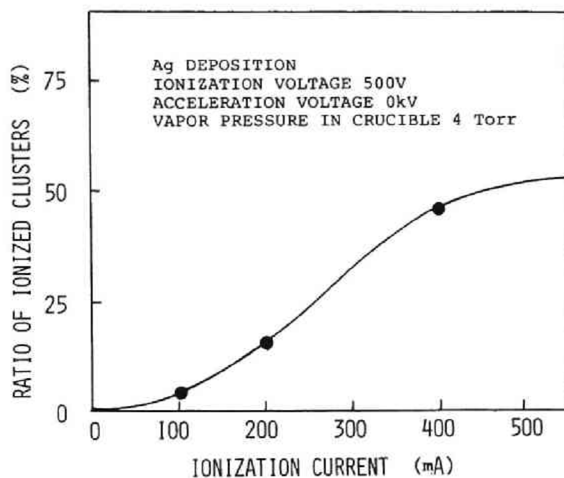


Fig. 4.13

Ratio of ionized clusters in the beam as a function of ionization electron current. Ionization voltage, 500 V; acceleration voltage, 0 kV; vapor pressure in crucible, 4 Torr.[68)]

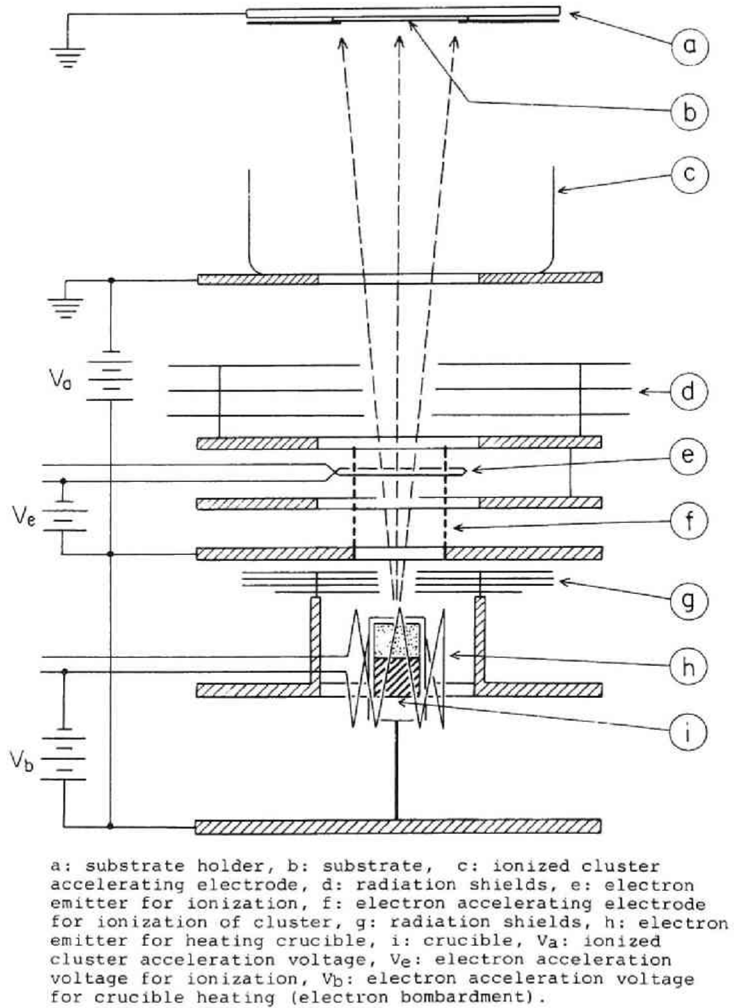


a: substrate holder, b: substrate, c: ionized cluster accelerating electrode, d: radiation shields, e: electron emitter for ionization, f: electron accelerating electrode for ionization of cluster, g: radiation shields, h: electron emitter for heating crucible, i: crucible, $V_a$: ionized cluster acceleration voltage, $V_e$: electron acceleration voltage for ionization, $V_b$: electron acceleration voltage for crucible heating (electron bombardment).

Fig. 4.14
Schematic diagram of the ICB source used to deposit Al films in a normal high vacuum.

Table 4.3 Deposition conditions of Al films by ICB in a moderately high vacuum.

| | |
|---|---|
| Acceleration voltage | 0.0 - 8.0 kV |
| Electron current for ionization | 100 mA |
| Ionization voltage | 500 V |
| Substrate temperature | 50 - 90 °C |
| Deposition rate | 50 nm/min |
| Film thickness | 0.5 - 1.0 μm |
| Background pressure | 2 X $10^{-4}$ Pa |

annealing at 200°C and 450°C, whereas the film deposited by conventional vacuum deposition showed a linear I-V characteristic only after 450°C annealing. Figure 4.15 shows the relationship between the annealing temperature and the contact resistivity measured by TLM method.[69] With ICB deposited films, contact resistivity falls to a low enough value after 200°C annealing and does not vary beyond 200°C. In the case of a film by conventional vacuum deposition, 200°C annealing was not enough to attain low resistivity contacts, so annealing at higher temperatures was necessary.

It seems that the mechanisms of the formation of such low-resistivity contacts by ICB are due to the elimination of the oxide and other contamination on the substrate surface by the cleaning effects of energetic ions.

### 4.3.3 Crystallographical Structure and Electromigration Resistance

As is mentioned earlier, Vaidya and Shinha[8] have reported the following relationship between electromigration lifetime and film microstructure ; (1) the electromigration resistance is found to increase with increasing grain size s and degree of <111> preferred orientation and with decreasing spread $\sigma$ in the grain size distribution, (2) this dependence on microstructure can be expressed in terms of the empirical quantity $(s/\sigma^2)\log(I_{111}/I_{200})^3$ being fitted well to the electromigration lifetime. X-ray diffractometer traces show that the Al films formed by ICB deposition are polycrystalline with <111> preferred orientation. However, the degree of orientation and the shape of the diffraction line change with changing deposition conditions. Figure 4.16 shows the dependence of the ratio of {111} diffraction intensity $I_{111}$ and {200} diffraction intensity $I_{200}$ on acceleration voltage. As the acceleration voltage increases, $I_{111}/I_{200}$ increases accordingly.

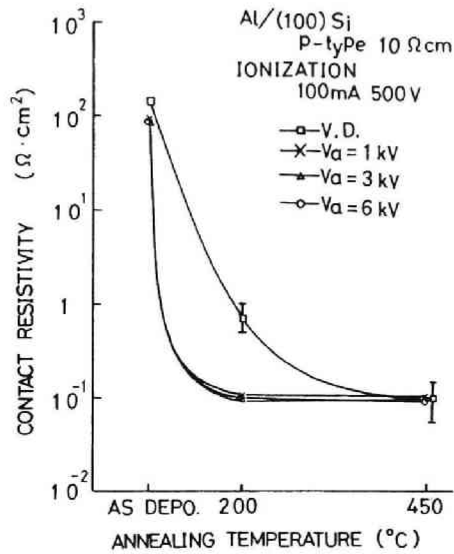


Fig. 4.15
Contact resistivity of ICB Al films to p-type 10-Ωcm Si(100) substrate, as a function of annealing temperature. The data by conventional vacuum deposition (denoted as V.D.) are compared.

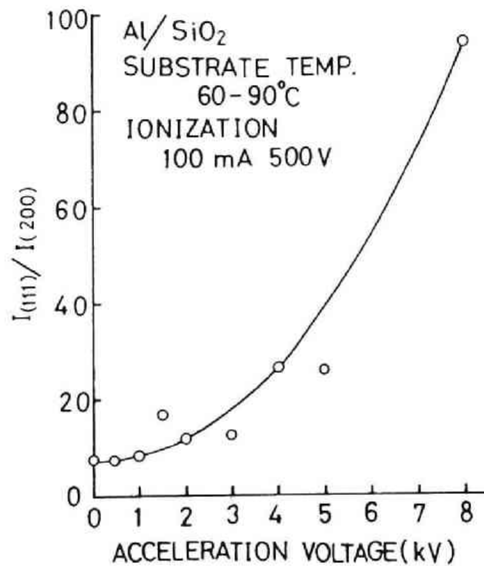


Fig. 4.16
Ratio of X-ray {111} diffraction intensity $I_{111}$ and {200} diffraction intensity $I_{200}$ as a function of acceleration voltage ($V_a$).

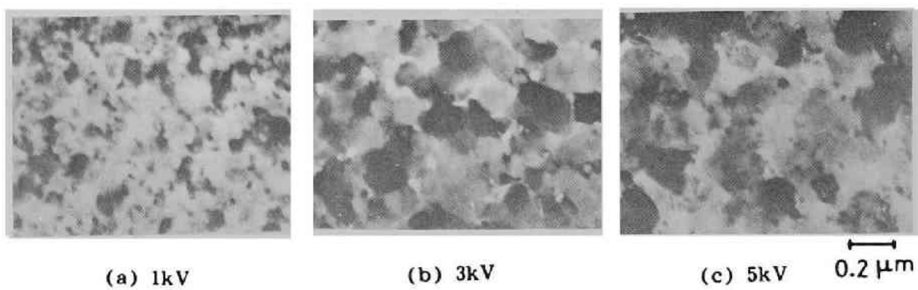


Fig. 4.17
Transmission electron micrographs of ICB Al films deposited at various acceleration voltages ($V_a$). (a) 1 kV, (b) 3 kV, and (c) 5 kV.

Figure 4.17 shows the TEM of the grain structure of the Al films deposited on plastic film substrates. The grain size s is increased monotonically by increasing the acceleration voltage. The spread $\sigma$ in the grain size distribution is decreased slightly. The above-mentioned dependence of the film characteristics on the acceleration voltage shows that the films deposited by ICB promise to have long electromigration lifetime.

### 4.3.4 Oxidation Resistance

The results of Auger profiling analysis of the Al films which were left in air after deposition by ICB were examined. Figure 4.18 shows the depth profiles of oxygen and aluminum near the film surface. The Al film deposited at the high acceleration voltage of 5 kV does not readily form a surface oxide at room temperature in comparison with an Al film deposited at a 1-kV acceleration voltage. This result indicates that Al films deposited by high acceleration voltage have high packing density and low gas incorporation. High corrosion resistance to humidity and good bondability can thus be expected in ICB Al films.

### 4.3.5 Step Coverage

Al interconnect films must completely cover the surface steps on the substrates. The step coverage characteristics of Al films on $SiO_2$ have been studied. Figure 4.19 shows the coverage on the beveled steps of common devices. Though the substrate temperature during the ICB deposition is as low as 50 - 90°C, these SEM photographs show good step coverage, which may be of practical use. When the film is deposited at a higher acceleration voltage, we can observe the wider thickness of the film at the step. This is probably due to the fact that adatom migration is enhanced when a higher acceleration voltage is applied to ICB.[23-25]

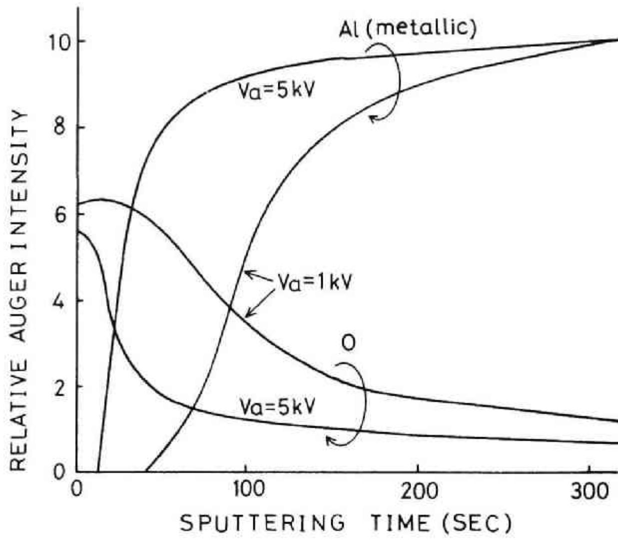


Fig. 4.18
Depth profiles of oxygen in ICB Al films measured by Auger electron spectroscopy combined with sputter etching.

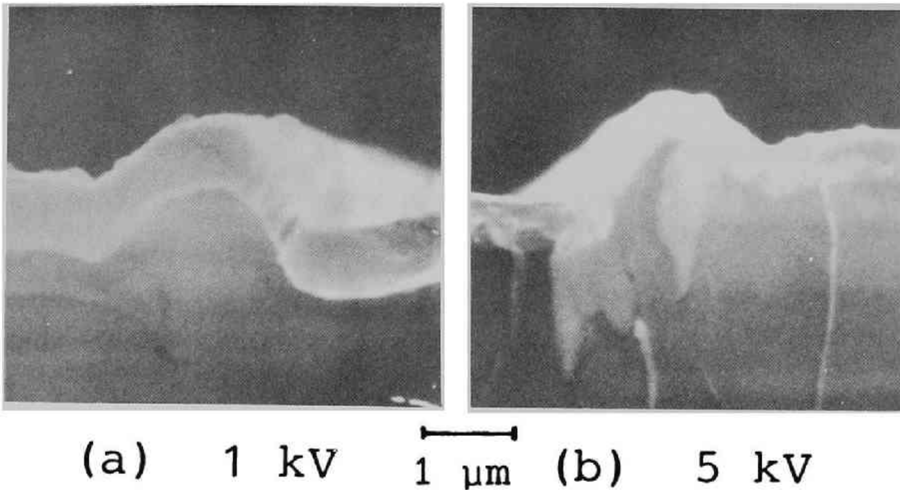


Fig. 4.19
Cross-sectional views of ICB Al films on beveled steps. (a) $V_a$ = 1 kV, (b) $V_a$ = 5 kV.

## 4.4 Al Epitaxy in an Ultra-High Vacuum

### 4.4.1 Experimental Conditions

In order to see the ultimate possibilities of the Al metallization, properties of the epitaxial Al films deposited on a clean Si surface[87)] by ICB are examined. Figure 4.20 shows the schematic diagram of the ICB source. Since both the crucible jacket and the substrate are grounded in this source, the geometry of the ionizer is modified so that ions are extracted more efficiently in the direction of the substrate, and the ion repeller is set to repel the ions produced around the crucible owing to the bombardment of the electrons which are used to heat the crucible. In this experiment acceleration voltage ($V_a$) of cluster ions, electron current for ionization ($I_e$), and ionization voltage ($V_e$) were set at 0.2 - 5 kV, 100 mA, and 200 - 500 V, respectively. Figure 4.21 shows the schematic diagram of the deposition chamber, which is equipped with an 5-keV electron gun and a fluorescent screen for reflection electron diffraction (RED), an Auger analyzer unit (a combination of a cylindrical-mirror analyzer, a 3-keV electron gun, and an ion gun) and a quadrupole mass analyzer. The deposition chamber was evacuated by a sputter ion pump and a titanium sublimation pump. The ICB source was surrounded by a liquid-nitrogen-cooled shroud. Residual gas pressure during deposition was maintained at less than $2 \times 10^{-7}$ Pa. Si(111) and Si(100) wafers were used as substrates. A protective oxide layer about 2-nm thick was formed by a mixture of $H_2O_2$ and $H_2SO_4$[70)] and this oxide layer was removed by heating the substrate at 800 - 1000°C for 5 - 30 min in vacuum just before the deposition. Figure 4.22 shows the differentiated Auger spectra before (a) and after (b) the heat treatment. Figure 4.23 shows the 5-keV RED patterns before (a) and after (b) the heat treatment. Thus a clean Si surface which gave the reconstructed RED patterns of Si(111)7X7 or Si(100)2X1, and showed

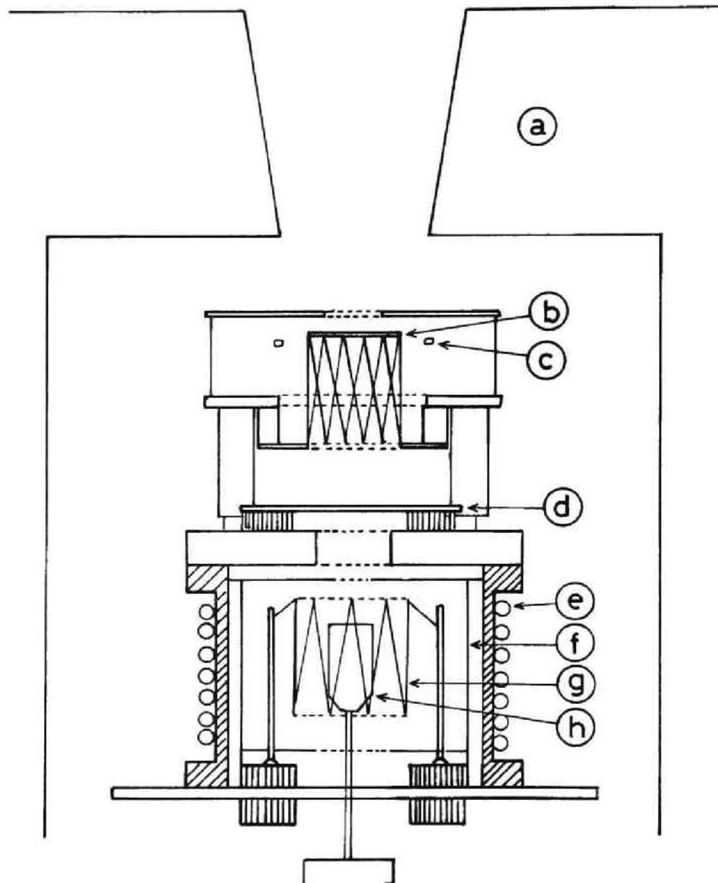


a: ionized cluster accelerating electrode (liq. $N_2$ shroud), b: electron accelerating electrode for ionization of cluster, c: electron emitter for ionization, d: ion repeller, e: tubes for cooling water, f: radiation shields, g: electron emitter for heating crucible, h: crucible.

Fig. 4.20

Schematic dagram of the ICB source used to deposit Al films in an ultra-high vacuum.

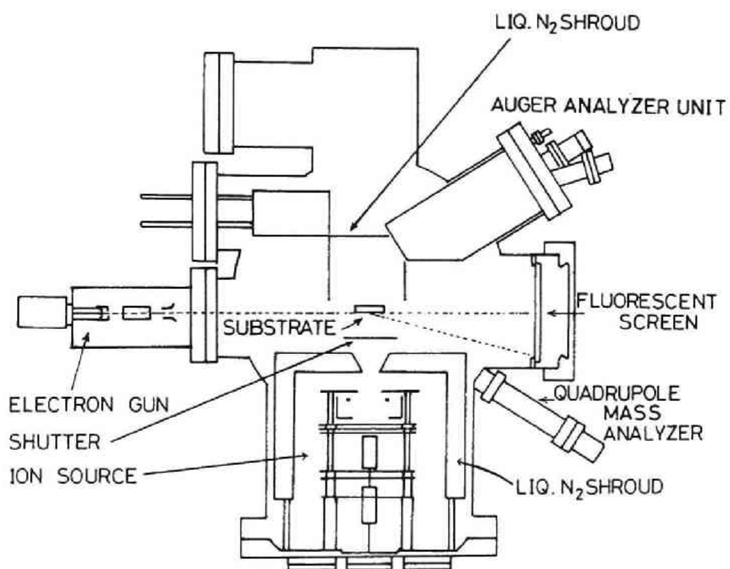


Fig. 4.21
Schematic diagram of the deposition apparatus.

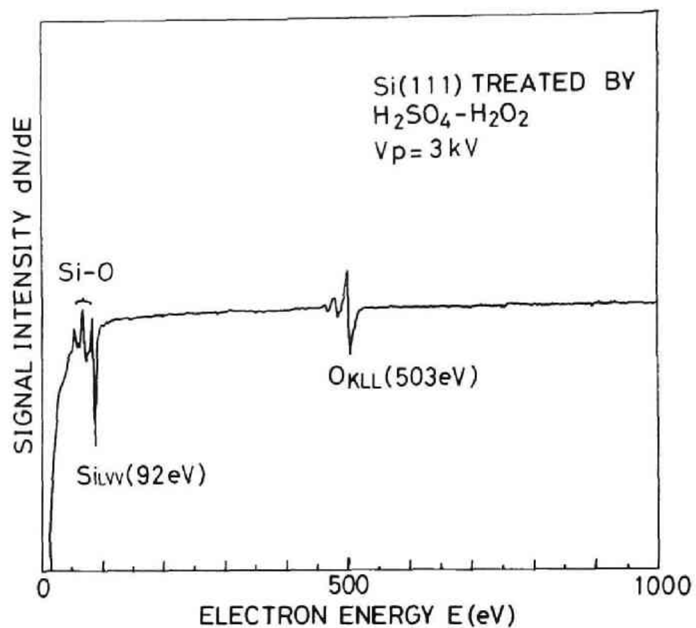


(a) before the heat treatment

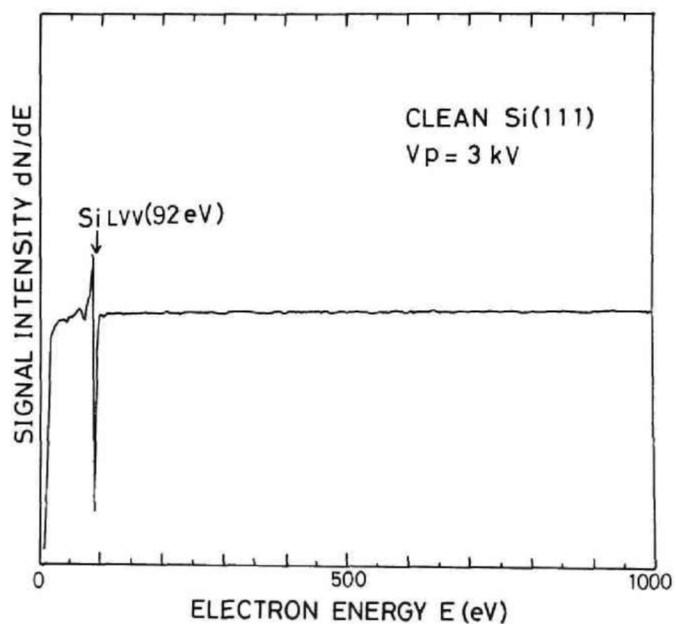


(b) after the heat treatment

Fig. 4.22
Auger spectra of Si(111) surface before (a) and after (b) the heat treatment at 1000°C for 5 min.

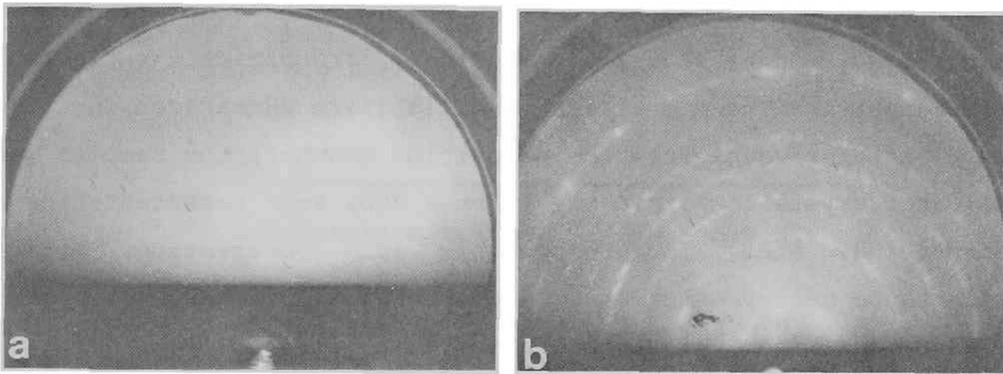


(a) before the heat treatment (b) after the heat treatment

Fig. 4.23
5-keV RED patterns of Si(111) surface before (a) and after (b) the heat treatment at 1000°C for 5 min.

no traces of carbon and oxygen by Auger electron spectroscopy (AES) analysis was obtained. The evaporant Al (99.999% purity) was heated in the graphite crucible (99.995% purity) which had been baked at 2000°C for 30 min in vacuum beforehand. The Si substrate was not intentionally heated during deposition and the substrate temperature ($T_S$) was confirmed to be less than 150°C by an infrared radiation pyrometer. Al was deposited stepwise at a low rate (3 nm/min) at the early stage of the deposition (less than 10 nm in thickness) for the ease of in-situ 5-keV RED observation, then the deposition rate was increased to 12 nm/min to form a 300 - 400 nm Al film. Sometimes films were deposited at a high rate (12 nm/min) from the beginning but no significant change was found by RED, ion channeling, or optical reflectance measurements. The deposition conditions are summarized in Table 4.4. After removal from the deposition chamber, the samples were evaluated crystallographically (75-keV RED, ion backscattering / channeleing, etc.), morphologically (SEM observation, optical reflectance measurement, etc.) and electrically (J-V measurement of Al-Si junctions, electromigration test, etc.).

### 4.4.2 Crystalline Orientation

In this experiment 5-keV RED was used to observe in situ the deposition processes and 75-keV RED in another vacuum system was used to examine Al films after the deposition. Because of the limited freedom of the target movement in the deposition chamber, precise determination of crystalline orientation by the 5-keV RED was difficult, so we will first describe the 75-keV RED analyses of the 360-nm thick Al films.

Figure 4.24 shows typical 75-keV RED patterns from an Al film on Si(111) and Fig. 4.25 shows their indices. In the case of Si[$\bar{1}$10] incidence of the electron beam (Fig. 4.25 (a)), Al($\bar{1}$10) reciprocal lattice can be seen, and in the case of Si[$\bar{2}$11] incidence (Fig. 4.25 (b)), Al($\bar{2}$11) reciprocal lattice can be seen,

Table 4.4 Deposition conditions of Al films by ICB in a ultra-high vacuum.

| Parameter | Value |
|---|---|
| Acceleration voltage | 0.2 - 5.0 kV |
| Electron current for ionization | 100 mA |
| Ionization voltage | 200 - 500 V |
| Substrate temperature | room temp. |
| Deposition rate | 3 - 12 nm/min |
| Film thickness | 300 - 400 nm |
| Background pressure | $2 \times 10^{-7}$ Pa |

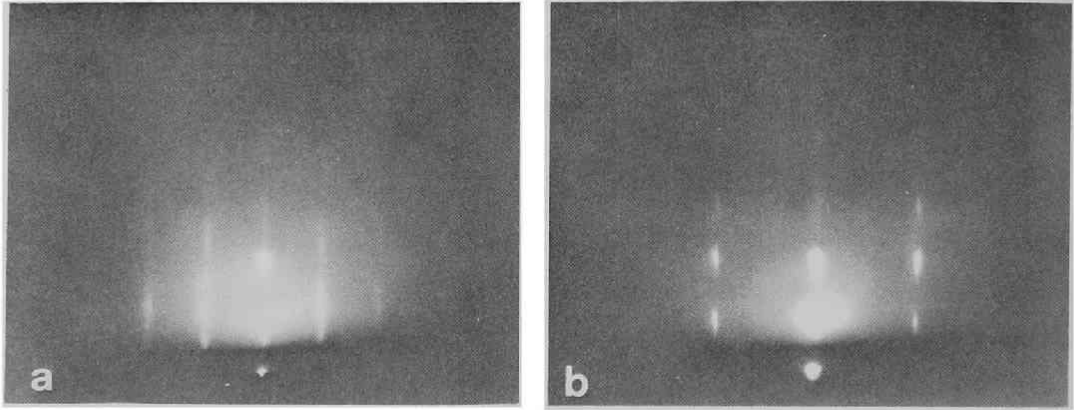


Fig. 4.24
75-keV RED patterns from an Al film on Si(111), deposited by ICB ($V_a$ = 5.0 kV, $I_e$ = 100 mA, and $T_s$ = room temperature). Incident electron beam is parallel to Si[$\bar{1}$10] (a), and Si[$\bar{2}$11] (b).

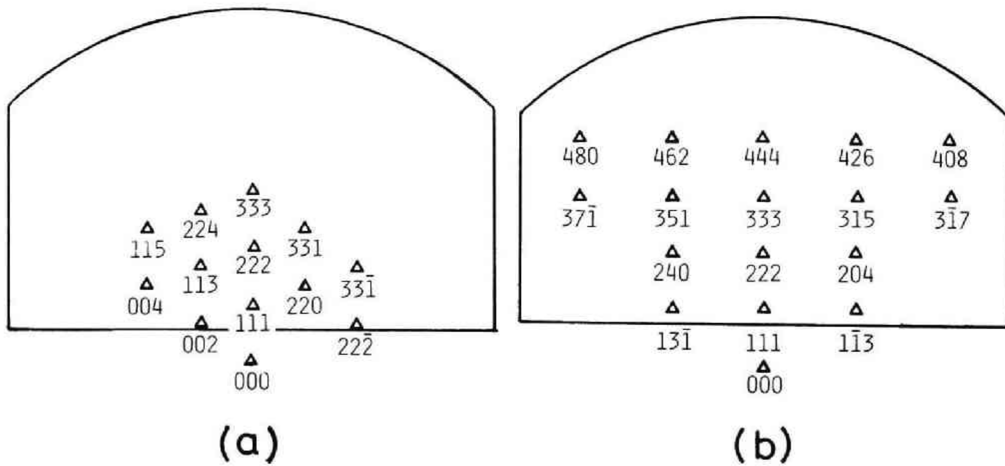


Fig. 4.25
Indices of the RED patterns in Fig. 4.24. The patterns correspond to Al($\bar{1}$10) reciprocal lattice (a), and Al($\bar{2}$11) reciprocal lattice (b).

which indicate the epitaxial relation:

$$Al(111)//Si(111),\ Al[\bar{1}10]//Si[\bar{1}10] \quad (4.13)$$

This relation is illustrated in Fig. 4.26.

Figure 4.27 shows the 75-keV RED patterns from an Al film on Si(100) and Fig. 4.28 shows their indices. Figure 4.27 (a) was obtained on Si[011] incidence of the electron beam and Fig. 4.27 (b) was obtained by rotating the sample azimuthally by 35° from the condition of Fig. 4.27 (a). These patterns can be identified as superposition of two Al patterns with epitaxial relations:

$$Al(110)//Si(100),\ Al[001]//Si[011], \quad (4.14)$$

denoted as Al(110), and

$$Al(110)//Si(100),\ Al[\bar{1}10]//Si[011], \quad (4.15)$$

denoted as Al(110)R. These relations are illustrated in Fig. 4.29. It is to be noted that these orientations are orthogonal and identical with each other. Orientation of the film was also confirmed by 160-keV $H^+$ channeling measurement. Figure 4.30 shows the stereographic projection of the crystal planes around the normal axis of the Al film. This stereographic projection clearly shows that the Al(110) is parallel to the Si(100) and does not contradict the existence of the two orientations in a film. Figure 4.31 shows the dependence of the backscattering yield on rotation angle, measured to determine the stereographic projection (Fig. 4.30). It can be seen that the depth of each dip of the backscattering yield is nearly the same, which supports the existence of two orientations within a film.

It is remarkable that a lattice misfit as large as (2.86 - 3.84)/3.84 X 100 = -25%, at least in one direction, permits epitaxial growth of Al on both Si(111) and Si(100) substrate.

#### 4.4.3 Observation of the Initial Stage of the Deposition

The deposition process of the Al film was observed by in-situ 5-keV RED and AES. Figure 4.32 shows the change of a 5-keV RED pattern during the Al deposition on Si(111). A spotty and

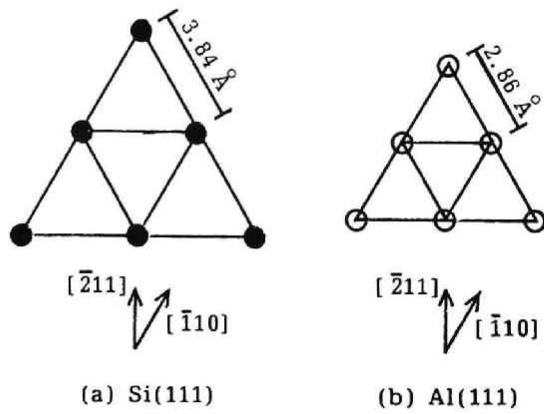


Fig. 4.26
Schematic illustrations of relative orientation of an Al film on Si(111) substrate.

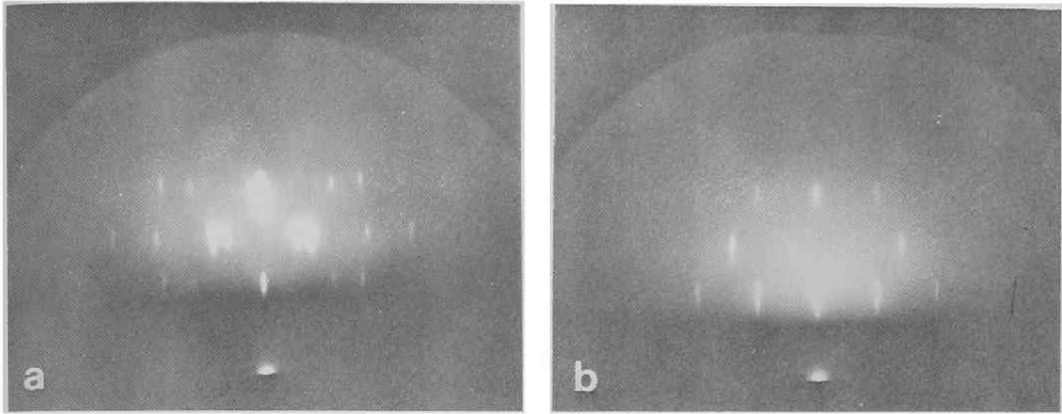


Fig. 4.27
75-keV RED patterns from an Al film on Si(100), deposited by ICB ($V_a$ = 0.2 kV, $I_e$ = 100 mA, and $T_s$ = room temperature). (a) incident electron beam is parallel to Si[011], (b) the sample is rotated azimuthally by 35° from the condition of (a).

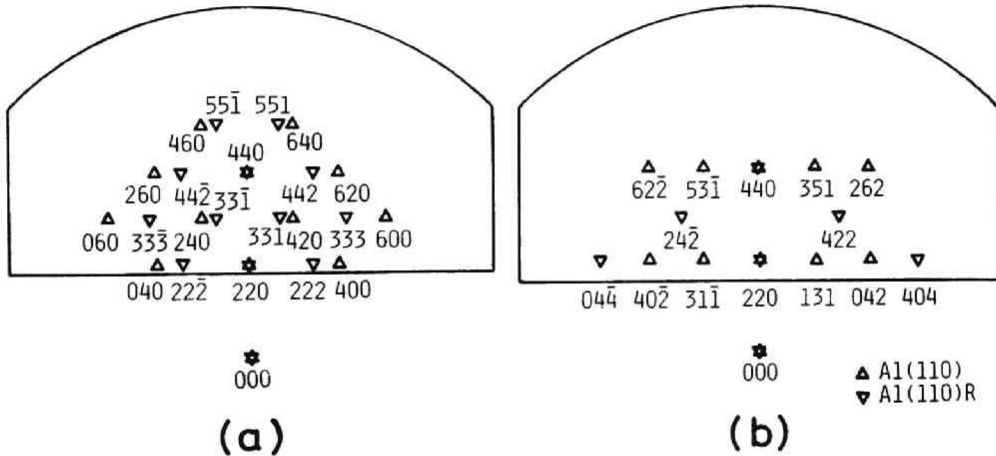


Fig. 4.28
Indices of the RED patterns in Fig. 4.27. Diffraction from Al(110) crystal corresponds to Al(001) reciprocal lattice (a), and Al(1$\bar{1}$2) reciprocal lattice (b). Diffraction from Al(110)R crystal corresponds to Al($\bar{1}$10) reciprocal lattice (a), and Al($\bar{1}$11) reciprocal lattice (b).

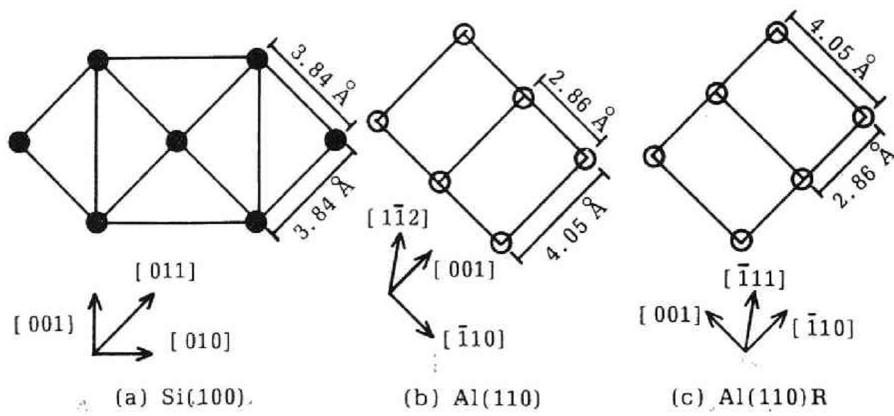


Fig. 4.29
Scehmatic illustrations of relative orientation of an Al film on Si(100) substrate.

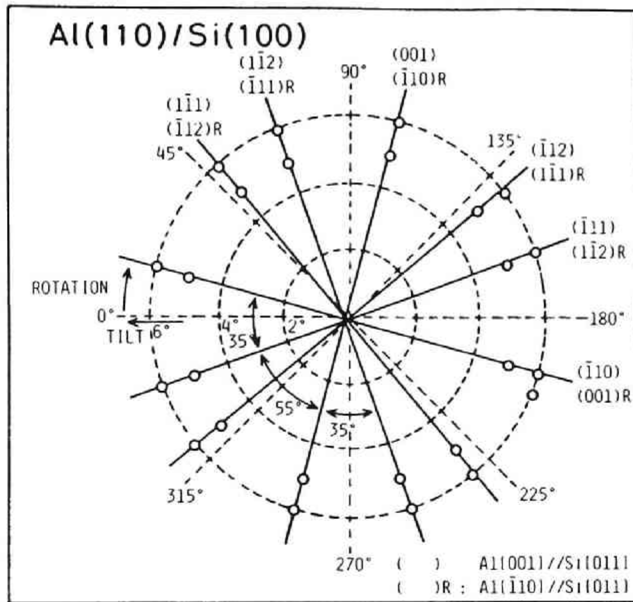


Fig. 4.30
Stereographic projection of the crystal planes around the normal axis of an Al film on Si(100), deposited by ICB ($V_a$ = 0.2 kV, $I_e$ = 100 mA, and $T_s$ = room temperature). 160-keV $H^+$ backscattering and channeling technique was used to determine this projection.

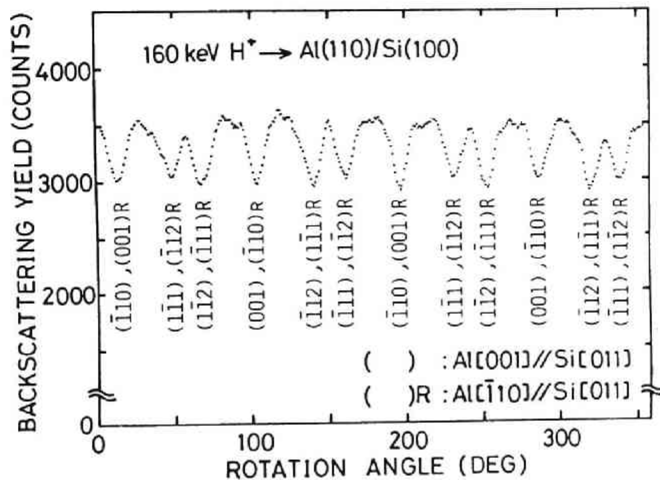


Fig. 4.31
Dependence of backscattering yield on the azimuthal rotation angle of Al film on Si(100), deposited by ICB ($V_a$ = 0.2 kV, $I_e$ = 100 mA, and $T_s$ = room temperature). Tilt angle was fixed at 5°.

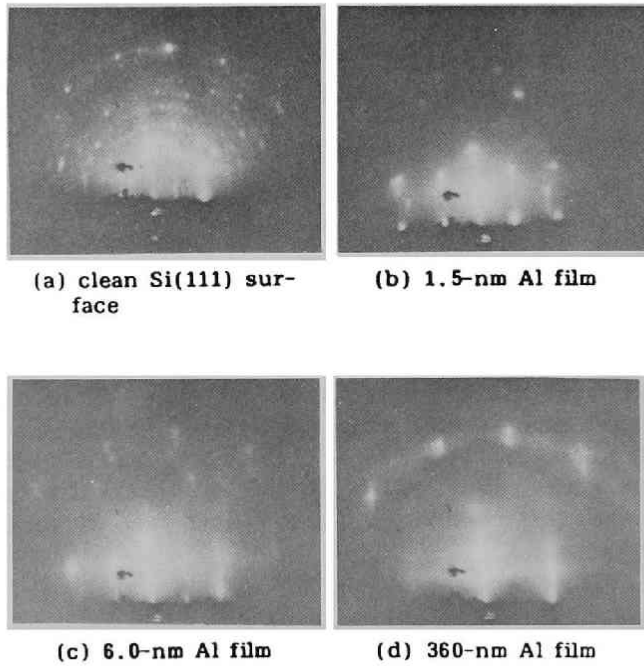

(a) clean Si(111) surface

(b) 1.5-nm Al film

(c) 6.0-nm Al film

(d) 360-nm Al film

Fig. 4.32
5-keV RED patterns during Al deposition by ICB ($V_a$ = 5 kV, $I_e$ = 100 mA, and $T_s$ = room temperature). Incident electron beam was parallel to Si[$\bar{2}$11] (a) clean Si(111) surface before deposition, (b) 1.5-nm thick Al film, (c) 6.0-nm thick Al film, and (d) 360-nm thick Al film.

complex pattern appears at the first stage (Fig. 4.32 (b)) which corresponds to the three dimensional nucleation of Al with several orientations. After further deposition this pattern becomes streaky and one orientation expressed by eq. (4.13) becomes dominant (Fig. 4.32 (c)). After the deposition of more than 10-nm of Al film, only one orientation remains and the RED pattern does not change to the end of the deposition of the 360-nm thick Al film (Fig. 4.32 (d)). This deposition process feature did not fundamentally change when the acceleration voltage (Va) of cluster ions was changed from 0.2 to 5.0 kV. The RED pattern became streaky at an earlier stage of deposition when the higher $V_a$ was applied.

In order to examine the pattern of Fig. 4.32 (b) precisely, the sample at this stage was removed from the deposition chamber and was observed by 75-keV RED. Figure 4.33 shows the RED pattern obtained when the electron beam is parallel to Si[$\bar{2}$11] direction. This pattern appeared at every 30° rotation of the azimuthal angle. The RED pattern of Fig. 4.33 is indexed in Fig. 4.34. Al(011), Al(013) and Al(0$\bar{1}$5) reciprocal planes can be seen simultaneously and three crystalline orientations are believed to exist in the film. Taking symmetry into account, the dominant orientations*) of the Al crystal at the initial stage of

---

Note:

*) It is natural to consider that the orientation of eq.(4.13) also exists at the initial stage of deposition because the stacking sequence of atomic layers is preserved, ie., Al(111) //Si(111), Al[1$\bar{1}$0]//Si[$\bar{1}$10] orientation does not coexist with Al(111)//Si(111), Al[$\bar{1}$10]//Si[$\bar{1}$10] orientation (eq.(4.13)) at later stage of deposition. It is likely that the Al(100) crystals (eqs.(4.16)-(4.18)) form three-dimensional nuclei resulting in strong spotlike diffraction and shadow the Al(111) crystals (eq.(4.13)).

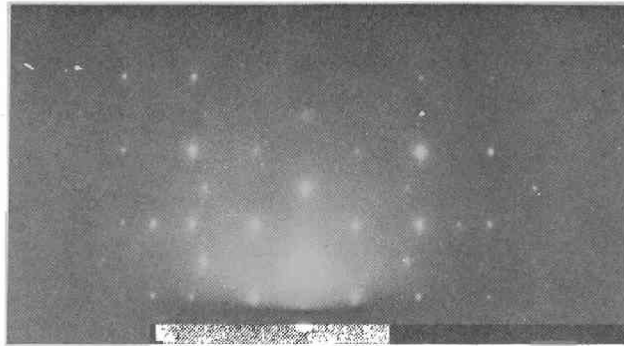

Fig. 4.33
75-keV RED pattern corresponding to Fig. 4.32 (b).

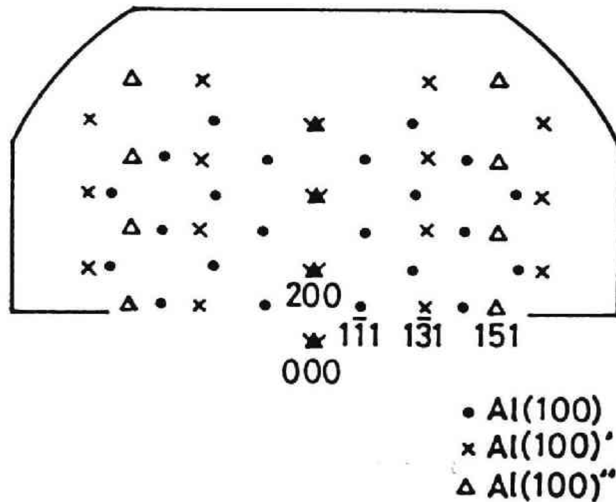


Fig. 4.34
Indices of the RED pattern in Fig. 4.33. Spots of Al(100) crystal correspond to Al(011) reciprocal plane, Al(100)' to Al(013), and Al(100)'' to Al($0\bar{1}5$).

deposition were determined to be as follows:

$$Al(100)//Si(111),\ Al[011]//Si[\bar{2}11], \tag{4.16}$$

denoted as Al(100)

$$Al(100)//Si(111),\ Al[011]//Si[\bar{1}10], \tag{4.17}$$

denoted as Al(100)', and

$$Al(100)//Si(111),\ Al[011]//Si[\bar{1}2\bar{1}], \tag{4.18}$$

denoted as Al(100)''. Figure 4.35 illustrates the relative orientations between Si substrate and Al film. Since [011] direction of the Al(100) crystal (Fig. 4.35 (b)), [013] direction of the Al(100)' crystal (Fig. 4.35 (c)), and [0$\bar{1}$5] direction of the Al(100)'' crystal (Fig. 4.35 (d)) are nearly parallel to each other, corresponding diffraction patterns can be observed simultaneously when the electron beam enters the Si[$\bar{2}$11] direction, as is seen in Fig. 4.33. Lattice misfit is (2.86-3.84)/3.84 X 100 = -25% in one direction and (5.73-6.65)/6.65 X 100 = -14% in the other direction. This lattice misfit is smaller than that of Al(111)//Si(111), Al[$\bar{1}$10]//Si[$\bar{1}$10] orientation observed at the later stage of film deposition, which could be (4.05-5.43)/5.43 X 100 = -25% in all directions. It seems that, at the initial stage of deposition, Al(100)//Si(111) growth is favored because of the relatively small lattice misfit, and at the later stage Al(111)//Si(111) growth becomes dominant in order to reduce interfacial energy at the grain boundary and surface energy at the film surface.[71)]

In the case of deposition on Si(100), the deposition process was completely different. The RED pattern did not change from the beginning (2-nm thick stage) to the end (360-nm thick stage), which means that the crystalline orientations of 360-nm thick Al film expressed by eqs. (4.14) and (4.15) appears at the early stage of deposition and the orientation does not change during deposition.

Figure 4.36 shows the ratio of peak-to-peak intensities of differentiated Auger signals corresponding to $Al_{KLL}$ (1396 eV) and

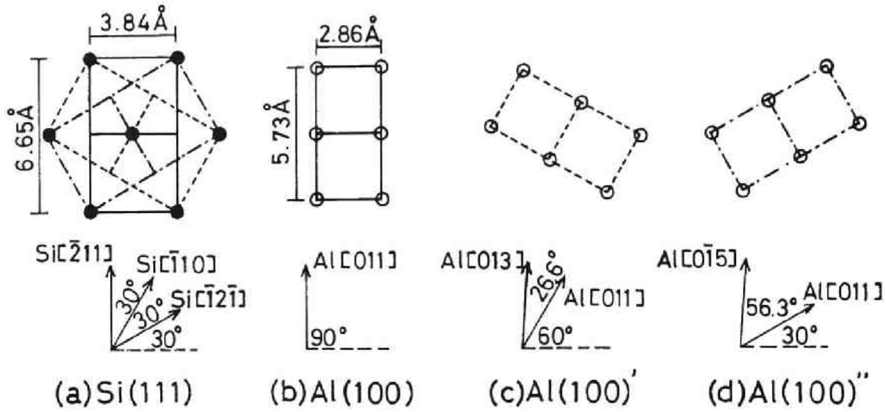


Fig. 4.35
Schematic illustrations of relative orientation of the Al crystals on Si(111) substrate at the initial stage of deposition.

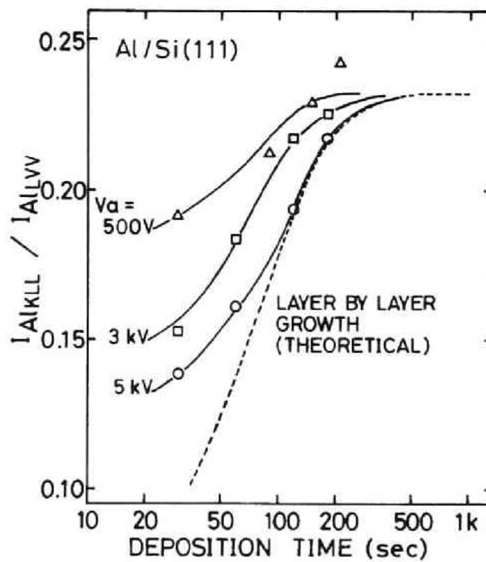


Fig. 4.36
Ratios of differentiated Auger peaks of $Al_{KLL}$ and $Al_{LVV}$ transitions as function of deposition time.

$Al_{LVV}$ (68 eV) transitions as a function of deposition time. Since the escape depth of a 1396-eV electron is longer than that of a 68-eV electron, the intensity ratio $I_{KLL}/I_{LVV}$ corresponds to island height of the film. Because the mass deposition rate was held constant at 3 nm/min in this case, the variation of $I_{KLL}/I_{LVV}$ among films deposited at various acceleration voltages ($V_a$) is due to the change in growth morphology of the films. If the growth of a film proceeds layer by layer, Auger signal intensity I from the film changes as follows.[72]

$$I = I_0 [1 - exp(-t/L)] \tag{4.19}$$

where $I_0$ is signal intensity from a film with infinite thickness, t is the film thickness, and L is the escape depth of electron given by

$$L = l \cos(\phi) \tag{4.20}$$

where l is the electron mean free path and $\phi$ is the angle with respect to the surface normal with which the electron leaves the sample. We used $\phi = 38°$, $l = 0.4$ nm for 68-eV electron and $l = 1.9$ nm for 1396-eV elctron[72] to calculate the theoretical curve shown in Fig. 4.36. It is to be noted that a change in deposition rate results in lateral shift of the curve without changing the shape of it. As is seen in Fig. 4.36, the growth morphology of the ICB Al films at higher acceleration voltages, i.e., 3 keV and 5 keV, is nearly layer-by-layer growth. This result corresponds to the previous RED observation that the film surface became flat at the earlier stage of deposition when higher $V_a$ was applied.

#### 4.4.4 SIM Observations

It is known that secondary electron images by scanning ion microscope (SIM) can provide crystallographic information through channeling contrast even if the surface of the sample is smooth.[73] By using this technique we examined the epitaxial Al films. Fig. 4.37 shows 100 keV $Ga^+$ SIM photographs of Al films deposited

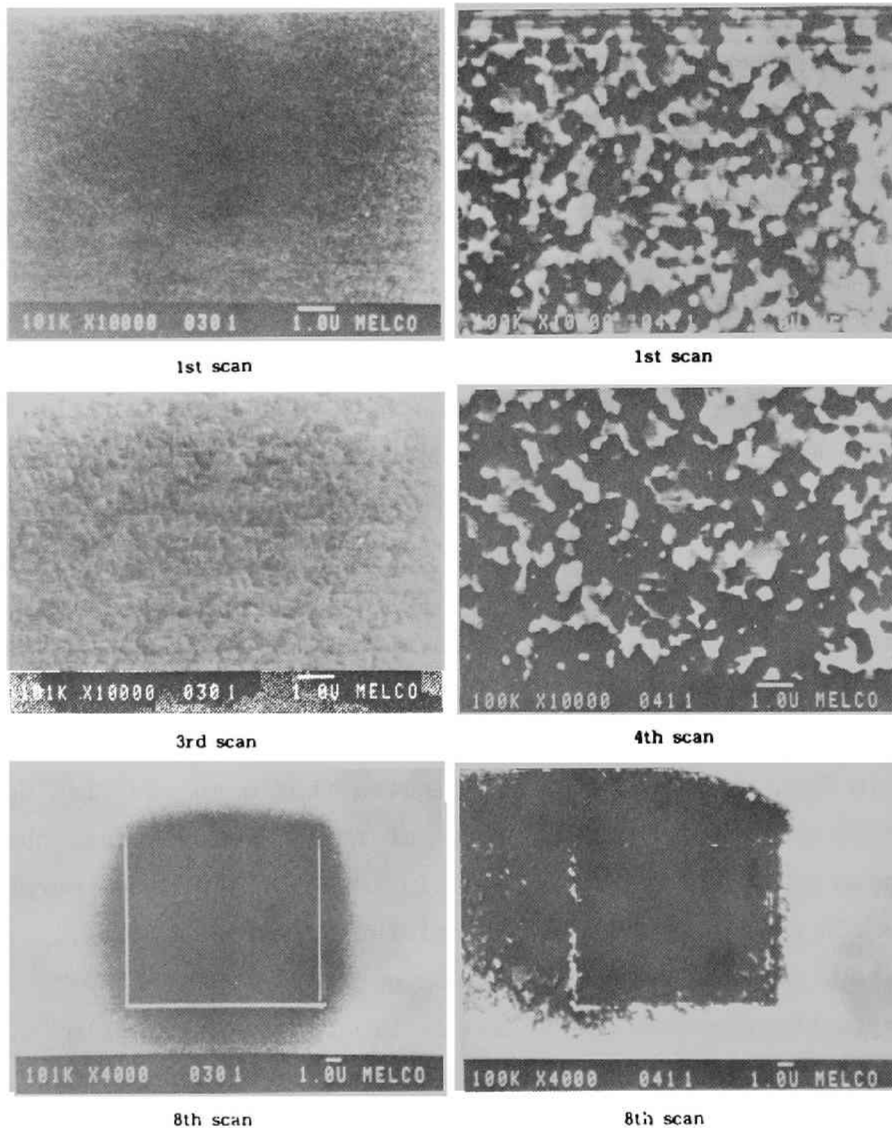


Fig. 4.37
Scanning ion micrographs (100 keV, $Ga^+$) of Al films on Si substrate, deposited by ICB ($V_a$ = 0.2 kV, $I_e$ = 100 mA, $T_s$ = room temperature) and conventional sputter deposition ($T_s$ = room temperature). By ICB deposition, Al(111) grows epitaxially on Si(111) substrate.

by ICB and by conventional sputter deposition. As the sputtered Al film is polycrystalline, contrast between constituent grains is formed whereas no crystallographic contrast can be seen in the ICB Al film. This clearly indicates the structural uniformity of the epitaxial Al films.

An Al film was deposited on a 100-nm layer of oxidized silicon etched into a line-and-space pattern and observed by SEM and SIM. Figure 4.38 (a) shows the SEM image of the substrate surface which is not covered with Al film. The narrower lines are of oxide. Figure 4.38 (b) shows the SEM image of the Al film surface. The film on the oxide is slightly rougher than that on the bare Si. Figure 4.38 (c) and (d) show the SIM images of the sample. The film on the bare Si is crystallographically smooth (ie. epitaxially grown), while the film on the oxide consists of poly-crystalline grains. It can be seen from these figures that the epitaxial film is smoother than the poly-crystalline film, and that since the epitaxial region is confined on the bare Si surface, a crystalline insulator substrate must be used to realize fully epitaxial Al metallization.

#### 4.4.5 Crystalline Quality

Crystalline quality of the Al films was examined by 160-keV $H^+$ backscattering and channeling analysis. Figure 4.39 shows the channeled backscattering spectra obtained from Al films deposited on Si(111) at acceleration voltages ($V_a$) of 0.5 kV, 3.0 kV, and 5.0 kV, Al films deposited on Si(100) at 0.2 kV, and a bare Si(111) wafer. Apparently the channeled yield decreases as the $V_a$ increases in the case of the films on Si(111). This is probably due to the fact that the accelerated clusters break up and migrate more effectively on the surface, leading to the enhancement of crystal growth. The $X_{min}$, defined as the ratio of the integrated yields of the channeled and the random spectra corresponding to the depth from 0 to 50 nm, were 22% for the Al film deposited on

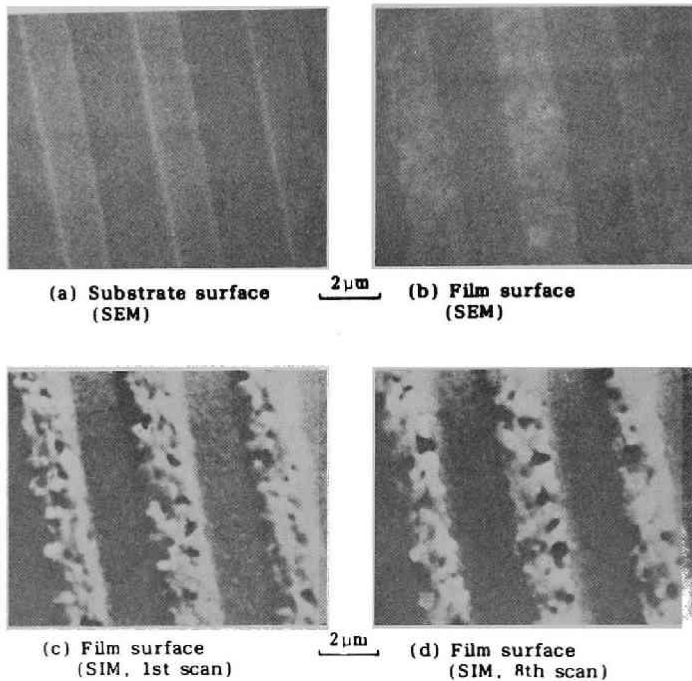


Fig. 4.38
Scanning electron micrographs (SEM) and scanning ion micrographs (SIM) of an ICB Al films ($V_a$ = 5 kV, $I_e$ = 100 mA, $T_s$ = room temperature) on a Si(111) substrate with lines of 100-nm thick oxide. Narrower lines on the substrate are the oxide.

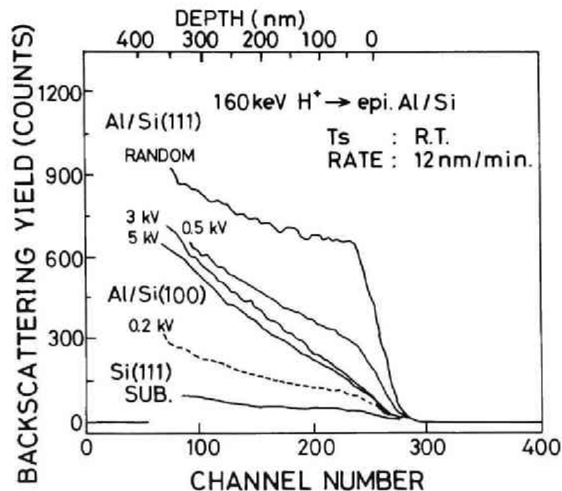


Fig. 4.39
Channeled backscattering spectra obtained from Al films on Si(111) and Si(100), deposited by ICB ($I_e$ = 100 mA, and $T_s$ = room temperature) at various acceleration voltages ($V_a$). Spectrum from a bare Si(111) wafer is also shown as the reference.

Si(111) at 5.0 kV, 15% for the Al film on Si(100) at 0.2 kV, and 6% for the bare Si(111) wafer. The reason for the $\chi_{min}$ of the film on Si(100) to be lower than that of the film on Si(111) is probably that the lattice misfit of the Al(110) on Si(100) is less than that of the Al(111) on Si(111), and that the $\chi_{min}$ for the <110> channel is less than that for the <111> channel because of the smaller atomic spacing along channel for the former.[75]

#### 4.4.6 Optical Reflectance

Optical reflectance is a good measure of the surface flatness and the resistance to oxidation of the film,[72] which are important factors for device applications. Figure 4.40 shows the reflectance of Al films deposited at various acceleration voltages ($V_a$), as a function of wavelength. Reflectance of the films is generally high and is further improved as the higher $V_a$ is applied. Degradation of reflectance in the short-wavelength region is also small. Reflectance of the film deposited at $V_a$ of 5 kV exceeds 90% in the wavelength region of 220 to 760 nm. These facts indicate that the ICB deposited film has a flat surface and high resistance to oxidation, and such characteristics become better by applying higher $V_a$.

#### 4.4.7 Morphological Stability

Changes in the morphology of the surface and the interface after annealing at 450°C, 500°C, and 550°C for 30 min were examined by SEM and AES with sputter etching. Figures 4.41 and 4.42 show the SEM images of the surface and the interface revealed by phosphoric acid etching after annealing at 450 and 550°C, respectively, in comparison with those by conventional vacuum deposition. On the surface of the Al film deposited by conventional vacuum deposition and annealed at 450°C, as is often observed, there are annealing hillocks, while nothing can be seen on the surface of the Al film deposited by ICB and annealed

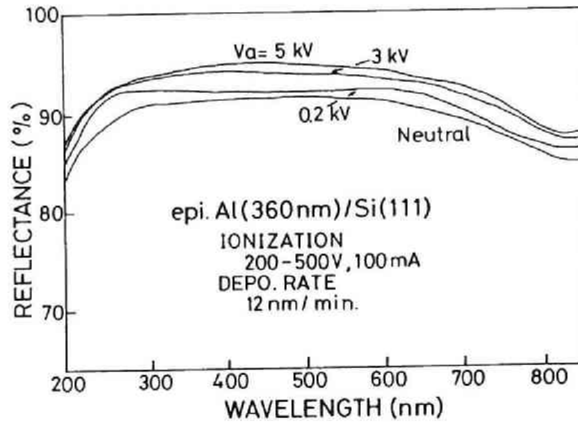


Fig. 4.40

Reflectance of the ICB deposited ($I_e$ = 100 mA, and $T_s$ = room temperature) Al films on Si(111) as a function of wavelength. Films were deposited at $V_a$ = 0.2, 3.0 and 5.0 kV, and without ionization of clusters (denoted as neutral).

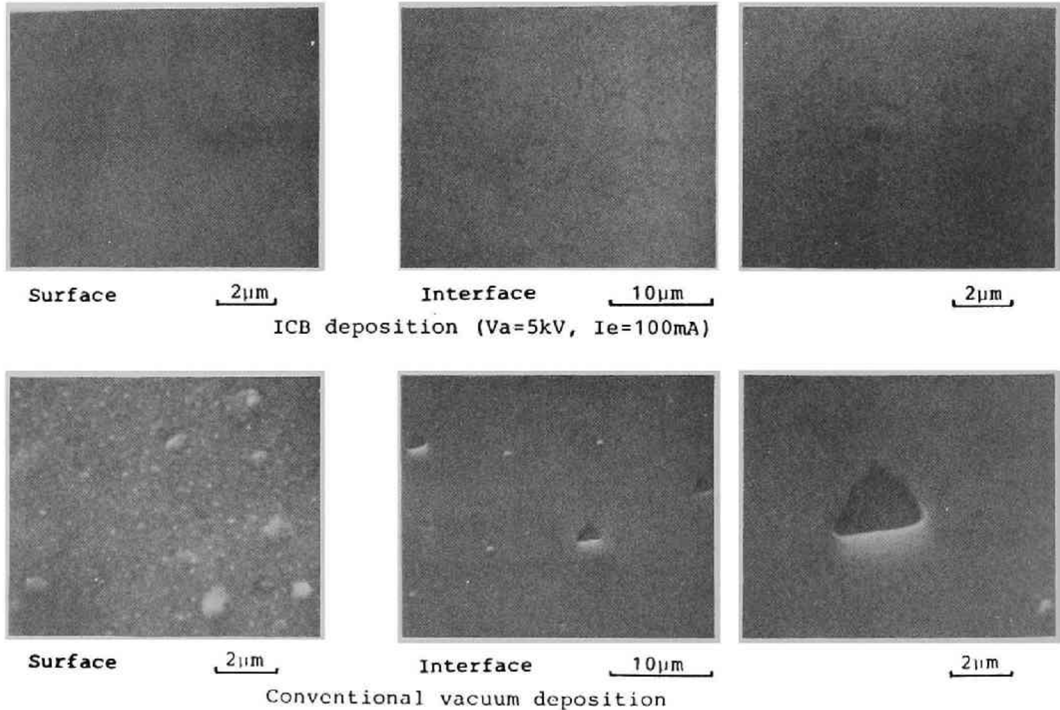


Fig. 4.41

SEM images of the surface and the interface of Al films on Si(111), post-annealed at 450 °C for 30 minutes in vacuum. (a) surface of an Al film deposited by ICB ($V_a$ = 5.0 kV, $I_e$ = 100 mA, and $T_s$ = room temperature), (b) interface of (a), (c) surface of an Al film deposited by conventional vacuum deposition, and (d) interface of (c).

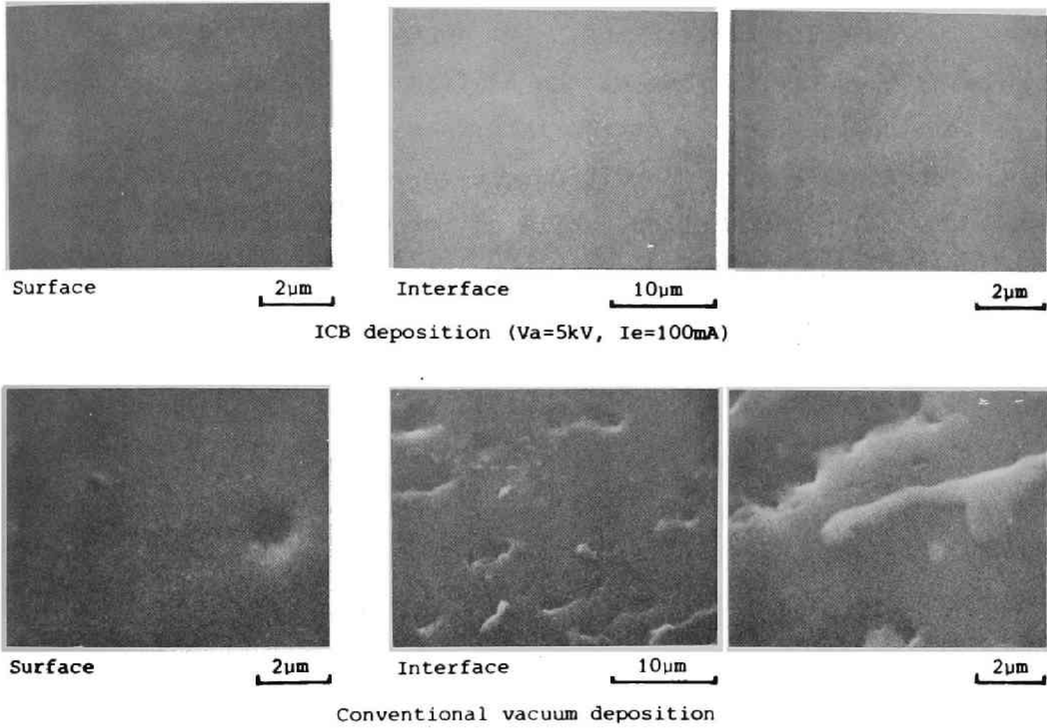


Fig. 4.42
SEM images of the surface and the interface of Al films on Si(111), post-annealed at 550 °C for 30 minutes in vacuum. (a) surface of an Al film deposited by ICB ($V_a$ = 5.0 kV, $I_e$ = 100 mA, and $T_s$ = room temperature), (b) interface of (a), (c) surface of an Al film deposited by conventional vacuum deposition, and (d) interface of (c).

identically. At the interface of the sample prepared by conventional vacuum deposition, there are triangular pits caused by so-called alloy penetration, while no pit can be seen at the interface of the ICB deposited sample. On the surface of the Al film deposited by conventional vacuum deposition and annealed at 550°C, there are annealing hillocks and valleys probably caused by the extended alloy penetration. No annealing hillock or valley can be seen on the surface of the Al film deposited by ICB and annealed identically. At the interface of the sample prepared by conventional vacuum deposition, there are strong undulations caused by alloy penetration, while no irregularity can be seen at the interface of the ICB deposited sample.

Figure 4.43 shows AES depth profiles of the Al-Si interface. Figure 4.43 (a) is of the sample deposited by ICB and annealed at 550°C for 30 min and (b) is of the sample by conventional vacuum deposition and annealed identically. The FWHM resolution of the AES system was measured to be about 20 nm by using an identical sample which had not been annealed. It can be seen that the interface of the sample deposited by ICB remains abrupt even after annealing at 550°C.

As discussed in Section 4.1, degradation of the Al-Si interface after annealing is explained to be the result of the nonuniform dissolution of Si into Al. High stability of the interface of the ICB deposited sample is probably due to the uniformity of the interface and the limited diffusion of Si in epitaxially grown Al film.

#### 4.4.8 Crystallographical Stability

When an Al film on Si is annealed, the Si dissolves into the Al and this phenomenon causes troubles such as alloy penetration (see Section 4.1). Since the solid solubility of Si in Al reaches 1.25 at.% at 550°C in thermal equilibrium,[9] dissolved Si may affect the crystalline quality. 1.5-MeV $He^+$ and 165-keV $H^+$

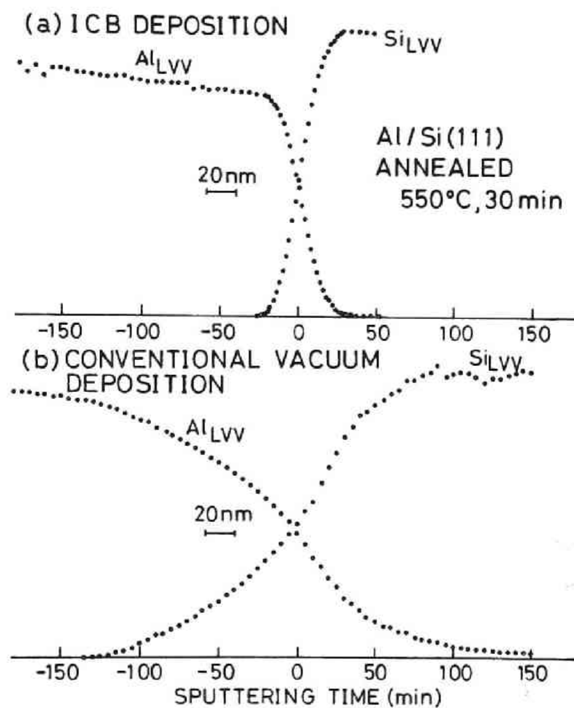


Fig. 4.43
AES depth profiles of Al-Si interfaces after annealing at 550°C for 30 min. (a) a sample deposited by ICB ($V_a$ = 5 kV, $I_e$ = 100 mA, $T_s$ = room temperature), and (b) a sample by conventional vacuum deposition.

backscattering / channeling were used to evaluate the crystalline quality of the Al film before and after annealing. Figure 4.44 shows the spectra obtained by 1.5-MeV $He^+$ of Al<111> incidence*) before (a) and after (b) annealing at 500°C for 30 min. Spectra corresponding to the Al film and the Si substrate overlap at about 180 ch. and produce a sharp peak. Spectra before and after anneal show the same features, indicating no interaction occured between Al and Si. The slope of the aligned spectrum (a measure of the degree of dechanneling) is reduced after anneal, indicating crystalline quality improved. Figure 4.45 shows the spectra obtained by 1.5-MeV $He^+$ of Al<100> incidence before and after annealing at 500°C for 30 min. Seen from the Al<100> direction, crystallinity of the ICB Al film even gets better after annealing at 500°C. It is likely that in the as-deposited Al film there exists variation of crystalline orientation around the axis normal to the film surface, and this variation of orientation is reduced after annealing. Figure 4.46 is the dependence of the minimum yield $\chi_{min}$ obtained by 165-keV $H^+$ beam of Al<111> incidence on the annealing temperature. From these backscattering spectra it can be said that the crystallinity of the ICB Al film improves after annealing at less than 500°C and degrades little even after annealing at 550°C.

### 4.4.9 Electrical Stability

Recrystallization of Si which has been dissolved in Al causes troubles such as an increase in contact resistance on $n^+$-Si and an

---

Note:

*) It was found that Al<111> axis is tilited from Si<111> axis by more than 0.7°. So the ion beam was aligned to the axis of the film crystal in ion channeling measurements. Tilt of crystalline axes was also appreciable in $CaF_2$(111)/Si(111) and Al(111)/$CaF_2$(111) samples (section 4.4.13).

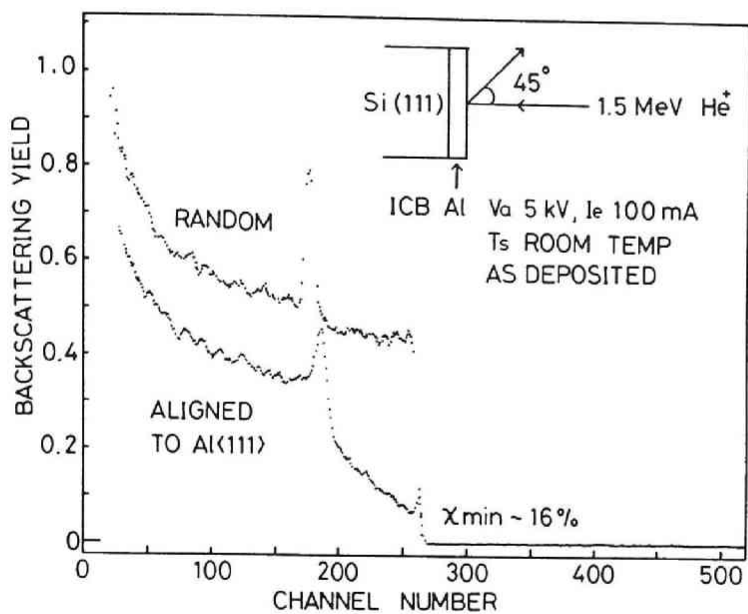


(a) before annealing

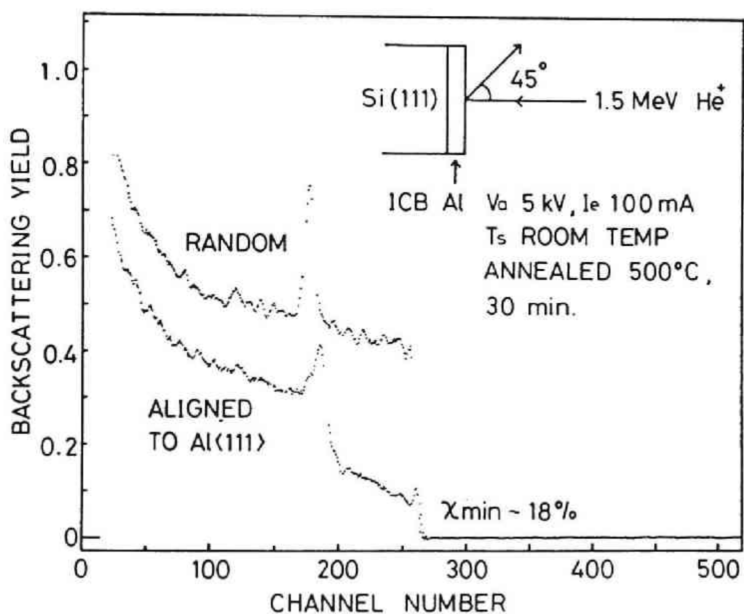


(b) after annealing

Fig. 4.44
1.5-MeV $He^+$ backscattering / channeling spectra of the ICB Al film on Si(111) before (a) and after (b) annealing at 500°C for 30 min. Incident ion beam is aligned to Al<111>.

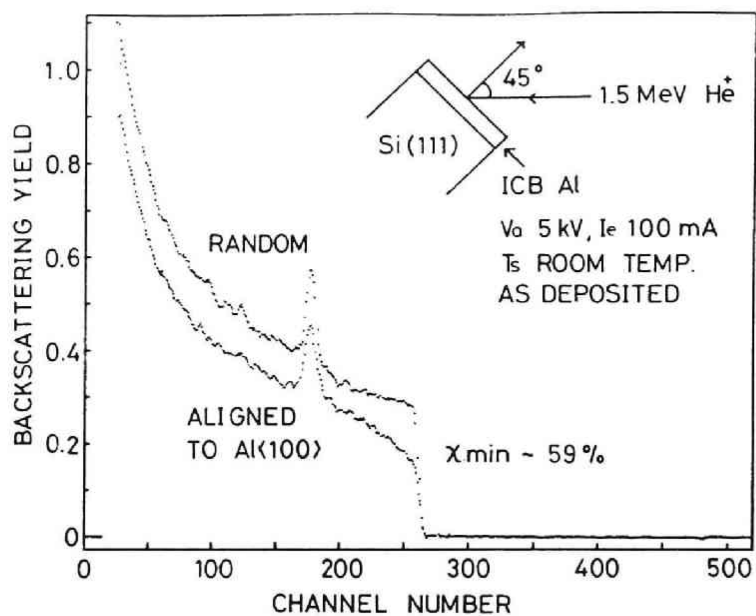


(a) before annealing

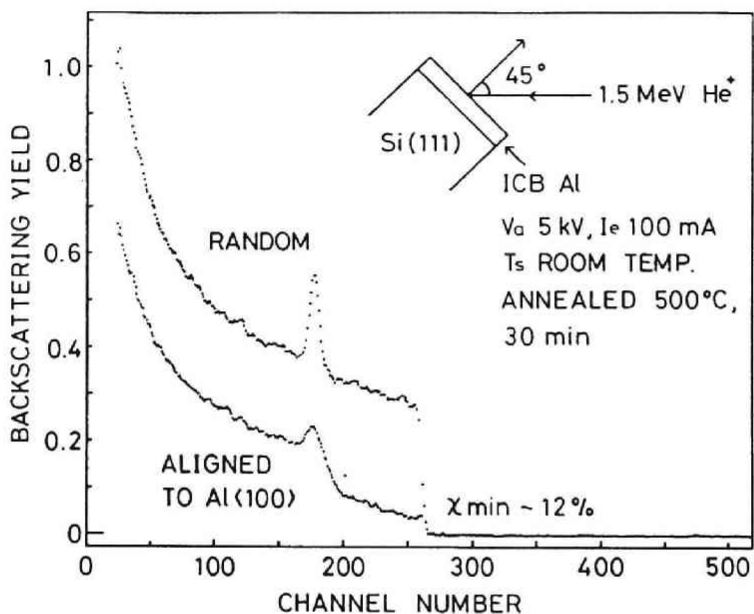


(b) after annealing

Fig. 4.45
1.5-MeV $He^+$ backscattering / channeling spectra of the ICB Al film on Si(111) before (a) and after (b) annealing at 500°C for 30 min. Incident ion beam is aligned to Al<100>.

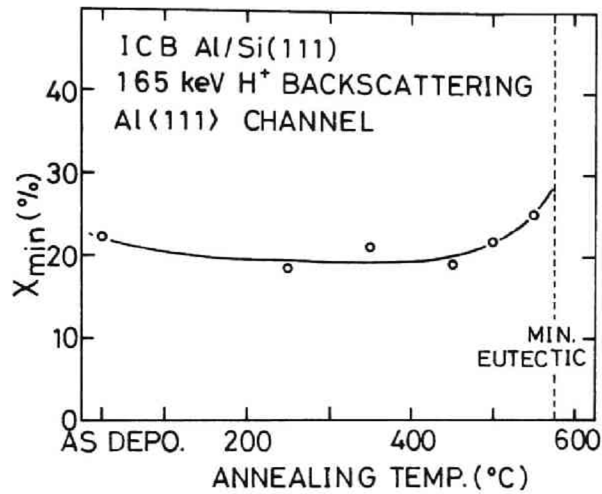


Fig. 4.46

Dependence of the minimum yield $\chi_{min}$ on annealing temperature, measured by 165-keV $H^+$ beam of Al<111> incidence. The ICB Al films were deposited under $V_a$ = 5 kV, $I_e$ = 100 mA, and $T_s$ = room temperature and postannealed at various temperatures for 30 min.

increase in barrier height of an Al-n-Si junction (see section 4.1). Morphological change in the Al-Si interface degrades or completely destroys the device beneath the Al film. In this experiment Al-n-Si (0.7 Ωcm) junctions of 1-mm diameter were fabricated and the current density-voltage (J-V) and 1-MHz capacitance-voltage (C-V) characteristics were measured before and after annealing at 450°C, 500°C, and 550°C. Figure 4.47 shows the J-V characteristics of the junctions. The extraporated value of current density at zero voltage, which is related to barrier height,[77] remains stable after annealing. Figure 4.48 shows the dependence of the barrier height and the forward n value on the annealing temperature, calculated from the J-V characteristics in Fig. 4.47. The barrier height and the n value are around 0.75 eV and 1.17, respectively. Changes in the barrier height and the n value are 0.03 eV and 0.02, respectively, while in the case of Al-Si junctions fabricated by conventional deposition techniques, changes of more than 0.1 eV and 0.1, respectively are reported.[12,15] It is estimated that the dissolution and/or the recrystallization of Si are suppressed in the epitaxial Al films deposited by ICB.

Figure 4.49 shows the C-V characteristics of the Al-Si junctions. From the intercept on the voltage axis, the barrier height can be calculated.[77] The change in the barrier height after annealing is found to be less than 0.04 eV and the thermal stability of the epitaxial Al-Si junction is confirmed. However, the barrier height by C-V measurement is around 0.92 eV and is considerably higher than that by J-V measurement. In these experiments the Si substrates were heated at 1000°C for 10 min in vacuum before deposition and this process can cause diffusion and electrical activation of the adsorbed boron on the substrate surface[78,79] and the large shift of the barrier height by C-V measurement. The source of the boron is considered to be the glass window of the deposition chamber[78] or the glassware used in

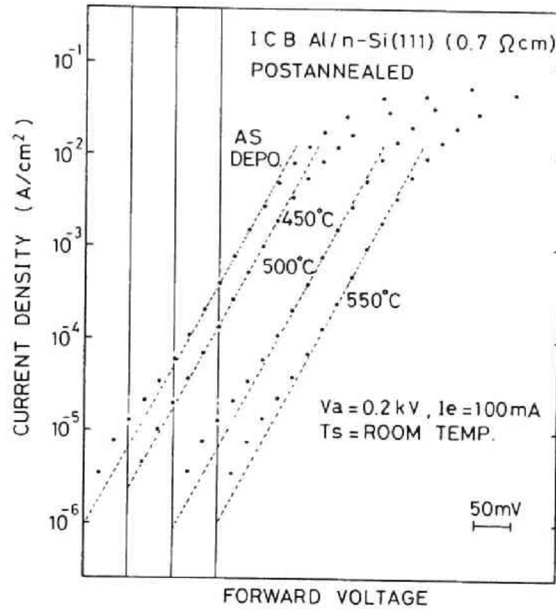


Fig. 4.47
Current density-voltage (J-V) characteristics of ICB Al-Si junctions after annealing at various temperatures for 30 min. Zero voltage of each curve is shifted by 50 mV.

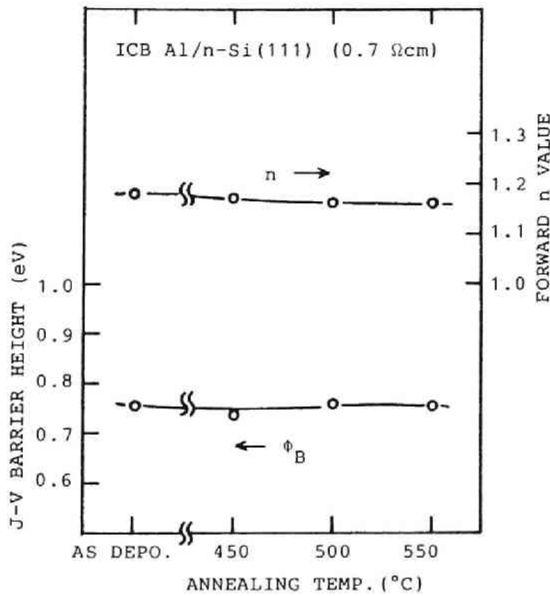


Fig. 4.48
Dependence of the forward n value and the J-V barrier height of the Al-Si junctions on annealing temperature. The ICB Al films were deposited with $V_a$ = 0.2 kV, $I_e$ = 100 mA, and $T_s$ = room temperature.

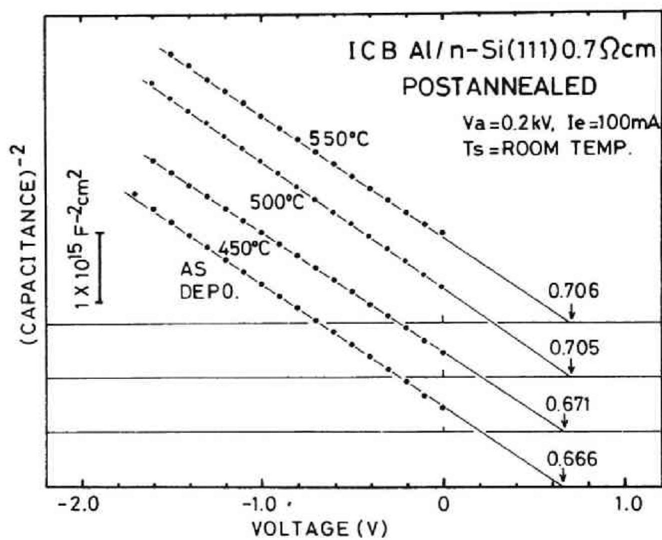


Fig. 4.49
1-MHz capacitance-voltage (C-V) characteristics of ICB Al-Si junctions after annealing at various temperatures for 30 min.

the chemical treatment of the substrate.[79] By using the barrier height $\Phi_j$ by J-V measurement (0.75 eV), the barrier height $\Phi_c$ by C-V measurement (0.92 eV), and the donor concentration $N_D$ in the substrate (7 X $10^{15}$ $cm^{-3}$), we can estimate the thickness a of the boron-doped layer, the boron concentration $N_A$ and the ideal n value.[12] The calculated results are a = 40 nm, $N_A = 1.4 \times 10^{17}$ $cm^{-3}$, and n = 1.14, respectively. As the diffusion constant D of boron at 1000°C is about 1.5 X $10^{-14}$ $cm^2/sec$[80] and the time t of the heat treatment is 600 sec, mean diffusion length $(Dt)^{1/2}$ of the boron is 30 nm, which is in good agreement with a. In addition the surface density of the adsorbed boron ($N_A a = 6 \times 10^{11}$ $cm^{-2}$) is in accordance with the reported value.[78] Thus one can attribute the large barrier height by C-V measurement to the boron-doped surface layer. The rather high value of the measured n value (1.17) can also be due to this surface layer.

### 4.4.10 Electromigration Resistance

Electromigration resistance was measured for 10 μm wide, 1000 μm long strips, 400 nm thick. When they passed current at a density of $10^6$ A/cm² at 250°C, there was no change in resistance after 400 hours, as opposed to sputtered Al films that normally fail at $10^6$ A/cm² after 20 hours. Since electromigration is caused by the atomic movement along the grain boundary or the film surface,[1,2,7] these results clearly reflect the crystalline structure of the epitaxial Al film.

### 4.4.11 Oxidation Resistance

The oxide layer on an Al surface, which increases the contact resistance between metallization layers and degrades the bondability, must be as thin as possible. The oxidation resistance of the epitaxial Al films was examined by exposing them to high-temperature steam. Figure 4.50 shows 0.9-MeV $He^+$ channeling spectra of the epitaxial Al film on Si(111) substrate

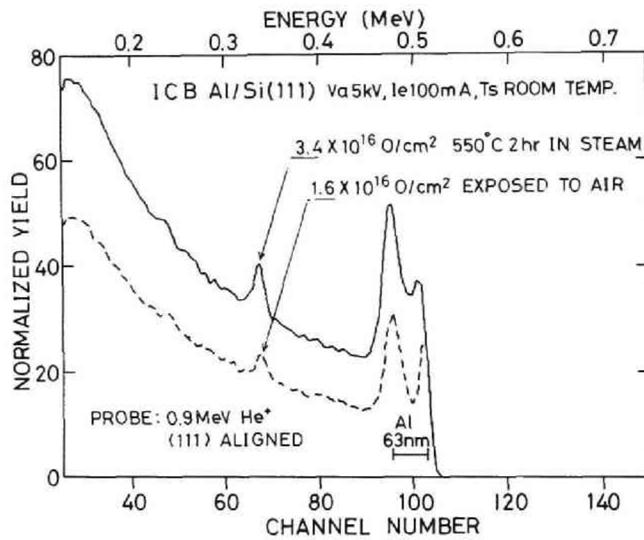


Fig. 4.50
0.9-MeV $He^+$ aligned backscattering spectra of an epitaxial Al film before and after the treatment by steam at 550°C for 2 hours.

before and after the treatment in steam at 550°C for 2 hr. The sample used here had been stored in air for 3 months before the experiment. From these spectra the surface concentrations of oxygen can be calculated, which are 1.6 X $10^{16}$ atoms/$cm^2$ (equivalent to 2.2-nm thick $Al_2O_3$) and 3.4 X $10^{16}$ atoms/$cm^2$ (equivalent to 4.8-nm thick $Al_2O_3$) for the untreated and the treated sample, respectively. The former value is considerably smaller than the reported value, 3.0 - 4.0 nm.[81,82] The oxide thickness increases only by factor 2 after the exposure to steam at 550°C, showing remarkable oxidation resistance of the epitaxial Al film.

#### 4.4.12 Deposition on GaAs(100)

GaAs(100) substrates were chemically treated by a $H_2SO_4$-$H_2O_2$-$H_2O$ mixture and HCl,[83] then to 580°C in vacuum for 10 min just before deposition. The surfaces showed no traces of carbon and oxygen by AES, and RED indicated clear GaAs(100)1X1 pattern. Al was deposited by ICB in the same condition as that for Si substrates. Figure 4.51 shows the 75-keV RED pattern obtained after the sample was once exposed to air. This pattern can be indexed as shown in Fig. 4.52 and the orientation of the film is determined as

Al(100)//GaAs(100), Al[011]//GaAs[010]. (4.21)

This epitaxial relation, which is reasonable having a small latice misfit of (4.05 - 4.00)/4.00 X 100 = 1.3%, is illustrated in Fig. 4.53.

Figure 4.54 shows the 160-keV $H^+$ backscattering / channeling spectra. The minimum yield $\chi_{min}$ is about 49%, which is considerably higher than those of Al films on Si(111) and Si(100). However, it is expected that the epitaxial Al film on GaAs(100) also has the same characteristics as those of the Al films on Si, such as high thermal stability, long electromigration lifetime, high surface flatness, etc. if the crystalline quality of the film is improved.

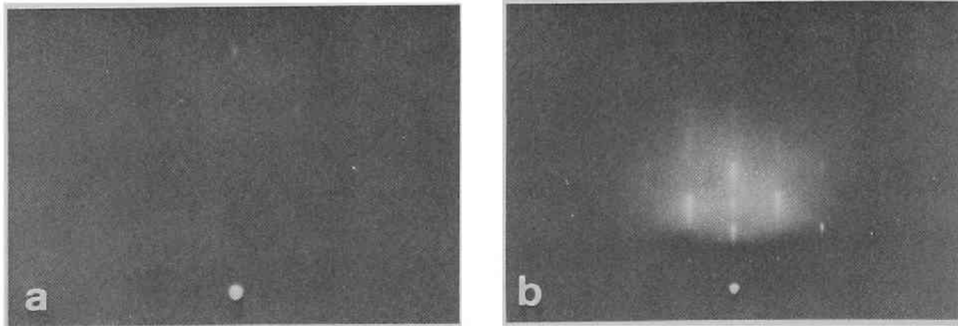


Fig. 4.51
75-keV RED patterns of an Al film deposited on GaAs(100) by ICB ($V_a$ = 0.2 keV, $I_e$ = 100 mA, $T_s$ = room temperature). Incident elctron beam is parallel to GaAs[011] (a), and GaAs[010] (b).

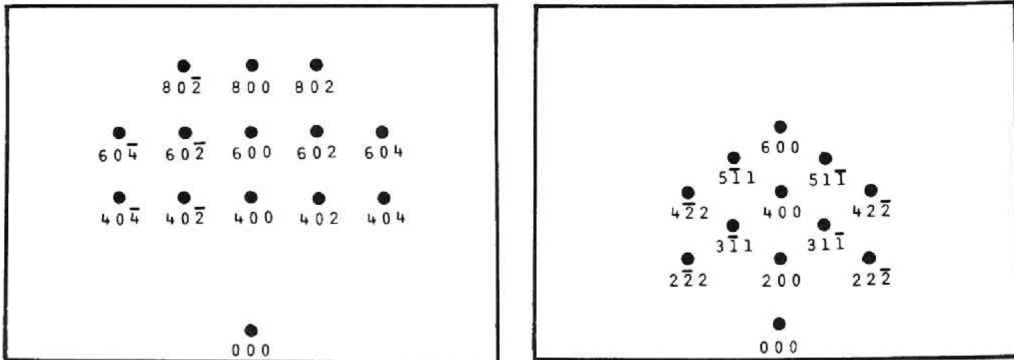


(a) GaAs[011] incidence of the elctron beam.

(b) GaAs[010] incidence of the electron beam.

Fig. 4.52
Indices of the RED patterns in Fig. 4.51.

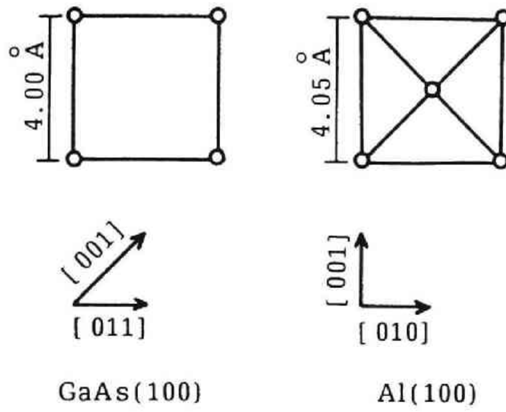


Fig. 4.53
Schematic illustration of the relative orientation of the Al film on GaAs(100) substrate.

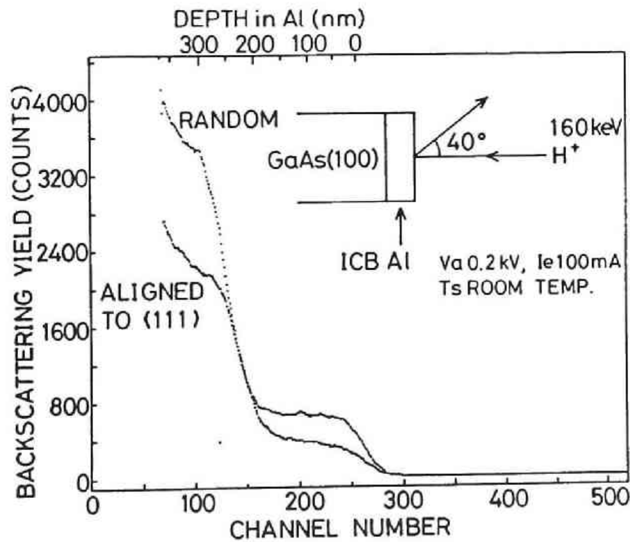


Fig. 4.54
160-keV $H^+$ backscattering spectra of an epitaxial Al film deposited on GaAs(100) substrate by ICB ($V_a$ = 0.2 keV, $I_e$ = 100 mA, $T_s$ = room temperature).

4.4.13 Epitaxy on Insulator Substrates

Al films are used for making interconnections as well as for making contacts to semiconductors. In order to take full advantage of the epitaxial Al film, Al must be grown epitaxially not only on a semiconductor substrate but also on a insulator substrate. In this experiment, sapphire (0001) and an epitaxial $CaF_2$ film on Si(111)[84-86] were used as substrates. Both substrates were heated in vacuum at about 700°C for 10 min, then cooled to room temperature for Al deposition. The acceleration voltage ($V_a$) was 5 kV for the sapphire substrate, and 2.5 kV for the $CaF_2$ substrate. Other deposition conditions were similar to those for Si substrates. Figure 4.55 shows 1.5-MeV $He^+$ channeling spectra of the 135-nm Al film on the sapphire substrate. The minimum yield $\chi_{min}$ is 41% indicating that a fairly good crystal is obtained. The RED patterns of Fig. 4.56 show that Al(111) grows parallel to the substrate surface.

An epitaxial metal-insulator-semiconductor structure was fabricated for the first time only by ICB deposition using $CaF_2$ as an insulator material. A $CaF_2$ film was deposited under a vacuum of $1 \times 10^{-4}$ Pa backed by an oil diffusion pump at a deposition rate of 28 nm/min to thickness of 420 nm. Acceleration voltage ($V_a$) and substrate temperature ($T_s$) were 1 kV and 700°C, respectively. Ion channeling and RED observations showed that the $CaF_2$ film grows with an orientation $CaF_2$(111)//Si(111), $CaF_2[1\bar{1}0]$// Si$[\bar{1}10]$ (so-called type B[84-86] orientation). Figure 4.57 shows the channeling spectra obtained by 2.0-MeV $He^+$ of $CaF_2\langle110\rangle$ incidence, which indicates that an excellent $CaF_2$ crystal with a $\chi_{min}$ of 2.0% grows epitaxially on a Si(111) substrate. Figure 4.58 shows the RED patterns of the epitaxial Al film on the epitaxial $CaF_2$ film. These patterns indicate that a good Al crystal grows with Al(111) parallel to the substrate surface. It seems that further improvement in crystallinity of the Al epitaxial film on sapphire and on epitaxial $CaF_2$ by adjusting the

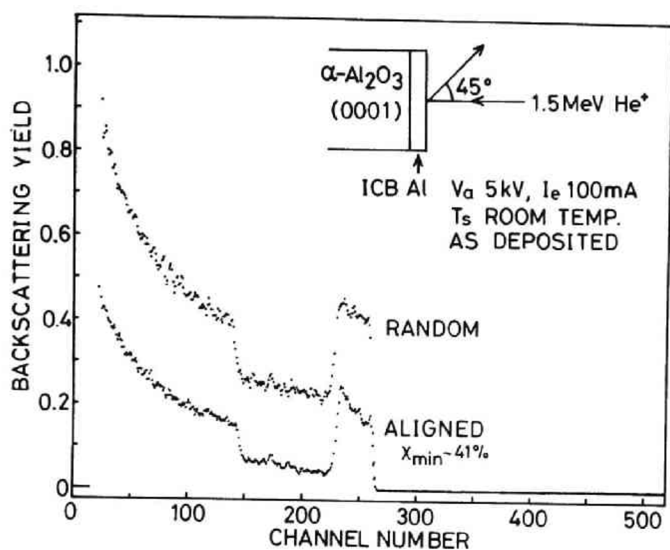


Fig. 4.55
1.5-MeV $He^+$ backscattering spectra of an epitaxial Al film deposited on sapphire (0001) substrate by ICB ($V_a$ = 5 kV, $I_e$ = 100 mA, $T_s$ = room temperature).

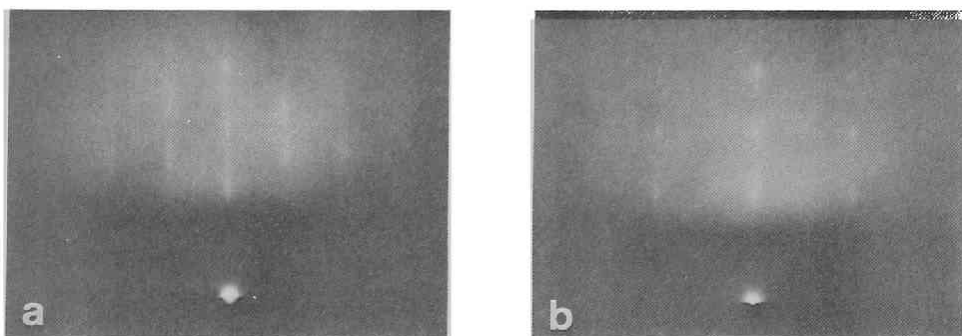


Fig. 4.56
75-keV RED patterns of an epitaxial Al film deposited on sapphire substrate by ICB ($V_a$ = 5 kV, $I_e$ = 100 mA, $T_s$ = room temperature). (b) is obtained by rotating the sample azimuthally by 30° from the condition of (a).

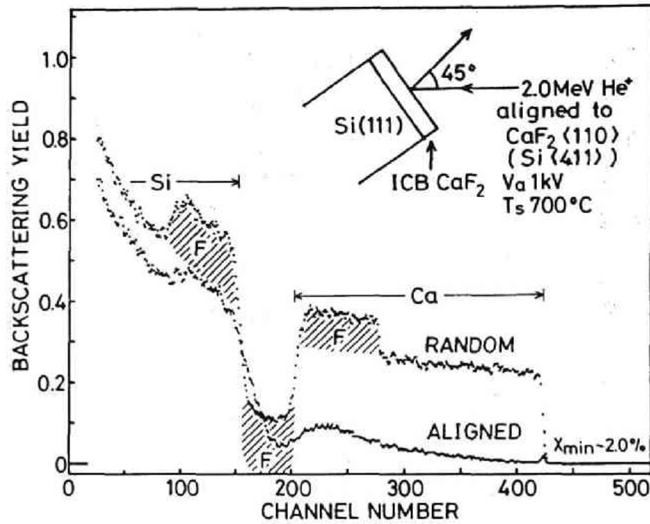


Fig. 4.57
2.0-MeV $He^+$ backscattering spectra of an epitaxial $CaF_2$ film deposited on Si(111) substrate by ICB ($V_a$ = 1 kV, $T_s$ = 700 °C). The $He^+$ beam enters the $CaF_2$<110> direction.

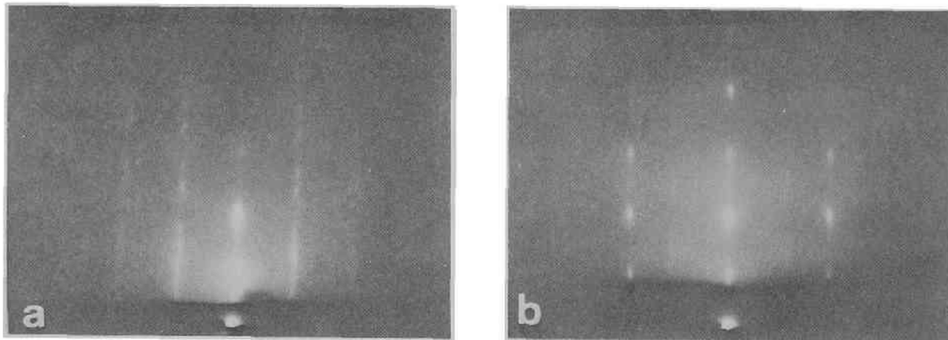


Fig. 4.58
75-keV RED patterns of an epitaxial Al film deposited on the epitaxial $CaF_2$ film on Si(111) shown in Fig. 4.57. Incident electron beam is parallel to Si[$\bar{1}$10] (a), and Si[$\bar{2}$11] (b).

ICB deposition conditions or the substrate preparation method, is sure to realize such characteristics as high thermal stability, high surface flatness, long electromigration lifetime, etc. useful in semiconductor metallization.

## 4.5 Conclusions

Problems in Al metallization of Si devices, such as alloy penetration, electromigration, recrystallization of Si, annealing hillocks, etc. are all related to and sensitive to the film structure and the interface properties, which are not readily controlled by any conventional deposition methods. The ionized cluster beam (ICB) technique permits control over the energy and the ion content of the beam, and thus control over sputter cleaning, formation of nucleation sites and adatom migration. This control can be used to improve the film structure and the interface properties, leading to elimination of the problems in semiconductor metallization. Especially, the epitaxial Al film on a clean Si surface is remarkably stable up to 550°C although pure Al is used. Alloy penetration at the interface, shift of barrier height, degradation of crystalline quality and development of annealing hillocks on the surface were not observed after the heat treatment. Electromigration lifetime 20 times longer than that of the conventional Al film was also obtained. In order to extend this result to Al films on other semiconductor and insulator substrates, epitaxy on GaAs, on sapphire and on epitaxial $CaF_2$ on Si was attempted and realized. The last result indicates the possibility of the three-dimensional devices fully constructed with epitaxial metal, insulator and semiconductor layers by the ICB technique.

References (Chapter 4)

1) D. Pramanik and A.N. Saxena: Solid State Technol. 26(1) (1983) 127-133; 26(3) (1983) 131-138.
2) A.J. Learn, J. Electrochem. Soc. 123 (1976) 894.
3) J.L. Vossen, J. Vac. Sci. Technol. 19 (1981) 761.
4) S.P. Murarka: J. Vac. Sci. Technol. 17(4) (1980) 775-792.
5) A.K. Sinha: J. Vac. Sci. Technol. 19(3) (1981) 778-785.
6) K.N. Tu: J. Vac. Sci. Technol. 19(3) (1981) 766-777.
7) J.M. Poate, K.N. Tu, and J.W. Mayer (eds.), Thin Films -Interdiffusion and Reactions- (Wiley, New York, 1978).
8) S. Vaidya and A.K. Shinha, Thin Solid Films, 75 (1981) 253.
9) M. Hansen, Constitution of Binary Alloys, (McGrow-Hill, New York, 1958).
10) H.F. Wolf: Silicon Semiconductor Data (Pergamon Press, Oxford, 1969) p.154.
11) G.J.van Gurp: J. Appl. Phys. 44(1973) 2040.
12) H.C. Card, in Metal-Semiconductor Contacts, Conf. Ser. No.22, (Institute of Physics, Manchester, England, 1974) 129.
13) P.A. Totta and R.P. Sopher, IBM J. Res. & Dev. 13 (1969) 226.
14) M. Mori, IEEE Trans. Electron Devices ED-30 (1983) 81.
15) T.M. Reith and J.D. Schick, Appl. Phys. Letters 25 (1974) 524.
16) T.M. Reith: Appl. Phys. Letters 28 (1976) 152-154.
17) P. Chaudhari, J. Appl. Phys. 45 (1974) 4339.
18) S.K. Lahiri: J. Appl. Phys. 41 (1970) 3172-3176.
19) S.K. Lahiri: J. Appl. Phys. 46 (1975) 2791-2793.
20) T. Takagi, J. Vac. Sci. Technol. A2 (1984) 382.
21) T. Takagi: Thin Solid Films 92 (1982) 1-17.
22) I. Yamada, H. Takaoka, H. Inokawa, H. Usui, S.C. Cheng, and T. Takagi, Thin Solid Films 92 (1982) 137.

References (Chapter 4)


23) T.Takagi, I.Yamada, and A.Sasaki, Thin Solid Films, 39 (1976) 207.

24) T.Takagi, I.Yamada, and A.Sasaki, Inst. Phys. Conf. Ser. 38 (1978) 142.

25) T. Takagi, I. Yamada, and A. Sasaki: Solid-State Electron Devices 2 (1978) S40-S-48.

26) T.Takagi, I.Yamada, and A.Sasaki, Technical Digest 1976 Int. Electron Devices Meeting, 1976, Washington D.C., p.605.

27) I.Yamada, F.W. Saris, T.Takagi, K.Matsubara, H.Takaoka, and S.Ishiyama, Jpn. J. Appl. Phys. 19 (1980) L181.

28) T.Takagi, I.Yamada, and A.Sasaki, Proc. Int. Conf. on Ion Plating and Allied Techniques, 1977, Edinburgh, (CEP Consultants, Edinburgh, 1977) p.50.

29) T.Takagi, I.Yamada, and A.Sasaki, Thin Solid Films 45 (1977) 569.

30) T.Takagi, K.Inoue, S.Mizugaki, A.Sasaki, and I.Yamada, Vacuum (Shinku) 22 (1979) 267.

31) I. Yamada, T. Takagi, P.R. Younger, and J. Blake: 1985 Los Angeles Tech. Symp. on Opt. & Electro-Opt. Eng., Jan. 20-25, 1985, SPIE Code No.530-11.

32) K.Morimoto, H.Watanabe, and S.Itoh, J. Cryst. Growth 45 (1978) 334.

33) T.Takagi, I.Yamada, and A.Sasaki, in S. Namba (ed.), Ion Implantation in Semiconductors, (Plenum, New York, 1974) p.275.

34) K.Matsubara, I.Yamada, N.Nagao, K.Tominaga, and T.Takagi, Surface Science 86 (1979) 290.

35) T.Takagi, K.Matsubara, and H.Takaoka, J. Appl. Phys. 51 (1980) 5419.

36) K.Matsubara, I.Yamada, H.Takaoka, and T.Takagi, Jpn. J. Appl. Phys. 21, Suppl. 21-1 (1981) 403.

References (Chapter 4)


37) T.Takagi, I.Yamada, and A.Sasaki, J.Vac.Sci.Technol. 12 (1975) 1128.

38) I.Yamada and T.Takagi, Thin Solid Films 80 (1981) 105.

39) T.Takagi, I.Yamada, and A.Sasaki, Proc. 7th Int. Vacuum Congr. and 3rd Int. Conf. on Solid Surfaces, 1977, Vienna, Berger, p.1915.

40) T.Ishida, S.Wako, and S.Ushio, Thin Solid Films 39 (1978) 227.

41) K.Matsubara, H.Takaoka, K.Shigeno, Y.Kuriyama, and T.Takagi, Proc. 6th Symp. on Ion Sources and Ion-Assisted Technology, Tokyo, 1982, (IEEJ, 1982) p.399.

42) T.Koyanagi, K.Matsubara, H.Takaoka, and T.Takagi, Proc. 6th Symp. on Ion Sources and Ion-Assisted Technology, Tokyo, 1982, (IEEJ, 1982) p.409.

43) T.Takagi, K.Matsubara, M.Oura, and T.Koyanagi, Proc. 6th Symp. on Ion Sources and Ion-Assisted Technology, Tokyo, 1982, (IEEJ, 1982) p.391.

44) J.B.Theeten, R.Madar, A.Mircea-Roussel, A.Rocher, and G.Laurence, J.Cryst. Growth 37 (1977) 317.

45) T.Takagi, K.Matsubara, H.Takaoka, and K.Hosono: Proc. Int'l Ion Engineering Congress -ISIAT'83 & IPAT'83-, Kyoto, 1983 (IEEJ, 1983) p.1237.

46) K.Matsubara, T.Horibe, H.Takaoka, and T.Takagi, Proc. 4th Symp. on Ion Sources and Ion Appli. Technology, Tokyo, 1980, (IEEJ, 1980) p.137.

47) K.Mameno, K.Matsubara, and T.Takagi, Proc. 6th Symp. on Ion Sources and Ion-Assisted Technology, Tokyo, 1982, (IEEJ, 1982) p.341.

48) H.Usui, N.Naemura, I.Yamada and T.Takagi, Proc. 6th Symp. on Ion Sources and Ion-Assisted Technology, Tokyo, 1982, (IEEJ, 1982) p.331.

References (Chapter 4)

49) H.Usui, I.Yamada, and T.Takagi: Proc. Int'l Ion Engineering Congress -ISIAT'83 & IPAT'83-, Kyoto, 1983 (IEEJ, 1983) p.1247.

50) H.Takaoka, K.Matsubara, and T.Takagi, Proc. 4th Symp. on Ion Sources and Ion Appl. Technol., Tokyo, 1980, (IEEJ, 1980) p.143.

51) I.Yamada, H.Takaoka, H.Inokawa, H.Usui, S.C.Cheng, and T.Takagi, Thin Solid Films 92 (1982) 137.

52) H. Sato, I. Yamada, and T. Takagi: Proc. 8th Symp. on Ion Sources and Ion-Assisted Technol., Tokyo, 1984 (IEEJ, 1984) pp.267-270.

53) I. Yamada, I. Nagai, M. Horie, and T. Takagi: J. Appl. Phys. 54 (1983) 1583.

54) J. Kudo, T. Morishita, K. Iguchi, M. Koba, and K. Awane: Proc. Int'l Ion Engineering Congress -ISIAT'83 & IPAT'83-, Kyoto, 1983 (IEEJ, 1983) p.1193.

55) I. Yamada, C.J. Palmstrom, E. Kennedy, J.W. Mayer, H. Inokawa, and T. Takagi: 1984 Material Research Society Meeting, Boston, Nov. 26-30, 1984.

56) Y.Minowa and K.Yamagishi, 1983 Int. Conf. on Electron, Ion, and Photon Beam, Los Angeles, Calif., June, 1983.

57) I. Yamada: Proc. Int'l Ion Engineering Congress -ISIAT'83 & IPAT'83-, Kyoto, 1983 (IEEJ, 1983) p.1177.

58) P.P. Wegener (ed.): Molecular Beams and Low Density Gasdynamics (Marcel Dekker, Inc., New York, 1974).

59) J. Frenkel, Kinetic Theory of Liquids (Dover, New York, 1955).

60) G.D. Stein, in: Proc Int'l Ion Engineering Congress ISIAT'83 & IPAT'83, Kyoto (1983) p. 1165.

61) R.C. Tolman, J. Chem. Phys. 17 (1949) 333.

62) C.J. Smithells (ed.), Metal Reference Book, 5th ed. (Butterworths, London, 1976) p. 944.

63) R.J. Meyer (ed.), Gmelins Handbuch der Anorganischen Chemie, 8th ed. System Nr. 1 (Verlag Chemie, Berlin, 1926).

64) H.Usui, H.Takaoka, I.Yamada, and T.Takagi, Proc. 4th Symp. on Ion Sources and Ion-Assisted Technology, Tokyo, 1981 (IEEJ, 1981) p.175.

65) I.Yamada, G.D.Stein, H.Usui, and T.Takagi, Proc. 6th Symp. on Ion-Assisted Technology, Tokyo, 1982 (IEEJ, 1982) p.47.

66) D.M. Cox, E.A. Rohlfing, D. Trevor and A. Kaldor: J. Vac. Sci. Technol. A2 (1984) 812-813.

67) F. Bottiglioui, J. Coutant and M. Fois: Phys. Rev. A, 6 (1972) 1830.

68) T. Takagi, I. Yamada, and A. Sasaki: Inst. Phys. Conf. Ser. No. 38, (1978) Chapt. 5, pp.229-235.

69) H.H. Berger: J. Electrochem. Soc. 119 (1972) 507-514.

70) M. Tabe, K. Arai, and H. Nakamura, Jpn. J. Appl. Phys. 20 (1981) 703.

71) B. Lewis and J.C. Anderson: Nucleation and Growth of Thin Films (Academic Press, New York, 1978) p.31.

72) C.C. Chang, in: Characterization of Solid Surfaces, Eds. P.F. Kane and B. Larrabee (Plenum, New York, 1974) p. 509.

73) R. Levi-Seti, T.R. Fox, and K. Lam, Electrochem. Soc. Inc. Spring Meeting, Montreal, Canada, May 9-14, 1982, Abstract No. 282.

74) I. Yamada, H. Inokawa, H. Usui, and T. Takagi: Proc. 4th Symp. on Ion Sources and Ion Application Technol. (IEEJ, 1980) pp.69-72.

75) W.K. Chu, J.W. Mayer, and M.A. Nicolet, Backscattering Spectrometry (Academic Press, New York, 1978) pp. 223-275.

76) G. Hass and J.E. Waylonis, J. Opt. Soc. Am. 51 (1961) 719.

References (Chapter 4)

77) S.M. Sze, Physics of Semiconductor Devices, (Wiley, New York, 1981) 279.

78) F.G. Allen, T.M. Buck, and J.T. Law, J. Appl. Phys. 31 (1960) 979.

79) R.C. Henderson J. Elctrochem. Soc. 119 (1972) 772.

80) R.N. Ghoshtagore, Solid State Electron. 15 (1972) 1113.

81) R.P. Madden, L.R. Canfield, and H. Hass: J. Opt. Soc. Am. 53 (1963) 620.

82) L.R. Canfield, G. Hass, and J.E. Waylonis: Appl. Opt. 5 (1966) 45.

83) A.Y. Cho, Thin Solid Films 100 (1983) 291.

84) T. Asano and H. Ishiwara: Appl. Phys. Letters 42 (1983) 517-519.

85) T. Asano, H. Ishiwara and N. Kaifu: Jpn. J. Appl. Phys. 22 (1983) 1474-1481.

86) J.M. Phillips and C.J. Yashinovitz: J. Vac. Sci. Technol. A2 (1984) 415-417.

87) Only a few studies of Al epitaxial growth on Si have been performed and little is known about the properties of the epitaxial Al films.
J.J. Lander and J. Morrison: Surf. Sci. 2 (1964) 553-565.
M. Ichikawa and K. Hayakawa: Jpn. J. Appl. Phys. 21 (1982) 154-163.

Chapter 5

# CONCLUSIONS

In this thesis, application of ion beams to semiconductor metallization was discussed with two purposes. One was to realize a new type of metallization, which had not been available in conventional film deposition techniques, by utilizing the properties of the charged particle itself and the other was to solve the problems in semiconductor metallization by improving the film structure and the interface properties through the effects of ion irradiation.

In Chapter 2, fundamental phenomena included in ion-surface interactions were discussed in terms of several characteristic energies. Special interest was invoked around the energy E*, where lattice defects begin to appear, because suitable numbers of defects may serve as nucleation sites for film growth if the ion energy does not exceed E* by too much. Even at energy less than E*, there may still exist sputtering of weakly-bonded atoms or molecules on surface, such as adsorbed impurities and deposited material itself. It was also pointed out that, without acceleration, ionization of material by itself can enhance chemical reactions. These considerations on ion-surface interactions determined the experimental conditions in the following chapters, and revealed what sort of improvements can be expected in semiconductor metallization using ion beams. These improvements include lowering of processing temperature, formation of metastable materials, reduction of film stress, increase of adhesion strength of deposited film, change in morphology, densification of deposited film and improvement of crystallinity,

purity, oxidation resistance, etc.

In Chapter 3, semiconductor metallization by mass-analyzed atomic ion beams was described. By using low-energy Pd ion beam deposition on Si, continuous Pd films were obtained with resistivity of the same order as that of bulk material, yet the films were as thin as a few nanometers in thickness. Selective deposition onto conductors was also realized utilizing charge-up of insulators. By high-dose Pd ion implantation into Si substrates, continuous conductive layers whose sheet resistance is on the order of a few ohms were formed under the surface while preserving the crystallinity of surface Si. The conditions to obtain low-resistivity buried layers were determined theoretically and experimentally. It was concluded that the atomic ion beam can be effectively utilized to achieve a new type of metallizaion which cannot be realized by conventional methods.

In Chapter 4, Al metallization by ionized cluster beam (ICB) was discussed. In ICB deposition, the kinetic energy and the electric charge of the ionized cluster have effects on the fundamental processes in film growth through sputter cleaning, formation of nucleation sites, enhancement of adatom migration, etc. and these effects allow realization of epitaxial film growth at low substrate temperature. Even though pure Al was used, epitaxial Al film on Si substrate was found to be stable morphologically, crystallographically and electrically up to 550°C, and remarkably relieved problems in Al metallization, such as alloy penetration, hillock growth, electromigration, step coverage, etc. It was concluded that the properties of a film can be drastically improved by changing the film structure through the use of ion beams, even if the material composition remains the same.

## APPENDIX

### A.1 Derivation of eq. (3.17)

The derivation of eq. (3.17) is mainly based on ref. 1, except that ion trajectories and ionic potential are considered, and that normalized variables $\xi$, $\eta$ and $\psi$, and a special parameter k are introduced. The equation of motion is written as

$$\frac{d^2\mathbf{r}}{dt^2} = \frac{e}{m}\, grad\ \phi \qquad (A.1)$$

where $\phi$ is the ionic potential (ie. negative of the electric potential) whose origin is set so that $\phi$ is equal to ion energy. In a rotationally symmetric cylindrical coordinate system, eq. (A.1) becomes

$$\frac{d^2 r}{dt^2} = \frac{e}{m}\frac{\partial \phi}{\partial r} \qquad (A.2)$$

$$\frac{d^2 z}{dt^2} = \frac{e}{m}\frac{\partial \phi}{\partial z} \qquad (A.3)$$

Taking account of Poisson's equation

$$\frac{1}{r}\frac{\partial}{\partial r}\left(r\frac{\partial \phi}{\partial r}\right) + \frac{\partial^2 \phi}{\partial z^2} = \frac{\rho}{\varepsilon_0} \qquad (A.4)$$

$\phi(r,z)$ can be expressed by power series in r, that is

$$\phi(r,z) = \Phi(z) - \left(\frac{r}{2}\right)^2\left(\Phi''(z) - \frac{\rho}{\varepsilon_0}\right) + \sum_{n=1}^{\infty}(-1)^{n+1}\frac{1}{[(n+1)!]^2}\left(\frac{r}{2}\right)^{2n+2}\Phi^{(2n+2)}(z) \qquad (A.5)$$

where $\Phi(z)$ is the ionic potential on the z axis, ie. $\Phi(z) = \Phi(0,z)$, $\Phi''(z)$ denotes the second derivative of $\Phi(z)$, and $\Phi^{(2n+2)}(z)$ denotes the (2n+2)th derivative of $\Phi(z)$. Neglecting

terms of higher degree than the second in r (paraxial approximation), eqs. (A.2) and (A.3) become respectively

$$\ddot{r} = -\frac{e}{m}\frac{r}{2}\left(\Phi''(z) - \frac{\rho}{\varepsilon_0}\right) \tag{A.6}$$

$$\ddot{z} = \frac{e}{m}\Phi'(z) \tag{A.7}$$

where $\ddot{r}$ and $\ddot{z}$ are the second derivatives of r and z with respect to time. In order to eliminate the derivatives with respect to time, the following relation is used.

$$\dot{r} = \dot{z}\, r' \tag{A.8}$$

where $\dot{r}$ and r' are the derivatives of r with respect to t and z, and thus we obtain

$$\ddot{r} = \frac{d}{dt}(\dot{z}\, r') = \ddot{z}\, r' + \dot{z}^2 r'' \tag{A.9}$$

Using eq. (A.7), $\dot{z}^2$ is expressed as

$$\begin{aligned} \dot{z}^2 &= \int 2\,\ddot{z}\,\dot{z}\,dt \\ &= \int 2\frac{e}{m}\Phi'(z)\,dz \\ &= \frac{2e}{m}\Phi(z) \end{aligned} \tag{A.10}$$

Substituting eqs. (A.7) and (A.10) into (A.9) yields

$$\ddot{r} = \frac{e}{m}\Phi' r' + \frac{2e}{m}\Phi r'' \tag{A.11}$$

Combining eqs (A.6) and (A.11) we obtain the ray equation.

$$r'' + \frac{\Phi'}{2\Phi} r' + \frac{\Phi'' - \rho/\varepsilon_0}{4\Phi} r = 0 \tag{A.12}$$

Let us consider that an ion beam whose initial radius, current density and energy are $R_O$, $J_O$ and $\Phi_O$, respectively, changes its radius during transport through distance d. Strictly speaking, ionic potential $\Phi$ and charge density $\rho$ are not constant in a cross section of the beam but we assume their average values. So the charge density $\rho$ is given by

$$\rho = \frac{J}{v} = J_0 \left(\frac{R_0}{R}\right)^2 \left(\frac{m}{2e\Phi}\right)^{1/2} \qquad (A.13)$$

J: current density of the beam

v: velocity of the beam

Substituting eq. (A.13) into (A.12) and considering the outermost ion trajectory, on the assumption that the beam is laminar, ie. there is no crossing of the trajectories, we obtain the beam radius equation.

$$R'' + \frac{\Phi'}{2\Phi} R' + \frac{\Phi''}{4\Phi} R - \frac{J_0}{4\varepsilon_0} \left(\frac{m}{2e}\right)^{1/2} \frac{R_0^2}{\Phi^{3/2}} \frac{1}{R} = 0 \qquad (A.14)$$

We introduce dimensionless variables $\xi$, $\eta$ and $\psi$, defined by

$$\xi = R/R_0, \quad \eta = z/d, \quad \psi = \Phi/\Phi_0 \qquad (A.15)$$

and a space charge effect parameter kd (see Note in section 3.2.1), defined by

$$kd = \frac{3}{2} \left(\frac{J_0}{\varepsilon_0}\right)^{1/2} \left(\frac{m}{2e}\right)^{1/4} \Phi_0^{-3/4}\, d \qquad (A.16)$$

Then eq. (A.14) becomes

$$\frac{d^2\xi}{d\eta^2} + \frac{1}{2\psi}\frac{d\psi}{d\eta}\frac{d\xi}{d\eta} + \frac{1}{4\psi}\frac{d^2\psi}{d\eta^2}\xi - \left(\frac{kd}{3}\right)^2 \frac{1}{\psi^{3/2}}\frac{1}{\xi} = 0 \qquad (3.17)$$

### A.2 Derivation of eq. (3.3)

Let us consider the case that a parallel beam whose initial radius is $R_0$ and energy is $\Phi_0$ enters a equipotential space and travels a distance d. In eq. (3.17) this condition is written as

$$\psi = 1, \quad \frac{d\psi}{d\eta} = \frac{d^2\psi}{d\eta^2} = 0 \qquad (A.17)$$

$$\xi = 1, \quad \frac{d\xi}{d\eta} = 0 \qquad \text{at} \quad \eta = 0 \qquad (A.18)$$

Then eq. (3.17) becomes

$$\frac{d^2\xi}{d\eta^2} = \left(\frac{kd}{3}\right)^2 \frac{1}{\xi} \qquad (A.19)$$

Multiplying eq. (A.19) by $2(d\xi/d\eta)$ and integrating the equation gives

$$\left(\frac{d\xi}{d\eta}\right)^2 = 2\left(\frac{kd}{3}\right)^2 \log \xi \qquad (A.20)$$

Integrating a square root of this equation with respect to $\eta$ from zero to unity yields

$$kd = \frac{3}{\sqrt{2}} \int_0^1 \frac{1}{\sqrt{\log \xi}} \frac{d\xi}{d\eta} d\eta$$

$$= 3\sqrt{2} \int_0^{\sqrt{\log(R/R_0)}} e^{w^2} dw \qquad (3.3)$$

This is the relation between beam radius R and transport distance d.

### A.3 Derivation of eqs. (3.6) - (3.15)

Under a condition shown in Fig. 3.4 (a), trajectories of ions are all parallel to each other and normal to the plates. Therefore substituting $r''=r'=0$ into eq. (A.12) gives

$$\Phi'' = \frac{\rho}{\varepsilon_0} = \frac{J_0}{\varepsilon_0}\left(\frac{m}{2e\Phi}\right)^{1/2} \qquad (A.21)$$

Multiplying eq. (A.21) by $2\Phi'$ and integrating the equation yields

$$\Phi' = \pm\frac{4}{3}k\,(u + C_1)^{1/2}\,\Phi_0 \qquad (A.22)$$

where $C_1$ is an integration constant and u is the relative velocity of an ion defined by

$$u = (\Phi/\Phi_0)^{1/2} \qquad (3.8)$$

By introducing a new variable w defined by

$$w = (u + C_1)^{1/2} \qquad (3.7)$$

we can integrate eq. (A.22) analytically to yield

$$w^3 - 3C_1 w = \pm k z + C_2 \qquad (A.23)$$

where $C_2$ is another integration constant. In mode 1, the potential $\Phi$ decreases monotonically from $\Phi_0$ to $\Phi_1$, ie.

$$\Phi' \leq 0 \quad \text{for} \quad 0 \leq z \leq d \qquad (A.24)$$

and

$$w^3 - 3C_1 w = -kz + C_2 \quad \text{for} \quad 0 \leq z \leq d \qquad (3.6)$$

Boundary condition is

$$u = 1 \quad \text{at} \quad z = 0 \qquad (A.25)$$

$$u = u_1 \quad \text{at} \quad z = d \tag{A.26}$$

where $u_1$ is the ratio of the final and the initial velocities, defined by

$$u_1 = (\Phi_1/\Phi_0)^{1/2} \tag{3.10}$$

Substituting eqs. (A.25) and (A.26) into (3.6) yields

$$C_2 = (1 + C_1)^{1/2}(1 - 2C_1) \tag{3.11}$$

$$-kd + C_2 = (u_1 + C_1)^{1/2}(u_1 - 2C_1) \tag{A.27}$$

Eliminating $C_2$ from eqs. (3.11) and (A.27) gives

$$kd = (1 + C_1)^{1/2}(1 - 2C_1) - (u_1 + C_1)^{1/2}(u_1 - 2C_1) \tag{3.9}$$

The following can be derived from eq. (3.9) for all $u_1$ between zero and unity

$$\frac{d}{dC_1}(kd) < 0 \quad \text{for} \quad -u_1 \leq C_1 < \infty \tag{A.28}$$

$$kd \rightarrow 0 \quad \text{as} \quad C_1 \rightarrow \infty \tag{A.29}$$

In mode 2, the potential $\Phi$ decreases first, reaches a minimum at $z=z_2$ and increases again, ie.

$$\Phi' \leq 0 \quad \text{for} \quad 0 \leq z \leq z_2 \tag{A.30}$$

$$\Phi' \geq 0 \quad \text{for} \quad z_2 \leq z < d \tag{A.31}$$

and

$$w^3 - 3C_{11}w = -kz + C_{21} \qquad \text{for} \qquad 0 \le z \le z_2 \tag{A.32}$$

$$w^3 - 3C_{12}w = \phantom{-}kz + C_{22} \qquad \text{for} \qquad z_2 \le z \le d \tag{A.33}$$

Boundary condition is

$$u = 1 \qquad \text{at} \qquad z = 0 \tag{A.34}$$

$$u = u_1 \qquad \text{at} \qquad z = d \tag{A.35}$$

$$\Phi' = 0 \qquad \text{at} \qquad z = z_2 \tag{A.36}$$

Combining eqs. (A.22) and (A.36) we get

$$w = (u + C_{11})^{1/2} = (u + C_{12})^{1/2} = 0 \qquad \text{at} \qquad z = z_2 \tag{A.37}$$

Therefore

$$C_{11} = C_{12} \equiv C_1 \tag{A.38}$$

$$u = -C_1 \qquad \text{at} \qquad z = z_2 \tag{A.39}$$

Substituting w=0 into eqs. (A.32) and (A.33) gives

$$-kz_2 + C_{21} = kz_2 + C_{22} = 0 \tag{A.40}$$

Therefore

$$C_{21} = -C_{22} \equiv C_2 \tag{A.41}$$

$$z_2 = C_2 / k \tag{3.15}$$

Thus eqs. (A.32) and (A.33) become respectively

$$w^3 - 3C_1 w = -kz + C_2 \qquad \text{for} \quad 0 \leq z \leq z_2 \tag{3.12}$$

$$w^3 - 3C_1 w = kz - C_2 \qquad \text{for} \quad z_2 \leq z \leq d \tag{3.13}$$

By boundary condition of eqs. (A.34) and (A.35), eqs. (3.12) and (3.13) are changed into

$$C_2 = (1 + C_1)^{1/2}(1 - 2C_1) \tag{A.42}$$

$$kd - C_2 = (u_1 + C_1)^{1/2}(u_1 - 2C_1) \tag{A.43}$$

Equations (A.42) and (A.43) are added to yield

$$kd = (1 + C_1)^{1/2}(1 - 2C_1) + (u_1 + C_1)^{1/2}(u_1 - 2C_1) \tag{3.14}$$

It can be derived that kd becomes a maximum at $C_1 = -u_1/(1+u_1)$, and that $C_1$ is bounded by $-u_1$ and zero because ion energy is always positive and real.

## Reference


1) K. Ura: Denshi Kohgaku (Electron Optics) (Kyoritsu Shuppan Co. Ltd., Tokyo, 1979) p.89 [in Japanese].

LIST OF PAPERS

1. Y.Hirose, H.Inokawa, I.Yamada and T.Takagi,
"Formation of Pb Films by Ionized Cluster Beam Deposition"
The Spring Meeting of JSAP, Paper No.1p-B-5, p.275, Yamanashi Univ., April 1-4, 1980.

2. I.Yamada, H.Inokawa, H.Usui and T.Takagi,
"Design Factors of Vapourized-Metal-Cluster Ion Source"
Proc. of the 4th Symp. on Ion Sources and Ion Application Technology, pp. 69-72, Tokyo, June 24-26, 1980 (IEEJ, Tokyo).

3. I.Yamada, Y.Hirose, H.Inokawa and T.Takagi,
"Pb and PbO Films Prepared by ICB Deposition"
Proc. of the 4th Symp. on Ion Sources and Ion Application Technology, pp. 141-142, Tokyo, June 24-26, 1980 (IEEJ, Tokyo).

4. S.C. Cheng, H.Inokawa I.Yamada and T.Takagi,
"Low Energy Ion Beam Transportation for Film Deposition"
The Spring Meeting of JSAP, Paper No.29p-X-13, p.340, Hosei Univ., March 29 - April 1, 1981.

5. I.Yamada, H.Takaoka, H.Inokawa, H.Usui, S.C. Cheng and T.Takagi,
"Vapourized-Metal Cluster Formation and Effect of Kinetic Energy of Ionized Clusters on Film Formation"
Proc. of the 5th Symposium on Ion Sources and Ion-Assisted Technology, and Proc. of International Workshop by Professional Group on Ion-Based Techniques for Film Formation, pp.449-458, Tokyo and Kyoto, June 1-5, 1981 (The Research Group of Ion Engineering, Kyoto Univ.).

6. H.Inokawa, M.Itoh, I.Yamada and T.Takagi,
"Effect of Acceleration Voltage on Grain Size of Pb Films Deposited by ICB"
The Spring Meeting of JSAP, Paper No.3p-D-8, p.400, Tokyo Rika Univ., April 1-4, 1982.

List of Papers (Continued)

7. H.Inokawa, K.Fukushima, I.Yamada and T.Takagi,
Characteristics of Al Films Formed by Ionized Cluster Beam Deposition"
Proc. 6th Symp. on Ion Sources and Ion-Assisted Technol. pp.355-358, Tokyo, July 7-9, 1982 (The Research Group of Ion Engineering, Kyoto Univ.)

8. I.Yamada, H.Takaoka, H.Inokawa, H.Usui, S.C.Cheng and T.Takagi,
"Vaporized-Metal Cluster Formation and Effect of Kinetic Energy of Ionized Cluster on Film Formation"
Thin Solid Films, Vol. 92, 1982, pp.137-146.

9. H.Inokawa, I.Yamada and T.Takagi,
"Film Formation Mechanism by Ionized Cluster Beam Deposition"
The Fall Meeting of JSAP, Paper No. 29a-L-2, p.222, Kyusyu Tech. Univ., Sept. 28-30, 1982.

10. K.Fukushima, H.Inokawa, I.Yamada and T.Takagi,
"Characteristics of Al Films Deposited by Ionized Cluster Beam Deposition"
The Fall Meeting of JSAP, Paper No. 29p-R-5, p.451, Kyusyu Tech. Univ., Sept. 28-30, 1982

11. I.Yamada, H.Inokawa, K.Fukushima and T.Takagi
"Semiconductor Metallization by Ion Beams"
Paper of the Professional Group of Electronic Material of IEEJ, Paper No. EFM-82-20, pp.51-62, Electrotechnical Lab., Nov. 17, 1982.

12. H.Inokawa, I.Yamada and T.Takagi
"Pd-Si Films Formed by Mass-Analyzed Ion Beams"
The Joint Meeting of Institutes Associating with Electrical Engineers in Western Region, Paper No. G177, Kyoto Univ., Dec.4-5, 1982.

13. K.Fukushima, H.Inokawa, I.Yamada and T.Takagi
"Characteristics of Al Films Deposited by Ionized Cluster Beam"
The Joint Meeting of Institutes Associating with Electrical Engineers in Western Region, Paper No. G267, Kyoto Univ., Dec.4-5, 1982.

List of Papers (Continued)

14. T.Takagi, I.Yamada, K.Fukushima and H.Inokawa
"Semiconductor Metallization by Ion Beam Processing Technology"
The Third Meeting of the Professional Group of "Nanometer Structure Electronics" Supported with the Grand-in-Aid for Scientific Research of the Ministry of Education, Tokyo, Feb. 1, 1983, pp.9-12.

15. H.Inokawa, J.Matsuo, I.Yamada and T.Takagi,
"Buried Layer Formation by Pd Ion Implantation in Si"
The Spring Meeting of JSAP, Paper No.6a-U-9, p.279, Chiba Univ., April 4-7, 1983.

16. H.Inokawa, J.Matsuo, I.Yamada and T.Takagi,
"Very Thin Pd Films Formed by Mass-Analyzed Ion Beam"
The Spring Meeting of JSAP, Paper No.6a-U-11, p.279, Chiba Univ., April 4-7, 1983.

17 K.Fukushima, H.Inokawa, I.Yamada and T.Takagi,
"Application to Interconnection of Al Films Deposited by Ionized Cluster Beam "
The Spring Meeting of JSAP, Paper No.6a-O-1, p.536, Chiba Univ., April 4-7, 1983

18. K.Fukushima, H.Inokawa, I.Yamada and T.Takagi,
"VLSI Applications of Al Films Deposited by Ionized Cluster Beam Deposition"
Proc. Int'l. Ion Eng. Congr. -ISIAT'83 & IPAT'83-, pp.1227-1232. Kyoto, Sept. 12-16, 1983 (IEEJ, Tokyo).

19 H.Inokawa, I.Yamada and T.Takagi,
"Formation of Very Thin Films and Buried Conductive Layers by Mass-Analyzed Ion Beams"
Proc. Int'l. Ion Eng. Congr. -ISIAT'83 & IPAT'83-, pp.1765-1772, Kyoto, Sept. 12-16, 1983 (IEEJ, Tokyo).

20 K.Fukushima, H.Inokawa, I.Yamada and T.Takagi
"Application to Interconnection of Al Films Deposited by Ionized Cluster Beam (II)"
The Fall Meeting of JSAP, Paper No. 25p-N-9, p.414, Tohoku Univ., Sept. 25-28, 1983.

21. H.Inokawa, J.Matsuo, N.Maeda, I.Yamada and T.Takagi,
"Characteristics of Buried Conductive Layer by Pd Ion Implantation into Si"
The Fall Meeting of JSAP, Paper No. 28a-T-9, p.246, Tohoku Univ., Sept. 25-28, 1983.

List of Papers (Continued)

22. H.Inokawa, N.Maeda, J.Matsuo, I.Yamada and T.Takagi, "Selective Deposition by Low Energy Mass-Analyzed Ion Beam" The Fall Meeting of JSAP, Paper No. 25p-U-16, p.255, Tohoku Univ., Sept. 25-28, 1983.

23. I.Yamada, H.Inokawa, J.Matsuo and T.Takagi "Formation of Very Thin Films and Buried Conductive Layers by Pd Ion Irradiation onto Si Substrate" The 6th Meeting of the Professional Group of "Nanometer Structure Electronics" Supported with the Grand-in-Aid for Scientific Research of the Ministry of Education, Kyoto, Dec. 13-14, 1983, pp.37-42.

24. I.Yamada, H.Inokawa, N.Maeda, Q.Fuquang, J.Matsuo and T.Takagi "Bombarding Effect on Si Surface by Low Energy Ion Beam" The 6th Meeting of the Professional Group of "Nanometer Structure Electronics" Supported with the Grand-in-Aid for Scientific Research of the Ministry of Education, Kyoto, Dec. 13-14, 1983, pp.43-46.

25. H.Inokawa, J.Matsuo, I.Yamada and T.Takagi "Characteristic Energy Dependence in Buried Conductive Layer Formation by Pd Ion Implantation" The Spring Meeting of JSAP, Paper No. 30a-W-9, p.264, Meiji Univ., March 29 - April 2, 1984.

26. N.Maeda, Q.Fuguang, H.Inokawa, J.Matsuo, I.Yamada and T.Takagi, "Bombarding Effect on Si by Low Energy Ion Beam" The Spring Meeting of JSAP, Paper No. 30a-W-1, p.261, Meiji Univ., March 29 - April 2, 1984.

27. I.Yamada, H.Inokawa T.Fujino and T.Takagi, "Al Epitaxial Growth on Si by Ionized Cluster Beam" The Spring Meeting of JSAP, Paper No. 30a-X-9, p.296, Meiji Univ., March 29 - April 2, 1984.

28. I.Yamada, H.Inokawa and T.Takagi "Ion Beam Deposition" in: International Symposium on Nanometer Structure Electronics, eds. Y. Yamamura, T. Fujisawa and S. Namba (Ohmsha, Ltd., Tokyo, 1985) pp. 113-120.

List of Papers (Continued)


29. H.Inokawa, T.Fujino, I.Yamada and T.Takagi,
"Low Temperature Epitaxy of Al on Si by Ionized-Cluster-Beam"
Proc. 8th Symp. on Ion Sources and Ion-Assisted Technol. pp.221-226, Tokyo, June 4-6, 1984 (The Research Group of Ion Engineering, Kyoto Univ.).

30. I.Yamada, H.Inokawa, K.Fukushima and T.Takagi,
"Al Metallization by Ionized Cluster Beam Deposition and Epitaxy"
Ion Beam Modification of Materials, Cornell, N.Y. July 16-20, 1984.
Nucl. Instr. Meth. B7/8 (1985) 900-905.

31. I.Yamada, H.Inokawa and T.Takagi,
"Film Deposition and Buried Layer Formation by Mass-Analyzed Ion Beams"
Nucl. Instr. Meth. B6 (1985) 439-446.

32. I.Yamada, H.Inokawa and T.Takagi,
"Aluminium Epitaxy on Si(111) and Si(100) using an Ionized Cluster Beam"
6th International Conference on Thin Films, Stockholm, Sweden Aug. 13-17, 1984.
Thin Solid Films 124 (1985) to be published.

33. T.Fujino, H.Inokawa, I.Yamada and T.Takagi,
"Low Temperature Formation of Aluminium Oxide Films by Reactive Ionized Cluster Beam Deposition
The Fall Meeting of JSAP, Paper No. 14p-U-2, p.287, Okayama Univ., Oct. 12-15, 1984.

34. H.Inokawa, T.Fujino, I.Yamada and T.Takagi
"Thermal Stability of Epitaxial Al Film-Si Substrate Interface Fabricated by ICB Deposition"
The Fall Meeting of JSAP, Paper No. 13p-C-13, p.453, Okayama Univ., Oct. 12-15, 1984.

35. I.Yamada, H.Inokawa and T.Takagi,
"Epitaxial Growth of Al on Si(111) and Si(100) by Ionized-Cluster Beam"
J. Appl. Phys, Vol. 56, No. 10, Nov. 15, 1984, pp.2746-2750.

List of Papers (Continued)

36. I.Yamada, C.J.Palmström, E.Kennedy, J.W.Mayer, H.Inokawa and T.Takagi,
"Epitaxy of Aluminium Films on Semiconductors by Ionized Cluster Beam"
1984 Material Research Society Meeting, Boston, Nov. 26-30, 1984.

37. H.Inokawa, I.Yamada and T.Takagi
"Observation of Initial Stage of Al Epitaxial Growth on Si(111) by Ionized Cluster Beam Deposition"
Jpn. J. Appl. Phys. 24 (1985) L173-L174.

38. I. Yamada, H. Inokawa and T. Takagi,
"Characteristics of Epitaxial Al Films on Semiconductor and Insulator Substrates"
Paper of Technical Group on Semiconductors and Semiconductor Devices, IECEJ, Paper No. SSD84-149, pp.7-14, Kyoto Univ., March 11, 1985.

39. H. Inokawa, I. Yamada and T. Takagi,
"Epitaxial Al/GaAs/GaAs(100) Structure Fabricated by ICB Technique"
The Spring Meeting of JSAP, Paper No. 31p-K-4, Aoyama Gakuin Univ., March 29 - April 1, 1985.

40. H. Inokawa, T. Fujino, I. Yamada and T. Takagi,
Radiation Effect of Ionized Clusters on Al/Si Epitaxial Growth"
The Spring Meeting of JSAP, Paper No. 31p-K-10, Aoyama Gakuin Univ., March 29 - April 1, 1985.

41. T. Fujino, H. Inokawa, T. Kobayashi, I. Yamada and T. Takagi,
"Crystallization of Al2O3 Films Deposited by Reactive Ionized Cluster Beam Deposition"
The Spring Meeting of JSAP, Paper No. 31p-K-12, Aoyama Gakuin Univ., March 29 - April 1, 1985.

42. H. Inokawa, M. Shibutani, T. Fujino, I. Yamada and T. Takagi,
"Buried Insulating Layer Formation by $O^+$ Implantation to Polycrystalline and ICB Epitaxial Al Films"
The Spring Meeting of JSAP, Paper No. 31p-H-16, Aoyama Gakuin Univ., March 29 - April 1, 1985.

List of Papers (Concluded)

* IEEJ(The Institute of Electrical Engineers of Japan)
* JSAP(The Japan Society of Applied Physics)
* IECEJ(The Institute of Electronics and Communication Engineering of Japan)